The Stability of the Bottom Boundary Layer

Under a Model Mode-1 Internal Tide

John Manuel Segreto

August 2018

ABSTRACT

The instability properties of the bottom boundary layer (BBL) under a model mode-1 internal tide in linearly stratified finite-depth water are studied, using 2-D fully nonlinear and non-hydrostatic direct numerical simulations (DNS) based on a spectral multidomain penalty method model. Low-mode internal tides are known to transport large amounts of energy throughout the oceans. One possible mechanism, among others, through which the energy of the particular tidal waves can be directly dissipated, without transfer to higher modes, is through wave-BBL interactions, where strong near-bottom shear layers develop, leading to localized instabilities and ultimately mixing. In the model problem, the stability response of the time-dependent wave-induced BBL is examined by introducing low-amplitude perturbations near the bed. For the linear stage of instability evolution, the time-dependent perturbation energy growth rates are computed by tracking the largest perturbation energy density in the domain through the wave-modulated shear and stratification, ultimately the formation of distinct localized near-bed Kelvin Helmholtz billows are observed. The average growth rate, σ, is then compared to the time, T_w, that a parcel of fluid is subject to a local Richardson number less than 1/4, resulting in a nondimensional criterion for instability, σT_w. A stability boundary is then constructed as a function of the three non-dimensional parameters that characterize the flow, the wave steepness, aspect ratio and Reynolds number. It is shown that the nondimensional growth rate can be written as a function of these parameter, $\sigma T_w = F(Re, st, AR)$. Additionally the minimum initial perturbation amplitude that is shown to cause over-

turning of isodensity surfaces for each parameter set is also shown to be a function of the wave parameters, $A_c = F(Re, st, AR)$.

BIOGRAPHICAL SKETCH

The author was born on April 2, 1992 in Red Bank, New Jersey. He did his undergraduate studies at Coastal Carolina University in South Carolina in the Department of Physics and Chemistry. In 2015 he came to Cornell University and started the Master of Science program in Environmental Fluid Mechanics & Hydrology and conducted research under the supervision of Professor Peter Diamessis on the bottom boundary layer stability under mode-1 internal waves, which is the subject of this thesis.

This thesis is dedicated to my parents for supporting and believing in me.

ACKNOWLEDGMENTS

I would like to thank Professor Peter Diamessis for all of the help and support that he has given me throughout the process of completing this work. He has given me a wonderful opportunity to study at an amazing institution. In addition, he has motivated me to become a better researcher and academic. Moreover, he has been a role model. I would like to thank Professor Roi Gurka (CCU) for introducing me to the world of fluid dynamics, being my mentor, and putting me on this path. I would also like to thank Dr. Kris Rowe for helping with any technical questions and for giving his time freely. I would like to thank Professor Edwin Cowen and Professor Gregory Bewley for their insightful remarks which served to improve this work. Lastly, I would like to thank the Alfred P. Sloan Foundation for the funding that allowed me to complete this work.

Contents

Chapter 1

Introduction

1.1 Internal Gravity Waves

Gravity waves are waves that are generated when a fluid, displaced from equilibrium, is acted on by restoring forces (i.e. buoyancy and/or gravity). Most commonly gravity waves are thought of as a surface phenomena. Surface gravity waves occur at the interface of two media, the ocean and atmosphere. However gravity waves can also occur within a single stratified media and are known as internal gravity waves[37]. Within a stratified fluid medium in nature, density differences are relatively small. As a result internal gravity waves are capable of having much larger amplitudes than surface waves, often reaching several tens to hundreds of meters. The displaced fluid, in both surface and internal gravity waves, generates currents as it oscillates about its equilibrium position. The associated currents can have shear that is strong enough to lead to instability and turbulence[32]. The frequency of the oscillation is determined by the local density stratification and is known

as the buoyancy frequency (Brünt-Vaisala frequency), denoted as N.

$$N^2 = \frac{-g}{\rho_o} \frac{\partial \rho}{\partial z} \qquad (1.1)$$

Where g represents the force of gravity, ρ and ρ_0 are the local density and reference density respectively and z is the vertical coordinate. A full discussion on the derivation of the buoyancy frequency is given in Sutherland's *Internal Gravity Waves* [94]. The primary focus of this work is on internal gravity waves, hereafter refereed to simply as internal waves.

Internal waves (IWs) can be further classified into two categories, waves that propagate in a continuously stratified fluid or those that are confined to density interfaces. In a continuously stratified fluid IWs have the interesting property, that the wave phase, c, and group, c_g, velocities are perpendicular to one another. This is due to the fact that the vertical phase and group velocities are always opposite, the effect being that IWs propagating their phase upward will be propagating their energy downward. The dispersion relation for IWs can be used to relate the frequency of the wave, ω, to the direction of the wave propagation. The dispersion relation is given by

$$\omega^2 = \frac{N^2 \times (k^2 + l^2)}{k^2 + l^2 + m^2}, \qquad (1.2)$$

where $\mathbf{K} = (k, l, m)$ is the wave number vector. Further discussion on the dispersion relation can be found in chapter 8 of *Fluid Mechanics* by Kundu et. al. [50]. A schematic of internal wave propagation is shown in figure 1.1. Note that the wave vector $\mathbf{K}$ is in the same direction as the phase velocity,
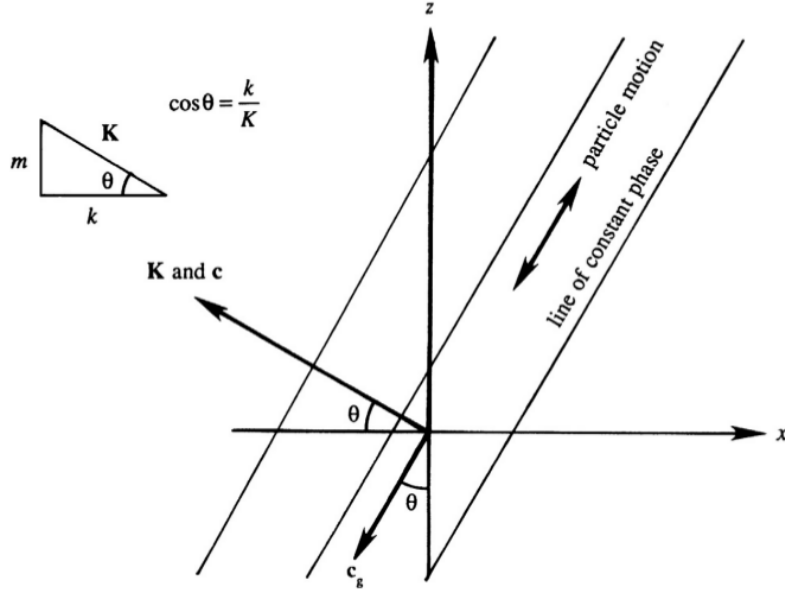
Figure 1.1: Schematic of internal wave propagation from Kundu et. al. *Fluid Mechanics.*

while particle motions are aligned with the group velocity (perpendicular to the phase velocity). Waves that are confined to density interfaces are known as interfacial waves and have group and phase velocities that are in the same direction. Density interfaces that can support interfacial waves are ubiquitous in nature. In oceans[33] and lakes[43] there is typically a thermocline where there are two different temperature fluids with a steep temperature gradient between them. Within the lowest layer of the atmosphere (troposphere) there is an interface between the convective boundary layer and the free atmosphere known as the entertainment zone which can support interfacial waves[25]. Above the entrainment zone there are interfaces between the various layers of the atmosphere that can support interfacial waves such as the tropopause, which is the interface between the troposphere and the stratosphere. Interfacial waves can be further classified as either periodic or

solitary, further discussion can be found in Sutherland's textbook *Internal Gravity Waves*[94].

This study is focused on a particular class of internal gravity waves known as internal tides which are classified as periodic progressive waves that propagate in a continuously stratified environment. Internal tides are generated by the interaction of the barotropic tidal currents with topography. Therefore these waves propagate with a tidal frequency and have amplitudes on the order of the scale of the topography that generated them [103] [32] [31]. Unlike other internal waves, the tides are dominated by the lowest vertical modes. As a result the internal tides propagate primarily horizontally [103].

1.2   Motivation

The forcing mechanism that generates the internal tidal field is the interaction of the barotropic tidal motions, that are generated by the gravitational forces on the earth caused by moon and sun, with topography. The tidal constituents, or tidal frequencies, that make up the barotropic tidal currents can be seen in the spectrum of sea level variation estimated from bottom pressure in figure 1.2, which shows a variety of frequency peaks corresponding to both diurnal ($\approx 1/24 hr^{-1}$) and semi-diurnal ($\approx 1/12 hr^{-1}$) frequencies. The largest of these frequencies is the principal lunar tide, M_2.

The total global rate of barotropic tidal energy dissipationin the Earth-Moon-Sun system has been well determined [24]. The principal semidiurnal lunar tide dissipates 2.5 TW (figure 1.3), while all lunar tides dissipate 3.2 TW, in total 3.7 TW of energy are dissipated when including the solar

tides. Of the tidal energy dissipated it is estimated that up to 1 TW is lost from barotropic tides in the deep ocean and that nearly all of this energy is converted to internal tides[24][23]. Of the estimated 2 TW of mixing energy required to maintain the abyssal global stratification of the ocean[63], one-half could therefore be provided by the internal tides[23]. To gain an understanding of how this energy is distributed throughout the ocean, we will now look at some of the fundamental characteristics of the internal tidal field.
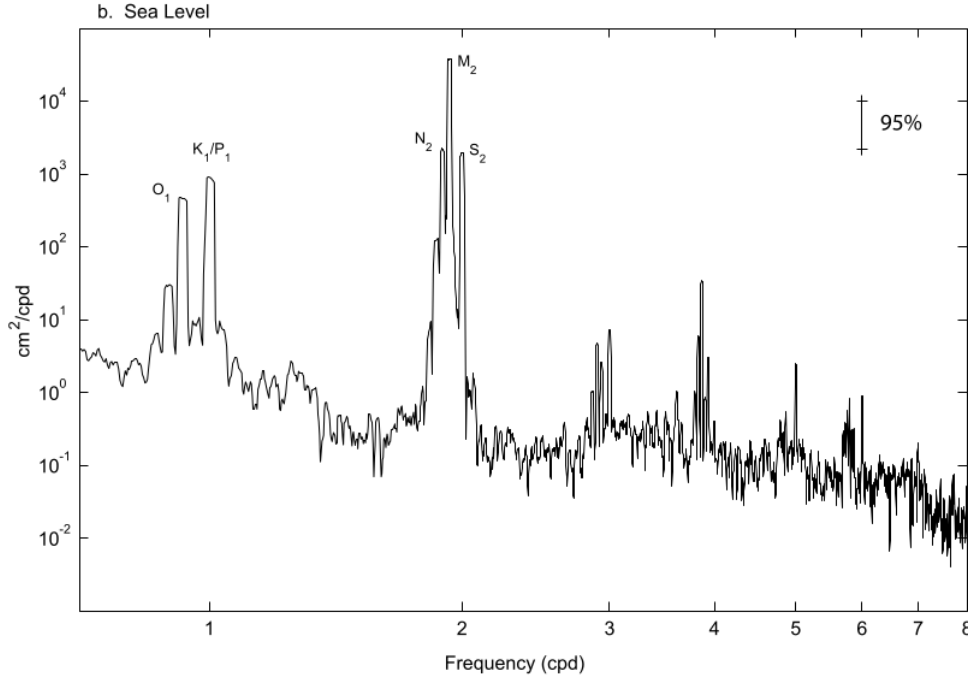

Figure 1.2: Spectrum of sea level variations estimated from bottom pressure on the New England Shelf by Shearman and Lentz [83]. Individual peaks at diurnal (K_1, O_1, P_1) and semi-diurnal (M_2, N_2, S_2) frequencies are labeled.

1.2.1   Internal Tide Fundamentals

In order to understand the distribution of the energy in the internal tidal field, we can examine where and how the energy is transferred to the internal tides and how the tides then transport that energy. Egbert & Ray, show that the barotropic tidal energy is generally transferred to the internal tides in regions associated with three types of topography; oceanic islands, oceanic trenches, and midocean ridges [24] [90] (refer to figure 1.3). These baroclinic, or internal, tides that are generated tend to have a rich vertical structure causing dramatic vertical displacements of density surfaces and induce horizontal currents that are typically comparable in strength to the barotropic tidal currents that generated them. Due to their strong horizontal currents and rich vertical structure, internal tides can have vertical shear that is strong enough to lead to instability and turbulence [32]. When these wave break, or go unstable, energy is dissipated locally at the breaking site. However, low mode components are typically more stable and tend to propagate away from the generation site without much dissipation.

At large-scale bathymetry most of the outward radiated energy flux is associated with low mode components, characterized by long horizontal wavelengths which propagate nearly horizontally [32]. Only a small fraction is generated at smaller spatial scales, which dissipate locally due to higher shear and faster wave-wave interactions[52]. This is evident at the Hawaiian Ridge where Carter et. al.[12] shows in a model that 1.7 GW of the baroclinic tidal energy is radiated away, while 0.45 GW is dissipated close to the generation region. The large-scale motions associated with the radiated
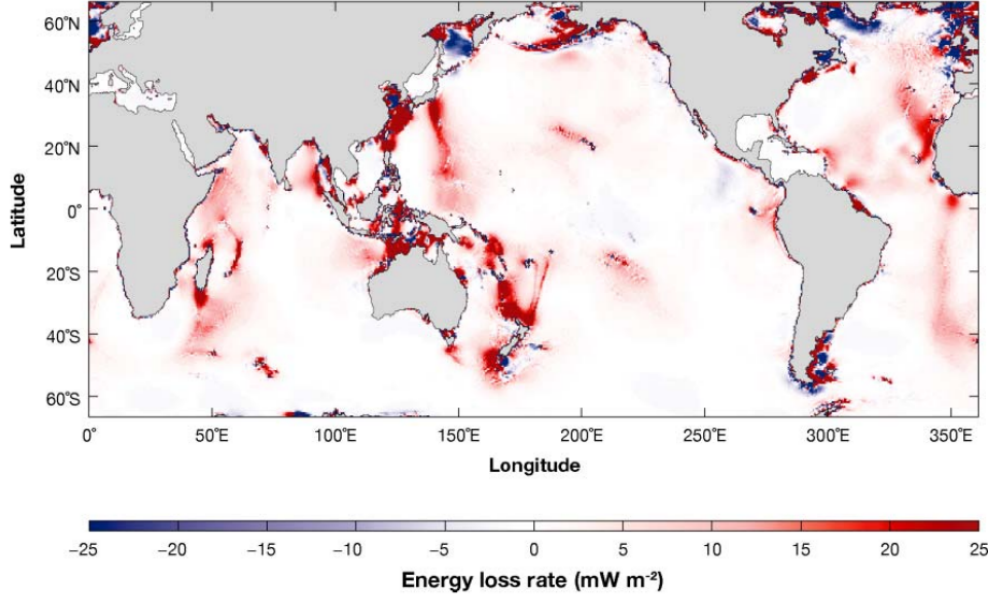
Figure 1.3: Estimated rate of the loss of energy from the barotropic M_2 tide. It has been shown by Egbert and Ray (2001) that most of the dissipation is occurring near oceanic islands, trenches, and midocean ridges, where this energy is converted to the internal tidal field [24] [32]

internal tide typically have Richardson numbers (refer to section 2.0.2) exceeding unity, meaning that a direct shear instability mechanism is not the dominant mechanism for energy transfer to smaller scales [90]. Additionally, the low modes are not significantly influenced by nonlinear processes, such as harmonic generation [22], and can therefore transport energy over very large distances before they are dissipated. Internal tides generated at the Hawaiian Ridge [71] and Aleutian Ridge [16] have been observed to propagate over 1000 km, indicating that low-mode internal tides contribute to mixing at locations far away from their generation sites (remotely).

The mechanisms by which the energy in the low mode internal tidal field is transferred to smaller scales and ultimately dissipated is poorly understood

and thus must be studied in greater detail[51]. It is important to understand
how this energy is dissipated so that it can be accurately parameterized in
general circulation models (GCM). Additionally, knowledge of the mechanism
by which the energy is ultimately dissipated can improve the understanding
of how ecological systems may be affected through redistribution of sediment
and nutrients caused by near bottom turbulence linked to internal tide dissi-
pation. To guide us in understanding the possible mechanisms through which
the radiated energy in low mode internal tides is dissipated we turn to some
previous work.

1.2.2   Dissipation Mechanisms

As it is not clearly understood where and how internal tide energy is ulti-
mately transferred to smaller-scales or dissipated at the smallest scales by
turbulence. It is important to know the spatial structure and temporal evo-
lution of the internal wave field that is generated through the internal tide
generation process [51] in order to understand which dissipation mechanisms
are dominant. The structure of the internal wave field coupled with back-
ground flow characteristics and the geometry of the boundaries will primary
determine the dissipation mechanism and spatial distribution of that dissipa-
tion. The possible candidates for the dissipation of internal waves in general
are

- local mixing near generation sites
- wave–wave interactions in the deep ocean
- scattering by sea-floor topography [68][47] [2][53]
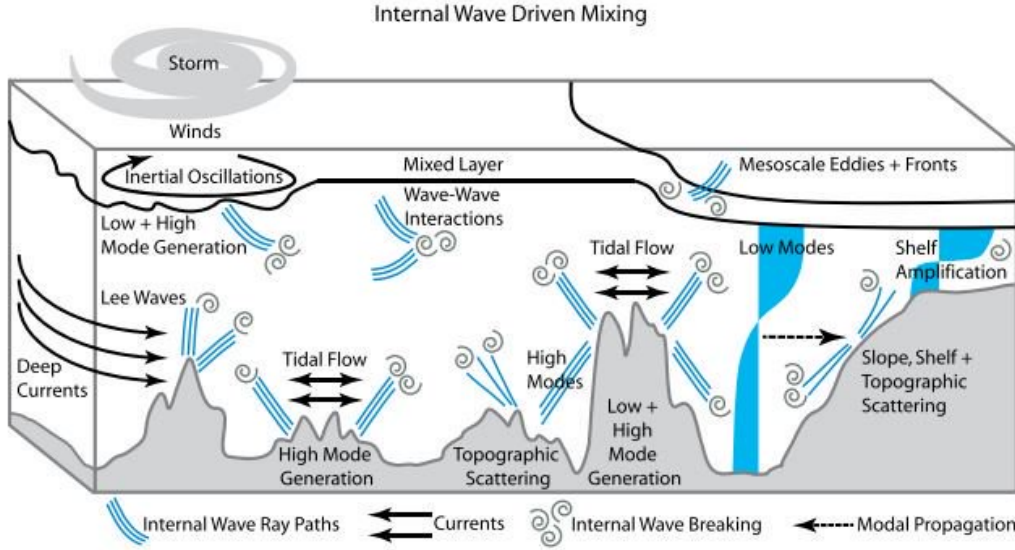
Figure 1.4: Internal wave driven mixing cartoon from MacKinnon et. al. (2017).

- scattering by mesoscale features[70]

- reflection at continental shelves [14]

- shoaling on sloping continental shelves [51]

- intensified boundary flows at near-critical slopes [35]

- parametric subharmonic instability (PSI)[55] [106] although recent observations suggest that PSI is not relevant for mode-1 diurnal tides[108]

Determining the role of each of these candidates requires that the structure of the radiated internal tides is well known. In addition to knowing the exact structure of the radiated internal tides, we must also know the conditions for a specific dissipation mechanism to be active. Finally, for each dissipation mechanism we must also know the amount of energy that will be dissipated for a given set of the flow characteristics, such as the velocity and density fields. It is plausible that no single dissipation mechanism is globally

dominant, but instead that the relative importance of different mechanisms varies geographically and seasonally[105].

The primary candidates for the dissipation of the radiated energy in low mode internal tides as stated by Echeverri et. al. [22] are transfer to smaller-scale internal waves in the ocean interior [55] [90], scattering by sea-floor topography or mesoscale features in the ocean and reflection at continental shelves. However, long internal solitary waves which are used to help guide our understanding of internal wave dissipation are shown to have different dissipation mechanisms. Internal solitary waves tend to have smaller wavelengths, shorter time scales and are typically more prone to nonlinear effects then internal tides which is why there are differences in the dissipation mechanisms. Helfrich & Melville [39] noted that the most significant types of internal wave dissipation are radiation damping, boundary shear, wave breaking/shoaling and shear instability. Additionally, internal solitary waves have been shown by Diamessis & Redekopp to generate bottom boundary layer vortex shedding causes intensified shear stress and drag on the wave [19]. Since the structure of the boundary layer under a solitary wave has some similar characteristics to the boundary layer under a low mode internal tide, it is proposed that the BBL under a low mode internal tide can also create intensified shear stress that may lead to instability and ultimately dissipation.

The dissipation mechanism of interest in this study is that driven by bottom shear caused by the interaction of low mode internal tides with a horizontal boundary. It is shown by Ansong et. al.[1] that open ocean wave drag of the low mode internal tides is required to achieve agreement between

modeled and observed baroclinic tides[84][9]. It is proposed that if low mode waves can form bottom boundary layer structures that are unstable and can lead to dissipation, over very large distances the cumulative amount of energy dissipated may be significant. Since these low mode waves are known to propagate over very large distances this mechanism may even be dominant, atleast in regions where other mechanisms are less favorable.

1.2.3 Parameterization in GCMs

An accurate description of the dissipation of energy in the radiated low mode internal tides is a prerequisite for the correct parameterization in general circulation models[13]. General circulation models are a class of computer-driven models used for forecasting weather and climate as well as for studying how various processes may affect climate, where they are commonly called global climate models. A global climate model (GCM) aims to describe climate behavior by integrating a variety of fluid-dynamical, chemical, and biological equations that are either derived directly from physical laws or constructed using empirical observations. Simulations must be designed so they can be completed and analyzed in a timely manner, however even the worlds most powerful computers have computational limitations. Due to the computational limitations approximations and parameterizations must be employed.

Climate processes operate on time scales ranging from several hours to millennia and on spatial scales ranging from a few centimeters to thousands of kilometers, due to the vast range of scales that affect climate parameter-

izations of sub-grid scale phenomena are required. Current GCMs operate
with horizontal resolution O(50 - 100 km), vertical resolution O(200 m), and
temporal resolution O(30 mins) [80], much too coarse to resolve internal tides
and the mechanisms by which they dissipate their energy.

Since internal tides contain large amounts of energy and are capable of
transporting this energy over large distances it is important to have accurate
parameterization of these processes. Understanding how and where waves are
generated, as well as dissipated, is the first step in adequately parameterizing
the energy transport and dissipation.

It has been observed through numerical modeling studies that the ocean
state is particularly sensitive to the spatial distribution of mixing. The verti-
cal distribution of mixing[77] and specifically vertical mixing associated with
gravity waves [61] seems to have a greater impact on the global state than
the corresponding horizontal distribution. However, the horizontal distri-
bution of mixing still plays a significant role, [87] suggesting that spatially
varying bottom intensified mixing is an essential component of the balances
required for the maintenance of the ocean's abyssal stratification. Thus the
global mixing patterns and amplitudes caused by internal wave generation,
propagation and breaking [61] must be understood in order to adequately
account for the IW field dissipation in GCMs. Understanding the physical
mechanisms responsible for this mixing will allow for more accurate param-
eterizations in numerical ocean modeling and will further our understanding
of how the abyssal stratification is maintained [63] and in general how the
ocean works[23].

In order to demonstrate that the choice in parameterization scheme can

affect the result of a GCM, Melet et. al. [61] performed a series of climate simulations using the GFDL-ESM2G, a global coupled carbon–climate Earth system model (coupled ocean–ice–atmosphere– land–biogeochemistry coupled model). The ocean model used was the Generalized Ocean Layer Dynamics (GOLD) isopycnal model. The impact of remote and local internal-tide dissipation on the ocean state was determined by meridional overturning and the oceanic heat budget. In the numerical study three different vertical profiles of mechanical energy dissipation were used to compare how the choice of parameterization can affect the global state of the ocean. The first parameterization chosen was that of St. Laurent et. al.[90] in which the internal tidal dissipation scales as an exponential decrease above the seafloor. This profile is motivated by the bottom-intensified dissipation simulated at critical slopes [53]. Two additional parameterizations used were chosen such that the internal tidal dissipation scales with N and N^2 respectively. Scaling with N is suggested by Gargett et.al.[29], with physical justification from catastrophic breaking of low-mode waves. The scaling with N^2 is supported by wave–wave interaction theory [102]. The stratification dependence of the dissipation means that the remote energy dissipation of internal tides will be stronger in the thermocline when scaling with N and even more so with N^2, where as the first scaling has stronger dissipation at the sea floor. Additionally, the remote dissipation of the internal-tide energy was also paramaterized to occur with some horizontal distribution such that it would be focused on continental slopes (S) , continental shelves (C), or in the ocean basins (B).

In figure 1.5, it can be seen that te parameterizations of the internal tide energy dissipation can have a drastic effect on the global state of the

ocean. The globally averaged ocean temperature is plotted as a function of time for various internal tide parameterizations. These internal tide parameterizations are a combination of the different horizontal distributions, combined with the three different scalings for the vertical distribution of the dissipation.From these GCM simulations it can be seen that thechoice in parameterization drastically effects the globally averaged ocean temperature, more precisely how the spatial distribution of the parameterization effects the results.
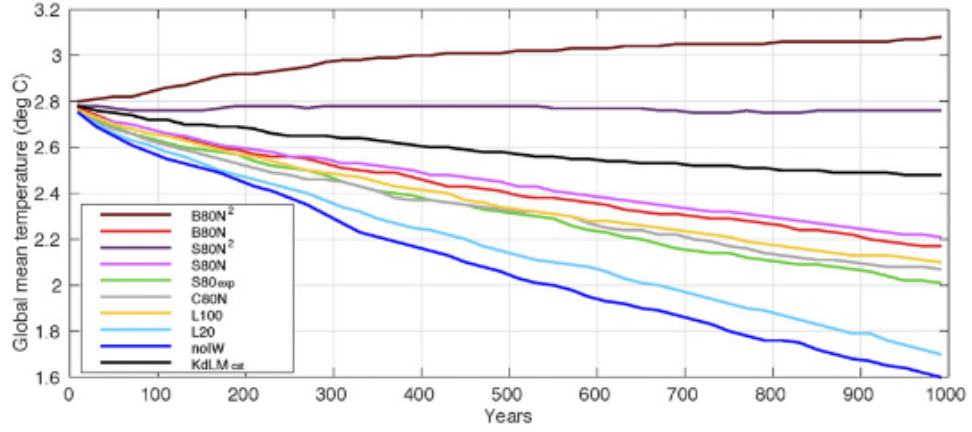
Figure 1.5: The globally averaged ocean temperature (C) for all GCM results as a function of simulation time. Increasing the mixing generally warms the ocean, as does shifting the mixing energy into more stratified waters (Melet et al. (2016)). The horizontal distribution on the dissipation is denoted by S , C, and B, representing dissipation on continental slopes, continental shelves and ocean basins respectively. The vertical distribution of the dissipation is represented by exp, N, and N^2.n.

Internal waves dissipation is known to be the main source of diapycnal mixing in the ocean [90]. Given that each dissipation mechanism has its own spatial distribution, understanding the relative importance of each dissipation mechanism will allow for more accurate parameterizations. Since the

parameterized energy loss due to wave drag in current GCM formulations is based soly on topographic scattering [90], additional mechanisms for wave drag dissipation in the open ocean must be studied in order to understand the damping of radiated internal tides.

The main focus of this work is on understanding the interaction of internal tides with a horizontal sea floor. The wave induced bottom boundary layer structure induced by this interaction may be prone to instabilities. The instabilities may lead to turbulence and dissipation that has a spatial distribution that may be important to understand. The correct spatial distribution of the dissipation may lead to more accurate parameterization for internal tide wave drag in the ocean.

1.2.4 Drivers of Benthic Mixing and Particulate Transport

Internal tide interaction with the sea floor is not only important in regard to ocean structure and circulation but also to ecological systems, sediment resuspension and transport. The interaction of a wave with solid surfaces are known to induce boundary layer profiles with strong shear. It is generally assumed that high bottom shear stresses associated with breaking waves dislodge particulate matter, such as sediment or nutrients from the seafloor, injecting it into suspension in the water column [58]. The resuspension of particulate and further transport by the wave-induced currents can have important ecological effects and may impact the transport of sediment[15].

The turbulence and mixing created by the internal tides interaction with

the bed is known to drive vertical fluxes. The vertical fluxes through the benthic zone are capable of transporting nutrients that are necessary for maintaining ecological systems [78][31]. In the coastal oceans ecological systems rely on nutrients supplied from the deep ocean [85]. On the southern continental shelf of Monterrey Bay, California bottom material was mobilized into the bottom boundary layer (BBL) by intense near-bed vertical velocities associated with the internal tidal currents. The suspended particulate matter was then advected by the onshore phase[15][81]. Vertical mixing is also required in the open ocean to replenish nutrients in the euphotic zone[78]. From measurements taken on the Scotian Shelf off Nova Scotia it was concluded that mixing by large amplitude internal tides were sufficient to supply the required nutrients to the euphotic zone[78]. Mixing due to the breaking of internal tides is thus crucial to the maintenance of ecological system [78] as well as having the capability to detach, resuspend and disperse sediment[58].

1.3   Literature Review

In the following sections we will review some of the literature focused on a variety of unsteady shear flows which exhibited instability. In section 2, the fundamentals of shear flow instabilities is presented for the purpose of reviewing work on instabilities in steady shear flows needed to study the unsteady problem presented here. The specific base flows include both periodic and solitary interfacial wave instabilities, in addition to solitary wave boundary layers and oscillatory boundary layers. Both the periodic and solitary interfacial wave instability problem gives insight into how our problem should be

investigated. For example, developing an instability criterion that is based on the average growth rate over a given window in time and that whether that instability criterion is met is a function of the Richardson number. Then we will bring our focus to boundary layer instabilities, although all of the boundary layer problems omit stratification at the bed, which reveal some boundary layer characteristics that are crucial in understanding where the preferential locations for instability may exist. The primary purpose of this review is to expose the reader to unsteady shear flow instabilities observed in the literature. These will then guide us in understanding how the instabilities may develop in the BBL under a mode-1 internal wave, a model for the mode-1 internal tide.

1.3.1 Progressive Interfacial Waves

Periodic Interfacial Waves

Breaking of progressive, periodic, internal interfacial waves have been studied in laboratory experiments by Troy & Koseff [98] and in numerical simulations by Fringer & Street [26]. The waves under consideration by Troy & Koseff were long relative to the thickness of the density interface ($k\delta > 0.56$) and Fringer & Street studied moderate length waves ($0.31 < k\delta < 0.56$) where k is the horizontal wavelength and δ is the interface thickness. It is stated by Fringer & Street [26] that this class of waves can be fully characterized by the set of parameters (a, k, δ , ν , κ , g), where the dispersion relation sets the wave frequency ω, and the wave induced velocities are determined by the entire parameter set, a is the wave amplitude, ν is the fluid kinematic

viscosity and κ is the diffusivity of the stratifying scalar.
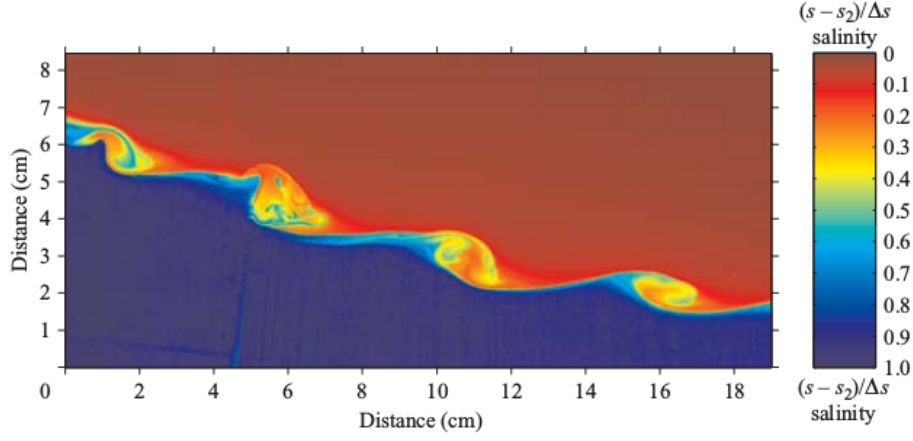
Figure 1.6: Row of Kelvin–Helmholtz billows observed by Troy & Koseff [98] in a progressive periodic wave trough for $k\delta = 0.048$ at time $t/T = 0.625$. The direction of wave propagation is left to right.

Troy and Koseff [98] state that regardless of the instability mechanism, the critical wave steepness ka_c at which progressive interfacial waves break can be identified as having the functional dependence,

$$ka_c = F(k\delta, Re, Sc). \tag{1.3}$$

Equivalently the same criterion can be written in terms of a critical wave induced Richardson number,

$$Ri_c = F(k\delta, Re, Sc), \tag{1.4}$$

since the parameters ka and $k\delta$ fully determine Ri, where

$$Ri \approx \frac{k\delta}{5.3(ka)^2}. \tag{1.5}$$

This approximation is made for periodic lowest-mode internal waves in a hyperbolic-tangent (two-layer) density profile and is shown to hold well for low values of $k\delta$ and $kak\delta$ [26].

The initial two dimensional instability that affects finite amplitude periodic interfacial waves consists of three different regimes. For waves with $k\delta < 0.56$, it was observed that the wave breaking most closely resembled a Kelvin-Helmholtz shear instability that originated in the wave crest and trough regions where there is high shear, an example of this can be seen in figure 1.6 where a row of billow have rolled up and began to break down. The critical wave steepness at which the wave breaking occurred was wave number dependent for all waves [98]. In the second regime, further increasing the interface thickness produces waves with energetic Kelvin–Helmholtz billows that induce a convective instability. In the last regime, waves having a non-dimensional interface thickness that is greater than $k\delta = 2.33$ are limited in amplitude by a weak two-dimensional convective instability that results when the maximum Froude number is greater than one, $Fr_{max} > 1$ [26], where the maximum Froude number is given in equation (1.7).

A stable interfacial wave was then defined in terms of the minimum Richardson number within the wave and the maximum Froude number. It was shown that these two values could be defined in terms of the wave steepness, ka, and the interface thickness, $k\delta$. The minimum Richardson number is given by

$$Ri_{min} = \frac{N^2}{(\partial u/\partial z)^2} \approx \frac{1}{8}\frac{k\delta}{(ka)^2}, \qquad (1.6)$$

and the maximum Froude number is

$$Fr_{max} = \frac{u_{max}}{c} \approx ka, \tag{1.7}$$

where u_{max} is the maximum velocity induced by the wave and c is the phase speed. The minimum Richardson number is then considered the bulk wave Richardson number (i.e. $Ri_w = Ri_{min}$).

For all ranges of $k\delta$ tested, it was observed that the critical wave Richardson number, Ri_w, that resulted in overturning was well below the canonical value of $Ri = 0.25$. In addition it was shown that the critical Ri_w decreased with decreasing nondimensional wavelength. This relationship is due to the fact that the growth rate increases with decreasing Ri_w and that the amount of time that a perturbation is in a region of appreciable shear decreases with decreasing $k\delta$. Shorter wavelengths the require higher growth rates for there to be overturning. To state this requirement more precisely, oscillatory motions that generate shear must have growth rates that are large enough so that the perturbation can grow to a significant amplitude within the time scale of the wave[98].

For the case of the periodic progressive interfacial wave, where the interface is described by a hyperbolic tangent density profile, it is stated by Troy & Koseff [98] that the time that the Richardson number will locally fall below 1/4 is given by

$$T_w = \frac{2}{\omega} \arccos\left(2Ri_w^{1/2}\right), \tag{1.8}$$

which is found from theory. The time varying amplitude of the growing

perturbation is then assumed to behave as

$$\frac{da_i}{dt} = a_i \sigma_i, \tag{1.9}$$

over a time T_w, the perturbation will then grow to amplitude

$$a_{i_w} = a_{i_0} \exp\left(\overline{\sigma}_i T_w\right). \tag{1.10}$$

Where $\overline{\sigma}_i$ is the average growth rate over time T_w and a_{i_0} is the initial perturbation amplitude. Instability will then occur only if $a_{i_w}/a_{i_0} \gg 1$, or

$$\overline{\sigma}_i T_w \gg 0. \tag{1.11}$$

In addition, it was found that the perturbation growth rate $\overline{\sigma}_i$ increased nearly linearly with decreasing Ri_w.

The instability criterion (1.11) can be rephrased in terms of a constant c as $\sigma_i T_w > c$ and solved numerically for different values of c, where c is the value for which the flow is unstable. In general, the value of c depends on the definition of instability since it is directly related to the maximum amplitude of the perturbations [98]. In both studies the value of the constant $c = 5$ was chosen to give good agreement with the data[98] [26].

The critical wave steepness is plotted as a function of the non-dimensional wavelength for both simulations and experiments in figures 1.7 and 1.8 respectively. In both figures it can be seen that the critical wave steepness and therefore the critical wave Richardson number increase with increasing non-dimensional wavelength. In figure 1.8, above $k\delta$ the critical wave steepness

becomes about constant. The constant critical wave steepness is just above 1. In this regime it is now the Fr condition that is causing the wave to break and the instability mechanism is purely convective.
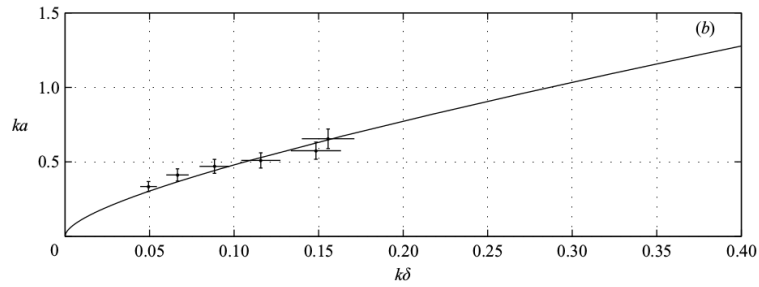

Figure 1.7: The critical wave steepness is plotted against the nondimensional wave length for the simulations of progressive interfacial waves conducted by Troy & Koseff over the range of $k\delta > 0.56$ [98].
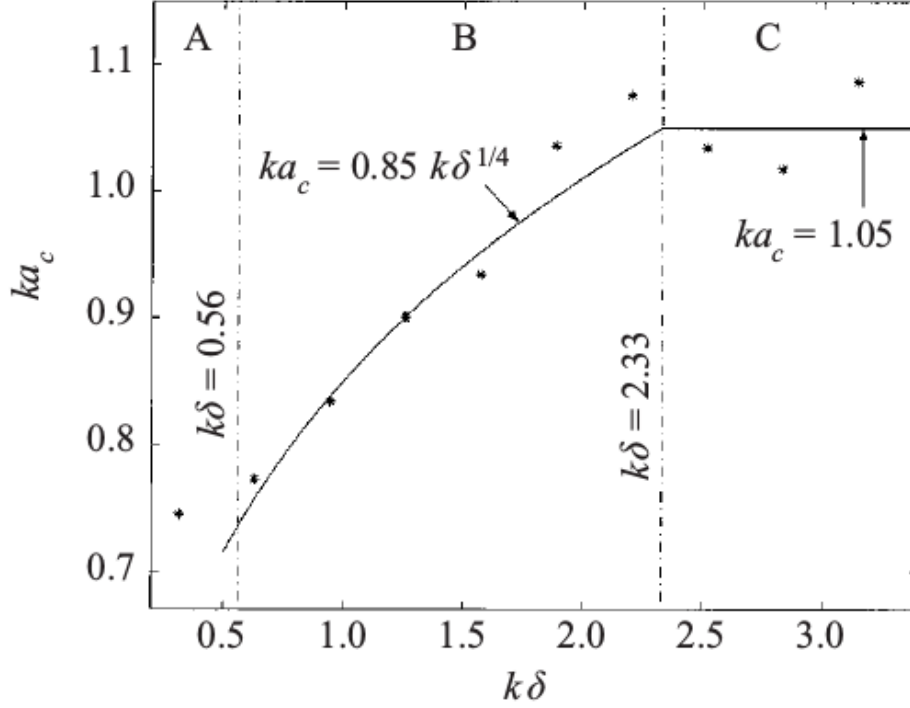
Figure 1.8: The critical wave steepness is plotted against the nondimensional wave length for the experiments of progressive interfacial waves conducted by Fringer & Street who studied moderate length waves, $0.31 < k\delta < 0.56$ [26].

Internal Solitary Waves

The stability properties of interfacial internal solitary waves were studied in numerical simulations conducted by Barad & Fringer [3]. In the simulations, a block structured adaptive mesh refinement (AMR) method was used. This method was chosen to overcome computational limitations that are inherent in wave instability problems that involve a broad range of scales [3]. AMR methods are useful in this regard because resolution can be focused in active regions of the flow field.

To determine the stability of the flow Barad & Fringer focus again on a Richardson number of the flow. Barad & Fringer state that the Richardson number can be written as a function of the three nondimensional wave parameters the characterize the flow. These parameters are the ratio of the upper layer depth to the lower layer H_1/H_2, the interface thickness nondimensionalized by the upper layer depth δ_0/H_1, and the nondimensional wave amplitude α/H_1.

$$Ri = Ri(\frac{H_1}{H_2}, \frac{\delta_0}{H_1}, \frac{\alpha}{H_1}) \tag{1.12}$$

A critical Richardson number can then be found for a given set of background conditions based on the critical amplitude of the wave.

$$Ri_c = Ri(\frac{H_1}{H_2}, \frac{\delta_0}{H_1}, \frac{\alpha_c}{H_1}) \tag{1.13}$$

In the particular study, the ratio H_1/H_2 is held constant, while the effects of the non-dimensional interface thickness on the critical wave amplitude are assessed. It is seen that if there is a critical Richardson number then for a given set of H_1/H_2 and δ_0/H_1 then there is a critical wave amplitude that results in the critical Richardson number. An approximate value of the bulk Richardson number can be expressed in terms of the wave parameters as

$$Ri \approx \frac{g'\delta_0}{(\Delta U)^2}. \tag{1.14}$$

in which the velocity difference across the layers is approximated using as

$$\Delta U \approx \frac{\alpha(H_1 + H_2)c}{(H_1 - \alpha)(H_2 - \alpha)}, \tag{1.15}$$

where c is the solitary internal wave phase speed, $g' = g\Delta\rho/\rho_0$ is the reduced gravity, and $\Delta\rho$ is the density difference between the layers. For long, small-amplitude waves in a deep lower layer, $\alpha << H_1 << H_2$, Bogucki & Garrett [5] showed that the critical amplitude at which $Ri = 1/4$ is given by $\alpha_c = 2(\delta_0 H_1)^{1/2}$.

A key feature of internal solitary waves is that the vertical gradient in density changes because of vertical strain which acts to decrease the buoyancy frequency at the wave trough. The reduction of the buoyancy frequency coupled with the strong vertical shear within the wave leads to drastic decrease in Ri that was always a minimum at the wave troughs. In each of the simulations that were run, the minimum measured Richardson number was always below 0.25, however there were cases that did not lead to the formation of billows. It was shown that the computed growth rates along different locations upstream of the wave trough where $Ri < 1/4$ were always positive. However, unless the instabilities had sufficient time to grow into billows, then they were simply advected past the wave trough (in a frame moving with the waves) and appeared as small perturbations in the isopycnals. An example of a simulation where billow were able to form is shown in figure 1.9, in the first subplot the entire subdomain is shown and successive subplots show zoomed in versions of the domain focusing on the region directly behind the trough.

In the study conducted by Barad & Fringer, the growth rate was measured using the amplitude of the perturbations as

$$\frac{da_i}{dt} = \sigma_i a_i, \tag{1.16}$$

which can be converted to a spatially varying equation in a wave-following coordinate system with $x_L = (x - ct)/L$. Applying the coordinate transform and integrating yields

$$log(\frac{a_i}{a_{i_0}}) = \overline{\sigma_i}T_w, \tag{1.17}$$

where a_{i_0} is the initial amplitude of the perturbation and is assumed to be equal to $a_{i_0}/H_1 = 5 \times 10^{-8}$ due to numerical noise associated with the low order method where spatial and temporal discretization errors are $O(\Delta x^2)$. The instabilities are excited by the numerical errors and subsequently grow because of physical mechanisms. The average growth rate within the region where $Ri < 1/4$ is given by

$$\overline{\sigma_i} = \frac{L}{L_w} \int_0^{L_w/L} \overline{\sigma_i}(x_L)dx_L \tag{1.18}$$

where L_w is related to the width of the pocket of possible instability(i.e. where $Ri < 1/4$), the possible time for growth is then given by $T_w = L_w T/\lambda$. Where λ, the internal solitary wave wavelength, is defined as twice the distance from the trough of the wave to the point where the ρ_0 isopycnal is displaced by 5% relative to the maximum displacement in the trough. In all simulations $\lambda = 500m$.

Calculating an average growth rate of the instabilities within the pocket of instability showed that instability only occurred when $\sigma T_w > 5$. While the criteria for instability based on σT_w is sufficient, a more attractive criterion is based on the minimum Richardson number within the wave because instability can be assessed via a single pointwise value of Ri rather than via quantities that require information about the distribution of Ri within the

wave. There results indicate that the minimum Richardson number required for instabilities to arise was much lower than the canonical value for parallel shear flow. It was reported that shear instabilities developed only after the Richardson number feel below 0.1 . In addition to the two dimensional simulation a three dimensional simulation was run and indicates that the primary instability is indeed two-dimensional, which then lead to secondary three-dimensional instabilities.

Carr et. al [10] studied the interaction of internal solitary waves, of both depression and elevation, with a corrugated bed, using both numerical and experimental studies. In the study, the amplitude and the wavelength of the corrugated bed, together with the ISW amplitude and wave speed were varied. The internal solitary wave induced current, for both the elevation and depression waves, over the corrugated bed was observed to cause flow separation and vortices were formed. The vortices did not develop fully until after the wave passed. These vortices were capable of deforming the pycnocline and causing significant vertical mixing. It was found that the strength of the instability was dependent on both the amplitude and wavelength of the bottom topography. In the case of an ISW of depression, the generation of upward-propagating vortices is seen to result in entrainment of fluid from a bottom boundary.Large waves of elevation that were stable before the corrugations begin to exhibit evidence of a spatio-temporally developing shear instabilities as they interact with the bottom corrugation. The shear instability takes the form of billows that have a vertical extent that can reach 50% of the wave amplitude.
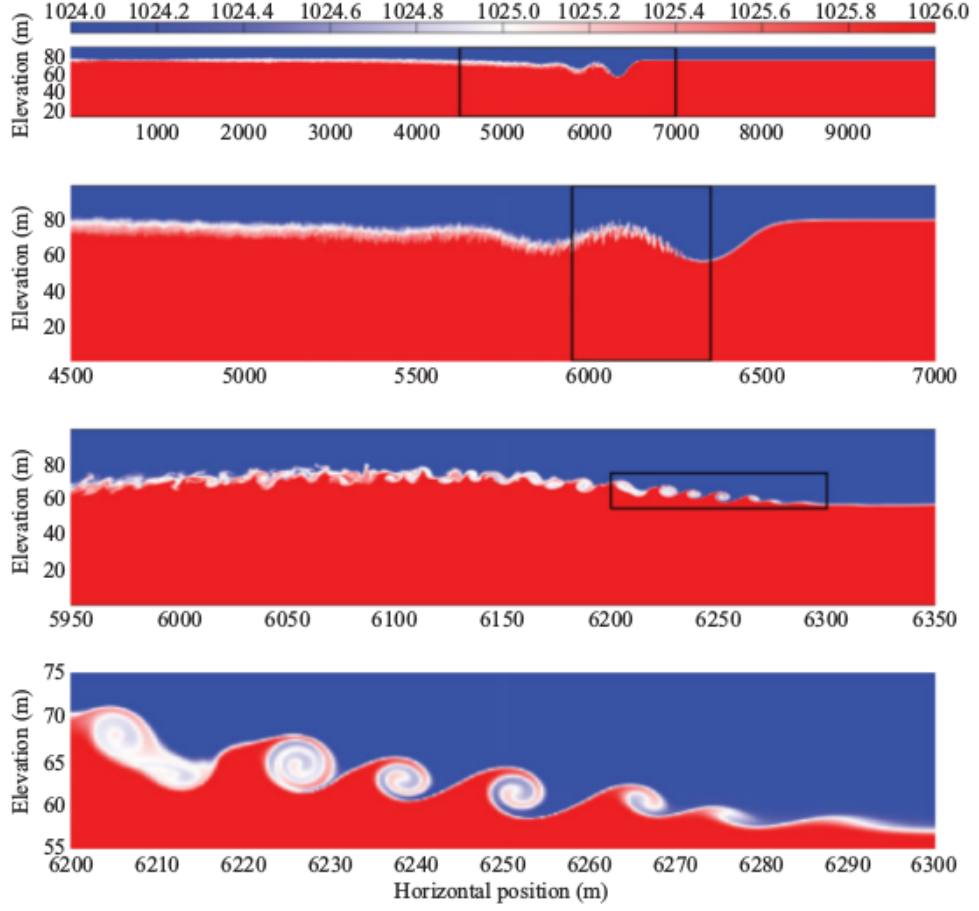
Figure 1.9: Detailed plot of the shear instability that has formed in simulation by Barad & Fringer at $t/T = 12$ in the leading wave for wave with $\delta_0/H_1 = 0.2$, $\alpha/H_1 = 1.18$, and $H_1/H_2 = 0.25$. Contours depict density in kgm^{-3}, and each plot is a zoomed-in view of the previous plot [3].

1.3.2 Boundary Layers

In the following section, two distinct boundary layer flows are examined, both of which consider homogeneous flows ($\rho = 0$). This simplification removes the stabilizing affects of the stratification as well as the discussion of the Ri criterion. However, the unsteady aspect of the boundary flow can give insight as to where and how the instabilities might develop in the case of a mode-1 internal tide.

The first scenario we will examine is the boundary layer induced by solitary waves. These flows are non periodic, however the unsteady nature of the boundary layer may still give some insight about the periodic case. The flow structure of a solitary wave can be compared at least in a rough qualitative sense to either the crest (solitary wave of elevation) or trough (solitary wave of depression) regions of a periodic wave. The solitary wave boundary layers may then be able to guide us in understanding the structure of the mode-1 internal tide boundary layer and in assessing which regions of the BL may most susceptible to instability. We then will turn our attention to oscillatory boundary flows in order to understand how the periodic nature of the BBL may affect the stability.

Solitary Wave Boundary Layers

A stability analysis was performed by Sadek et. al. [76] of the bottom boundary layer flow induced by a soliton-like wave using a fully nonlinear two dimensional simulation. The boundary layer was driven by a soliton-like wave induced pressure gradient using, an approximation to a BBL under

a surface solitary wave which mimics the U-tube experiments of Sumer et.
al [93]. Figure 1.10, shows an example of vortex tubes generated in the
BBL under a solitary wave in the U-tube experiments. The benefit to this
approximation is that the waves are assumed to be so long that there is no
horizontal dependence, which greatly simplifies the problem.

Figure 1.10: In experiment by Sumer et. al. vortex tubes generated in
the BBL under a solitary wave $\omega t = 105.7°$. With a maximum velocity of
$U_{0m} = 43.9 cms^{-1}$, and period of $T = 9.2s$, and $Re = 2.8 \times 10^5$ [93].

Sadek has shown that the BBL could become unstable depending on the
value of the BBL based Reynolds number and the amplitude and insertion
time of the perturbations. In the study it was found that the boundary layer
could be "stable", "conditionally unstable", or "unconditionally unstable"
depending on the time of the perturbation insertion as well as the amplitude
of the perturbation. Two distinct modes of instability were shown to exist.
Which one of these modes was dominate was dependent on the Reynolds
number of the flow. The instability mode are described as one that grows
pre-flow reversal and one that appears after the reversal. At a moderate value
of the Reynold number, both modes are observed during the deceleration
phase. For relatively low Re the post flow reversal mode was observed to
dominate. Finally, for Re above a threshold value of the base flow in the

unconditionally unstable regime, the pre-flow reversal mode, which is longer in wavelength than its post-reversal counterpart, is dominant. In figure 1.11, the left column shows the post-reversal mode dominates where $Re = 4000$ while in the right column the pre-reversal mode dominates at $Re = 8000$. The first row in the figure is the result of a linear stability analysis while the second and third rows are results of a DNS at two different phases of the wave.
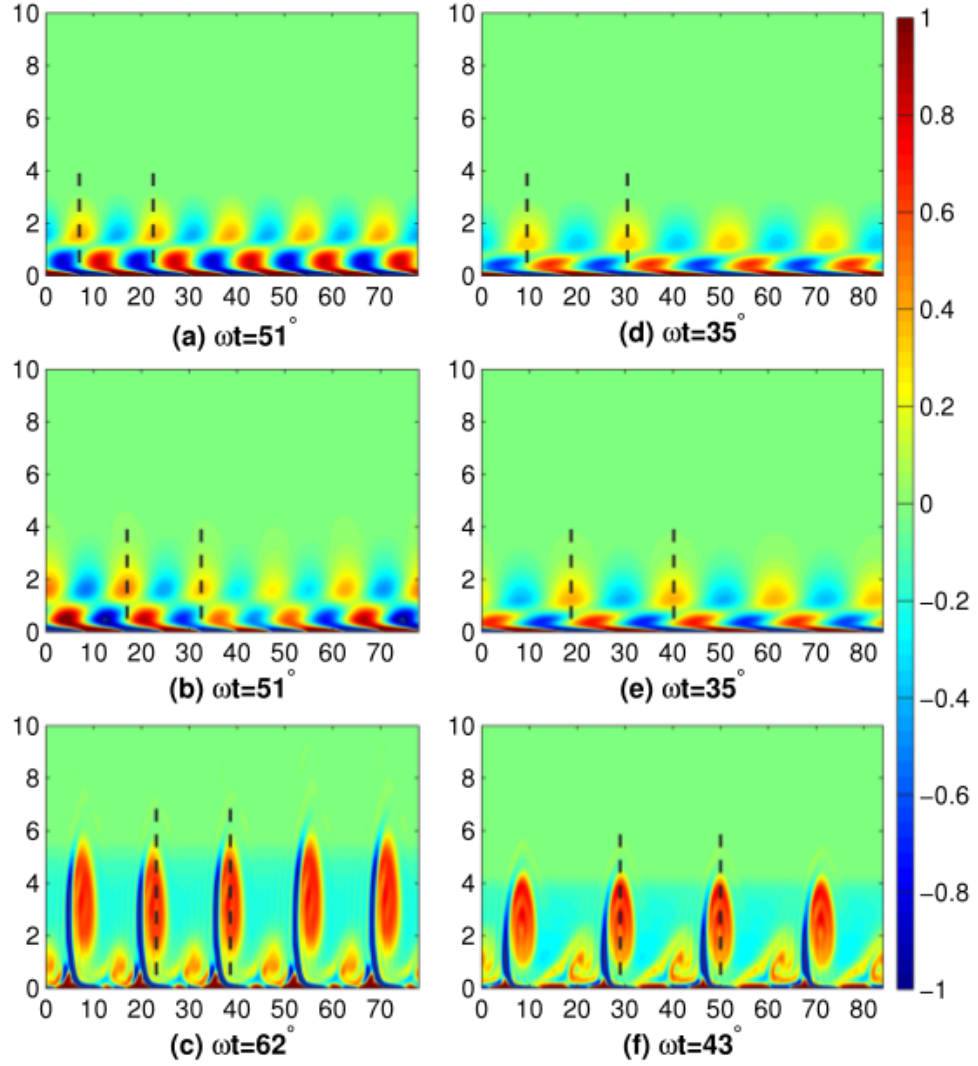
Figure 1.11: Sadek et. al., visualization of the perturbation vorticity field (normalized by the corresponding maximum value) for $Re = 4000$ (left column) and $Re = 8000$ (right column) at different wave phases ωt. First row: linear stability analysis. Second and third rows: DNS results. In the DNS results, only a portion of the computational domain is shown. In the left column, the post-reversal mode is the dominant instability mode. In the right column, the pre-reversal mode dominates. The horizontal and vertical coordinates in each panel are normalized by the boundary layer thickness δ [76].

Sumer et. al. [93] reported the boundary layer under a solitary wave has three flow regimes based on the Reynolds number. For low Reynolds number there is a laminar regime, as the Reynolds number is increase the laminar regime begins to form a regular array of vortex tubes near the bed over short periods of time during the deceleration stage, and at moderately high Reynolds number the transitional regime is characterized by turbulent spots that caused spikes in the bed shear stress.

Diamessis & Redekopp [19] examined time-dependent boundary layers induced by weakly nonlinear solitary internal waves, of depression and elevation, in shallow water using high order direct numerical simulations. It was seen for waves exceeding a critical amplitude, global instabilities occurred in regions near the bottom boundary leading to the periodic shedding of coherent vortical structures that ascend high into the water column. The accompanying strong bottom shear stress suggests that solitary waves can induce unstable bottom boundary layers that can lead to benthic turbulence, mixing and sediment resuspension. Additionally, it was observed that the critical wave amplitude was diminished as the Reynolds number of the flow was increased. For ISWs typical of the open ocean and lakes, this would be a typical phenomena.

In numerical simulations by Rivera et. al. a detailed study of bed failure due adverse pressure gradients induced by the passing of an ISW of depression was perfromed. It was shown that the adverse pressure gradient imposed by the wave made resuspension of particles easier by reducing the specific weight of the bed [74]. This further suggest that ISWs are capable of lifting sediments and nutrients from the bed, high into the water column especially

when instability is coupled with the affect of the adverse pressure gradient.

Oscillatory Boundary Layers

In an experimental study by Carstensen, Sumer & Fredsoe [11] instabilities
in the boundary layer of an oscillatory flow were observed to generate vortex
tubes. The vortex tubes were described as being a result of the culmination
of vorticity generated by Kelvin-Helmholtz instability in the shear layer. This
culmination occurred after the near bed flow reversal (i.e. $\omega t > 135°$, where
$\omega t = 90°$ is defined $u_\infty(\omega t) = max(u)$ and u_∞ is the free stream velocity).
This type of instability was only observed for flows with $Re > 7 \times 10^4$.

The laminar oscillatory flow velocity profile is given by Batchelor [4],
details of which can also be found in Johnsson et. al. [46], which also
considers turbulent oscillatory boundary layers.

$$\frac{u(z,t)}{U_{0m}} = sin(\omega t) - exp(-\frac{z}{\delta})sin(\omega t - \frac{z}{\delta}) \qquad (1.19)$$

where it can be seen that the flow experiences an inflection point for $\omega t > 135°$. Here δ is the stokes boundary layer thickness, given by

$$\delta = \sqrt{\frac{2\nu}{\omega}}. \qquad (1.20)$$

The instability is shown to be active after the flow reversal which can be
explained by Rayleigh's inflection point theorem that states that the base
flow must have an inflection point in order for there to be a shear instability.
Since there is only an inflection point after the flow reversal it makes sense

that this is where instabilities would be more active. It is important to note that the bed shear stress in the laminar oscillatory flow leads the free stream velocity by 45 degrees [65] [46]. If this statement can be extended to the mode-1 internal tide in a spatial sense this may be helpful in determining a preferential location for instabilities.

In addition to the vortex tubes it was also observed that arrow head shaped turbulent bursts, typical of laminar to turbulent transitional regimes, appeared for $Re_{cr} = 1.5 \times 10^5$. In experiments run with both the oscillatory flow and a background current, it was seen that the Re range for which vortex tubes were observed was unchanged and for turbulent bursts $Re_{cr} = 3.5 \times 10^4$. The magnitude of spikes in the shear bed shear stress due to instabilities in the flow were much larger than the maximum bed shear stress associated with the maximum free stream flow velocity. The spikes in the shear stress can have a significant implication for sediment ressupension and transport[11].

The PIV experiments conducted by Mujal et. al.[62], oscillatory flows over smooth and rough boundaries were examined. It was shown that smooth bed flow is populated by vortex-tube structures that are formed due to the Kelvin-Helmholtz instability, similar to the experiments conducted by Carstensen. The rough wall experiments were populated by three types of coherent structures, vortices randomly distributed in space, turbulent bursts and shear layers of vortices originating due to flow separation at the bed. It was observed that instabilities were typically generated near the flow reversal close to the wall before the free-stream flow reversal. The evolution of the instability can be seen in figure 1.12. Vortex tubes are marked with ellipse and turbulent burst are marked with rectangles. During the second half cycle, where an-

other near-wall flow reversal occurs, vortices present from the previous half
cycle were able to merge and migrate upwards while new structures were
formed near the wall. The migration of the instability is an important char-
acteristic of the oscillatory boundary layer instability which is not found in
the solitary wave boundary layer.
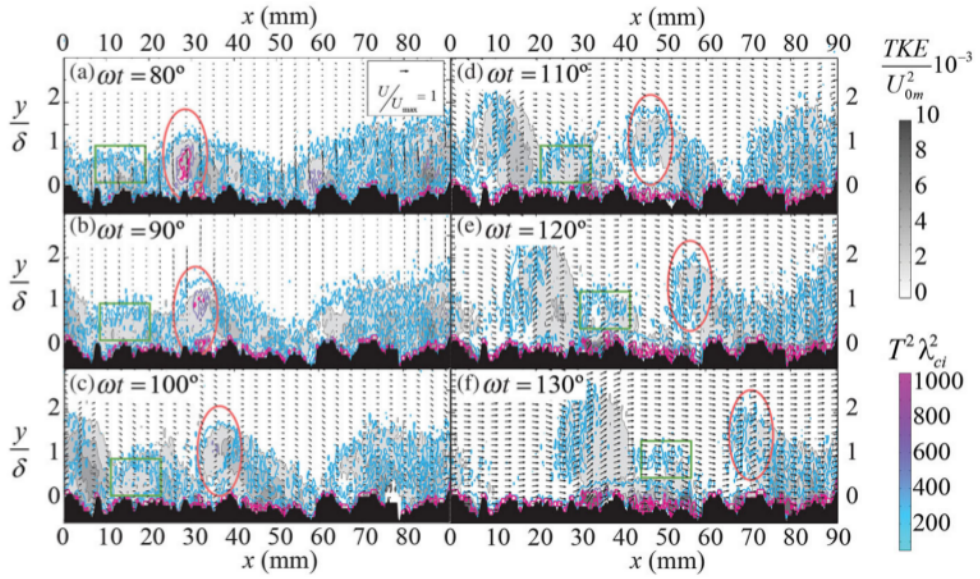
Figure 1.12: Phase evolution of the position of a vortex (ellipse), and a
turbulent burst (rectangle) for PIV experiments conducted by Mujal-Colilles
et. al. The backgound variable is the nondimensional turbulent kinetic
energy and the contour variable is the nondimensional swirling strength,
$T^2\lambda_{ci}^2$.

1.3.3   Objectives

The primary objective of this study is to understand how the bulk wave
parameters impact the instability properties of the bottom boundary layer
under a model mode-1 internal wave propagating in a horizontal wave guide.
To formally describe the instability properties the following objective are set:

- Describe the structure of the boundary layer base flow and identify any regions that may be prone to instabilities.

- Perturb the boundary layer with varying initial perturbation amplitudes to identify the critical perturbation amplitude, A_c, required for instability for a given set of wave parameters.

- Describe qualitatively the initial instability by examining the spatial structure and evolution of that instability.

- Calculate the average perturbation energy growth rates for each set of wave parameters.

- Determine a stability criterion as a function of the wave parameters.

The remainder of the thesis is laid out as follows. A discussion of shear instability fundamentals is given in chapter 2. In chapter 3 the governing equations, wave parameters and nondimensional parameters are discussed. In addition the simulation description is also given, outlining the process of forcing the wave field to generate the mode-1 waves as well as the method used to insert perturbations into the boundary layer. A short discussion on the numerical method is then given in chapter 4. The results are then presented in chapter 5 where a detailed discussion of the boundary layer structure is give. The instability structure and evolution as well as the linear growth rates are then discussed and finally a stability boundary constructed. Lastly, the discussion and conclusions are given in chapters 6 and 7 respectively.

Chapter 2

Shear Instabilities: Fundamentals

Strong shear is a dominant characteristic of the bottom boundary layer (BBL) induced by the interaction of the low mode internal tide flow field with the no slip boundary condition at the bed. It is therefore important to understand the effect of shear on the subsequent evolution of the BBL. Shear flows are ubiquitous in nature and can occur on a large range of scales, from blood flow through veins O[0.1-1 mm][41] to atmospheric and oceanic boundary layers O[10-100km] to accretion disks O[10-100 ly]. Shear, defined as the amplitude of the local velocity gradient in the direction perpendicular to the motion, can be represented in Einstein notation as

$$S_{ij} = \frac{\partial u_i}{\partial x_j}, \; for \; i \neq j. \tag{2.1}$$

The process of extracting energy from the background flow as a source for perturbation energy growth is known as an instability, in particular an instability that is due entirely to the spatial variation in the velocity, or shear, is known as a shear instability. Shear is a well known driver of instability and can be thought of as a reservoir of kinetic energy, which under the correct circumstances can be tapped into [28]. The question is what are the circumstances that are required to extract energy from this reservoir, especially in complex flows. To start to understand how we might answer this question let us first look at some simplified cases.

2.0.1   Parallel Shear Flows: Method of Normal Modes

The simplest class of shear flows that generate shear instabilities are parallel shear flows, defined as a flow whose velocity changes only in the direction perpendicular to the motion. This class of shear flows consists of wakes, jets, boundary layers and shear layers.

If we assume that the flow is inviscid ($\nu = 0$), homogeneous ($\rho = \rho_0$) and the Coriolis effects are negligible ($f = 0$) then the equations of motion become

$$\nabla \cdot \mathbf{u} = 0, \tag{2.2}$$

and

$$\frac{D\mathbf{u}}{Dt} = -\nabla p, \tag{2.3}$$

where $\mathbf{u} = (u, v, w)$ is the velocity vector and p is the pressure. Then, by assuming that the velocity field consists of a steady parallel shear flow $\mathbf{u} = U(z)\hat{e}^k$ plus a perturbation, where a prime denotes a perturbation, as

$$\mathbf{u} = U(z)e^k + \mathbf{u}', \tag{2.4}$$

$$p = P + p'. \tag{2.5}$$

It can be shown that a single equation for w' can be written as (details can be found in [89]):

$$\frac{\partial}{\partial t}\nabla^2 w' + U\frac{\partial}{\partial x}\nabla^2 w' = U_{zz}\frac{\partial w'}{\partial x}. \tag{2.6}$$

The normal mode solution of equation (2.6) can be written as

$$w' = \hat{w}(z)exp\{i(kx + ly - \omega t)\}. \tag{2.7}$$

The normal mode solution can alternatively be rewritten in terms of either the growth rate $\sigma = i\omega$ or the streamwise phase speed $c = \omega/k$. Substituting the normal mode solution into equation (2.6), we obtain Rayleigh's equation, the second order ordinary differential equation for $\hat{w}(z)$,

$$\sigma\nabla^2\hat{w} = -ikU\nabla^2\hat{w} + ik\frac{d^2U}{dz^2}\hat{w}, \tag{2.8}$$

where

$$\nabla^2 = \frac{d^2}{dz^2} - \tilde{k} \tag{2.9}$$

and $\tilde{k} = \sqrt{k^2 + l^2}$.

We can then see that equation (2.8) admits both wave like solutions, when σ is imaginary, and exponentially growing ($\sigma_r > 0$)) and decaying ($\sigma_r < 0$) solutions when σ is real.

Perturbation Energy Growth

From the perturbation momentum equation given by

$$\frac{D\mathbf{u}'}{Dt} = -\nabla p', \tag{2.10}$$

we can obtain the perturbation energy equation, per unit mass, by dotting with $\mathbf{u}'$. Horizontally averaging the equation results in the horizontally averaged perturbation kinetic energy equation

$$\frac{\partial K}{\partial t} = SP - \frac{\partial}{\partial z}EF \tag{2.11}$$

where

$$K = \mathbf{u}'^2 \tag{2.12}$$

and

$$SP = -\frac{\partial U}{\partial z}\overline{u'w'} \tag{2.13}$$

represents the shear production, the rate at which kinetic energy is transferred from the mean flow to the disturbance and the overbar denotes a horizontal average. The vertical kinetic energy flux is given by

$$EF = \overline{w'p'}. \tag{2.14}$$

The flux strictly transports the perturbation kinetic energy in the vertical. The convergence or divergence of the energy flux causes energy to either accumulate or be depleted at that height.

Alternatively, the time evolution of the horizontally averaged perturbation kinetic energy for a normal mode instability (2.7) can also be written in terms of the growth rate as

$$\frac{\partial K}{\partial t} = \sigma_r K \qquad (2.15)$$

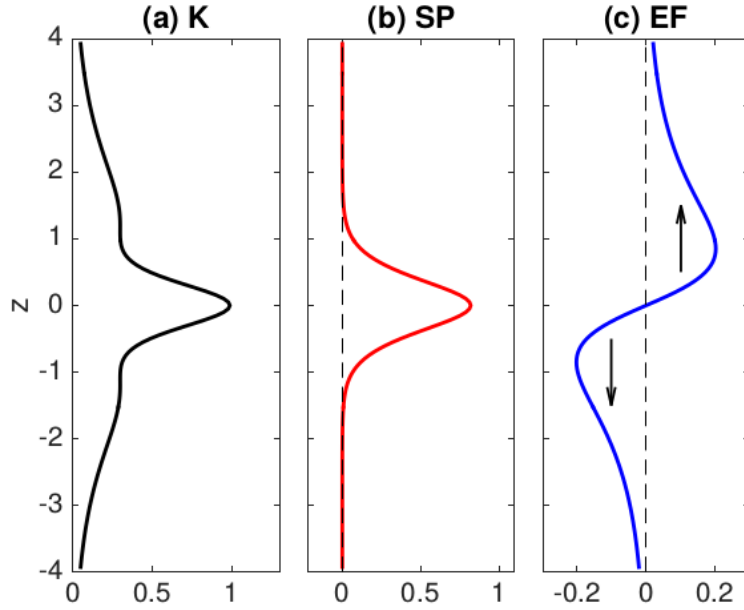Figure 2.1: The perturbation kinetic energy (K) for the instability of a hyperbolic tangent shear layer. The kinetic energy (a) is the sum of the energy being produced via shear production (b) and then transported by the energy flux (c) in the vertical. The convergence or divergence of the energy flux causes energy to either accumulate or be depleted at that height. Chapter 3 of Smyths notes [89].

Necessary Conditions for Instability

It can be shown that there exists four necessary conditions for instability in a invisid parallel shear flow, for more details refer to Smyth's Notes [89]:

- The mean velocity profile must have an inflection point (Rayleigh Inflection Point Theorem section 2.0.1)

- The inflection point must represent a maximum (not a minimum) of the absolute shear

- The mode must have a critical layer,$U(z) - c_r = 0$ (a corollary of Howard's semicircle theorem [44], more detail is section 2.0.2)

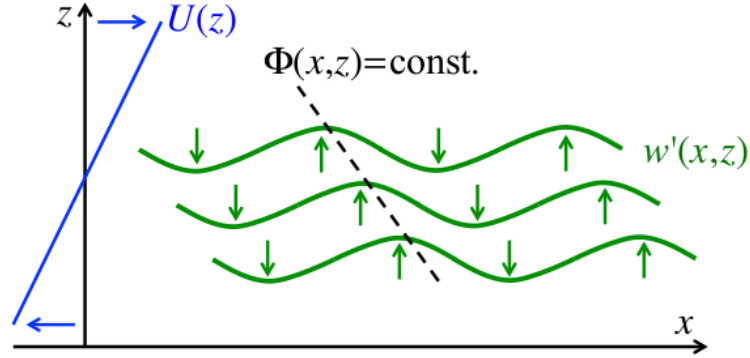- The phase lines of w' must tilt against the mean shear. Schematic in figure 2.2.

Figure 2.2: Schematic of a vertical velocity field showing how phase lines (black) tilt against the sheared background flow (blue). Schematic found in Smyths notes [89].

There also exist three "rules of thumb" that apply to the fastest growing instability of every parallel shear flow:

- The fastest growing mode is two dimensional, i.e. the wave vector is parallel to the mean flow ($l = 0$).

- The growth rate is proportional to U_0/h, where h is the thickness of the shear layer and U_0 is a velocity scale characteristic of the mean flow $U(z)$

- the wavelength is proportional to h

Rayleigh's Inflection Point Theorem Instability requires that the net shear production be positive since the only term that can generate perturbation energy in equation (2.11) is the shear production term,

$$\int SP dz > 0. \tag{2.16}$$

Since the shear production must be positive for some z, but must go to zero at the boundaries due to the no slip condition, then there must be a local maximum somewhere in the interior of the flow. The vertical derivative of the SP can be written as:

$$SP_z = U_z U_{zz} \left(\frac{SP}{U_z^2} + |\frac{\hat{w}}{U - c}|^2 \frac{\sigma_r}{2k^2} \right) \tag{2.17}$$

There are three factors in this expression and at least one of them must be zero. For a solution with a positive maximum of SP, U_z cannot be zero otherwise $SP = 0$ (2.13). The term in brackets is positive definite since $SP > 0$ and $\sigma_r > 0$. This leaves $U_{zz} = 0$, which is the result of Rayleigh's inflection point theorem [79], which states for an inviscid, homogeneous parallel shear

flow, a necessary condition for instability is that there exists an inflection point somewhere in the flow. Additionally, it can be shown that this inflection point must be a shear maximum in order for the flow to be unstable.

2.0.2   Stratified Shear Flows: Method of Normal Modes

For gravity waves to be supported in either the ocean or atmosphere there must be a density stratification. It then follows that we should consider how stratification affects shear instabilities. Stratification can effectively suppress instabilities by causing growing perturbations to do additional work against gravity. The competition between the shear, causing instabilities to grow, and stratification can be quantified using the local Richardson number,

$$Ri = \frac{N^2}{(\partial U/\partial z)^2}. \tag{2.18}$$

The value of the Richardson number that is required for instabilities to grow can depend on many details of the flow. However in general we can make arguments about the limiting cases, when the Richardson number is small ($Ri << 1$) than shear dominates, if it is large ($Ri >> 1$) stratification dominates[27].

Additionally, a bulk Richardson number can be defined that characterizes the shear flow using bulk parameters,

$$Ri_b = \frac{N_0^2}{U_0^2/h^2} \tag{2.19}$$

where N_0, U_0, and h are quantities representative of the stratification,

velocity, and length scales respectively of the background flow. This is typically done for convenience since it is much simpler to report one number based on bulk parameters of the background flow than a quantity that may depend non trivially on both space and time.

Linear Stability

To derive the perturbation theory, we start with the Boussinesq equations for an inviscid, non diffusive, inhomogeneous fluid, ignoring planetary rotation. The main consequence of the Boussinesq approximation is that the affects of the density differences is only important when it is multiplied by gravity. In order for the Boussinesq equation to hold the density differences must be small relative to the background density, that is

$$\rho = \rho_0 + \overline{\rho} + \rho', \tag{2.20}$$

and

$$\rho_0 >> \overline{\rho} >> \rho'. \tag{2.21}$$

The governing equations are then similar to the equations used for parallel shear flows with the addition of the gravity force and the density equation.

$$\nabla \cdot \mathbf{u} = 0, \tag{2.22}$$

$$\frac{D\mathbf{u}}{Dt} = -\frac{1}{\rho_0}\nabla p + \mathbf{F}_g, \tag{2.23}$$

$$\frac{D\rho'}{Dt} = 0, \tag{2.24}$$

where the gravity force acts only in the vertical:

$$\mathbf{F}_g = -g\frac{\rho'}{\rho_0}\hat{\mathbf{k}}.$$

In order to find solutions to the perturbation equations we follow a similar approach to that of the parallel shear flow. Assume that the velocity field consists of a steady parallel shear flow plus a perturbation. However, now also include a perturbation to the density field. It can then be shown that two equations can be found with two unknowns, w' and ρ', and can be written as (details can be found in [89]):

$$\left(\frac{\partial}{\partial t} + U\frac{\partial}{\partial x}\right)\rho' + \frac{\partial \rho'}{\partial z}w' = 0, \tag{2.25}$$

and

$$\left(\frac{\partial}{\partial t} + U\frac{\partial}{\partial x}\right)\nabla^2 w' - U_{zz}\frac{\partial w'}{\partial x} = \nabla_H^2 \rho'. \tag{2.26}$$

Then substitute the normal mode forms of w' and ρ' into the equations above, where the normal mode forms are given by

$$w' = \hat{w}(z)\exp i(kx + ly - \omega t), \tag{2.27}$$

and

$$\rho' = \hat{\rho}(z) \exp i(kx + ly - \omega t), \tag{2.28}$$

and the result is a set of ordinary differential equations:

$$(\sigma + ikU)\nabla^2 \hat{w} - ik\frac{d^2 U}{dz^2}\hat{w} = -\tilde{k}\hat{\rho}, \tag{2.29}$$

and

$$(\sigma + ikU)\hat{\rho} + \frac{\partial \rho}{\partial z}\hat{w} = 0, \tag{2.30}$$

and $\tilde{k} = \sqrt{k^2 + l^2}$.

As a result, it can be shown that a normal mode perturbation in a shear flow is effected only by the component of the background flow that is parallel to the perturbation wave vector. A detailed discussion of these results can be found in Smyth's notes [89]. It then follows that the fastest growing mode will be two dimensional and will have a wave vector that is parallel to the background flow. If we restrict our attention to the two dimensional modes parallel to the background flow then we can simply replace $\tilde{k}$ with k. Solving equation (2.30), for the eigenfunction $\hat{\rho}(z)$ and substituting into equation (2.29), at the same time replacing σ with $-ikc$ and rearranging, results in the Taylor-Goldstein equation:

$$\hat{w}_{zz} + \left(\frac{\partial \rho}{\partial z}\frac{1}{(U - c)^2} + \frac{\partial^2 U}{\partial z^2}\frac{1}{U - c} + k^2\right)\hat{w} = 0. \tag{2.31}$$

The Taylor-Goldstein equation describes a wide array of instabilities, and wavelike phenomena in stratified flows.

The Miles-Howard theorem

The Miles-Howard theorem states that although different flows may have different critical values of the Richardson number, Ri_c which defines the boundary between an unstable and stable flow, it is at most $1/4$. More precisely a necessary condition for instability in an inviscid, non diffusive, stratified, parallel shear flow is that $Ri < 1/4$ somewhere in the flow[44][89].

The semicircle theorem: In an inviscid, stably stratified, parallel shear flow, if the background velocity U(z) is bounded by U_{min} and U_{max}, then any unstable normal mode must have a phase speed located within the semicircle centered at $c_r = (U_{max} + U_{min})/2$, $c_i = 0$ with a radius, $r = (U_{max} - U_{min})/2)$. The result of the semicircle theorem then states that every unstable mode must have a critical level, $U(z) = c_r$ for some value of z[44] [89].

Perturbation Kinetic Energy

To analyze the perturbation kinetic energy, we again multiply the momentum equation (2.23) by $\mathbf{u}'$ and horizontally average. The result is similar to the non-stratified case with the addition of a term associated with the buoyancy

$$\frac{\partial K}{\partial t} = SP - EF_z + BF, \qquad (2.32)$$

where the buoyancy flux is given by

$$BF = -\overline{w'\rho'}g/\rho_0. \tag{2.33}$$

When buoyant fluid rises and dense fluid sinks, $BF > 0$. The BF term is then able to produce kinetic energy. In contrast, when $BF < 0$ the instability need to do work against gravity in order to grow, meaning it must lift dense fluid and depress buoyant fluid. When the stratification is stable ($\partial\rho/\partial z < 0$), a positive vertical velocity perturbation, $w' > 0$, will tend to move heavier fluid into lighter background fluid, $\rho' > 0$ and a negative vertical velocity perturbation, $w' < 0$, will tend to move lighter fluid into heavier background fluid, $\rho' < 0$. In a stable stratification it is thus more typical for the buoyancy flux term to be negative.

To make an analogy with the Richardson number criterion using energetic arguments, we can manipulate the perturbation kinetic energy evolution equation. Integrating the equation in the vertical, the energy flux term becomes zero because it it is purely a transport term ($EF = 0$), then equation can be rewritten as

$$\frac{\partial K}{\partial t} = SP(1 + BF/SP). \tag{2.34}$$

Since $BF < 0$ in a stably stratified fluid and we are interested in the case where the shear production is positive, it can be clearly seen that if the magnitude of the buoyancy flux is greater then the shear production the perturbation energy will decay.

Lastly, if we also include diffusion and dissipation the evolution of the

kinetic energy has two additional terms.

$$\frac{\partial K}{\partial t} = SP - EF_z + BF + \nu K_{zz} - \epsilon \qquad (2.35)$$

where νK_{zz} is the convergence of kinetic energy flux due to viscosity[89] and ϵ is the dissipation rate

$$\epsilon = \frac{\nu}{2}(\hat{u}_z^2 + \hat{v}_z^2 + \hat{w}_z^2 + 4\tilde{k}^2 K). \qquad (2.36)$$

Since the dissipation rate $-\epsilon$ is a negative definite quantity it always acts as a sink for perturbation kinetic energy.

Recall that each of the perturbation kinetic energy equations described thus far consider a purely parallel shear flow that does not vary in the horizontal direction or time. This means that the flux terms only act in the vertical. However, in flows that are spatially and temporally varying the steady normal mode analysis no longer applies. For the non steady case additional complications arise such as the flux of energy in the horizontal. Also each term can vary in time due to the temporal nature of the background flow and not only of the perturbations. Now a global instability analysis must be performed [79].

2.0.3   Time Dependent Shear Flows

In an unsteady flow, the background state varies with time as such a normal mode instability analysis no longer holds. More complicated analysis will need to be preformed for these types of flows, such as transient analysis, or

floquet. However, these types of formal mathematical analysis are beyond the scope of this research. Instead an empirical approach is considered.

Let us again consider how the steady parallel shear flow perturbation kinetic energy evolves. Recall equation (2.15), in which the perturbation kinetic energy is written in terms of the growth rate.

$$\frac{\partial K}{\partial t} = \sigma_r K \tag{2.37}$$

Here, it is clear that if $\sigma_r > 0$ then the flow will be unstable. However, now consider that the growth rate is a function of time, $\sigma_r = \sigma_r(t)$. It is no longer simple to say that if the growth rate is positive then the flow will be unstable, instead we must now specify that if $\sigma_r > 0$ for all time then the flow will be unstable. However, for different flow configurations requiring the growth rate to be positive for all time may be to strict. Instead there may be some way to relax our requirement for instability by considering the average growth rate that an instability is subjected to over a window of time when the growth rate is positive. The temporally averaged growth rate at a given can then be written as

$$\overline{\sigma_r} = \int_{t_i}^{t_f} \sigma_r(t) dt \tag{2.38}$$

where t_i and t_f are the initial and final time that the instability is subject to a positive growth rate. We can then rewrite the evolution of the perturbation kinetic energy as

$$\frac{\partial K}{\partial t} = \overline{\sigma_r} K \tag{2.39}$$

rearranging and integrating the equation results in the equation

$$ln(\frac{K_f}{K_i}) = \overline{\sigma_r}T_w \tag{2.40}$$

where $K_f = K(t_f)$ and $K_i = K(t_i)$ are the final and initial amplitude of the perturbation and $T_w = t_f - t_i$ is the total time that the instability is subject to a positive growth rate. Practically instability will only occur if sufficient instability growth can occur within the time scale of appreciable shear (i.e. where the shear is strong enough to cause positive growth rates)[98]. It then stands to reason that if a given flow requires some known amount of perturbation energy for the flow to be unstable, then we can define a stability criterion based on the expression in equation (2.40). There are some caveats here, the amount of perturbation energy required for the flow to be unstable can depend on both the flow and the exact definition of unstable that is used. Additionally, it can bee seen from equation (2.40) that the stability is also determined by the initial perturbation energy in the flow.

Chapter 3

Setup and Problem Geometry

In this thesis we will examine a model internal tide, with the primary objective of explaining the instability properties of the resulting bottom boundary layer. The model internal tide is studied by generating a mode-1 internal wave in a 2-D periodic domain with a horizontal free-slip top boundary and a no-slip bottom boundary. A schematic of the domain is shown in figure 3.1. A constant stratification is used. To generate the wave, the domain will be forced using "virtual paddles" which are essentially forcing functions added to the momentum equations. The forcing functions are determined using linear theory, a full discussion of which can be found in appendix A.

3.1   Governing Equations

The governing equations for the problem are the two-dimensional incompressible Navier-Stokes equations under the Boussinesq approximation (equations (3.1), (3.2), (3.3). The Boussinesq approximation states that density fluc-
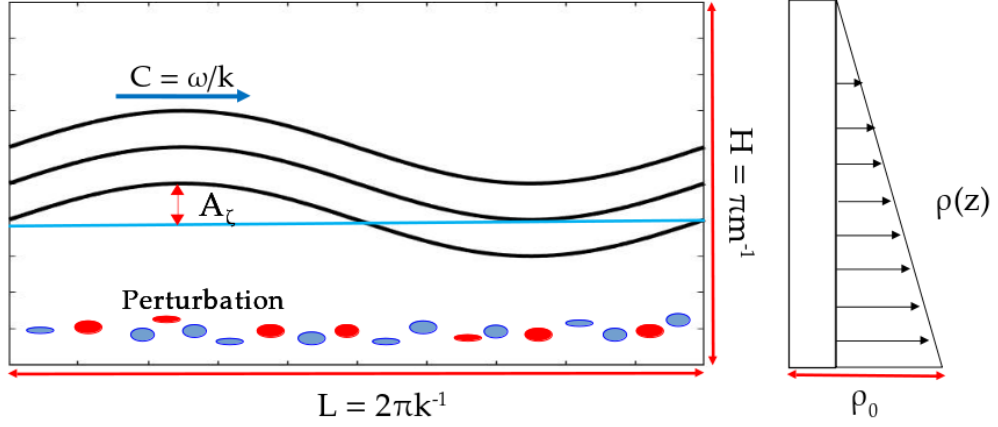
Figure 3.1: The mode-1 internal tide is generated in a 2D domain with periodic horizontal boundary conditions and a free slip top and no slip bottom boundary. Only a few isopycnals are shown in the domain for clarity but in reality the isopycnals extend all the way from the top to the bottom of the domain.

tuations are negligible except insofar as they affect buoyancy forces. This approximation can be invoked if the background density of the stratified fluid varies weakly over the depth of the fluid, a condition which holds for internal waves in the ocean where the density varies by only a few percent[94]. The full set of equations is

$$\frac{\partial \mathbf{u}}{\partial t} + \mathbf{u} \cdot \nabla \mathbf{u} = -\frac{1}{\rho_0} \nabla p + \mathbf{F}_g + \nu \nabla^2 \mathbf{u} + \mathbf{F_u}, \qquad (3.1)$$

$$\frac{\partial \rho'}{\partial t} + \mathbf{u} \cdot \nabla (\rho' + \bar{\rho}(z)) = \kappa \nabla^2 \rho' + \mathbf{F}_\rho, \qquad (3.2)$$

$$\nabla \cdot \mathbf{u} = 0, \qquad (3.3)$$

where the gravity force acts only in the vertical:

$$\mathbf{F}_g = -g \frac{\rho'}{\rho_0} \hat{\mathbf{k}}.$$

Here $\mathbf{u} = (u, w)$ is the two-dimensional velocity vector on the xz-plane, and ρ' and p denote the perturbation to the hydrostatic density and pressure respectively. Recall that according to the Boussinesq approximation, the instantaneous density is decomposed as

$$\rho(x, z, t) = \rho_0 + \overline{\rho}(z) + \rho'(x, z, t) \quad , \tag{3.4}$$

where

$$\rho_0 >> \overline{\rho}(z) >> \rho'(x, z, t). \tag{3.5}$$

Here ρ_0 is a reference density (refer to figure 3.1), $\overline{\rho}(z)$ is the background density and is chosen as a linear function of depth. The wave forcing terms are given by $\mathbf{F_u}$ and $\mathbf{F}_\rho$ which are defined in equation (3.7). The kinematic viscosity and mass diffusivity are denoted by ν and κ, respectively. In this study the Schmidt number $Sc = \nu/\kappa$ is always taken to be 1. Homogeneous Neumann boundary conditions (i.e. no-flux) for ρ' are applied at the top and bottom boundaries, while a no-slip bottom boundary and free-slip top boundary are applied for the velocity fields.

Wave Equations and Forcing

From linear theory, the method of vertical modes can be used to obtain equations for internal waves propagating in a horizontal wave guide. The ocean's

boundaries, sea floor and surface, act as a waveguide naturally confining the propagation of internal waves. Internal waves that propagate in such a wave guide have the character of a standing wave in the vertical, while it propagates in the horizontal. These properties are exploited in the method of vertical modes, which requires boundaries to be horizontal so that the solution can be obtained by a separation of the horizontal and vertical variables [37].

The solution to the linearized Navier-Stokes equations for a mode-1 wave propagating in a horizontal wave guide is written as follow (see appendix A for detailed derivation)

$$
\begin{aligned}
u(x, z, t) &= -\frac{am}{k} \cos{(mz)} \sin{(kx - \omega t)}, \\
w(x, z, t) &= a \sin{(mz)} \cos{(kx - \omega t)}, \\
\rho'(x, z, t) &= -\frac{a}{\omega} N_0^2 \frac{\rho_0}{g} \sin{(mz)} \sin{(kx - \omega t)}.
\end{aligned}
\tag{3.6}
$$

The forcing functions are then specified using similar relations to the wave solution, e.g.

$$
\begin{aligned}
F_u &= a_f \omega \frac{m}{k} \cos{(mz)} \cos{(kx - \omega t)} \\
F_w &= -a_f \omega \sin{(mz)} \sin{(kx - \omega t)}. \\
F_{\rho'} &= a_f N_0^2 \frac{\rho_0}{g} \sin{(mz)} \cos{(kx - \omega t)}
\end{aligned}
\tag{3.7}
$$

A similar method was employed by Slinn & Riley [88] to generate a planar internal wave incident on a slope. The strength of the forcing is set by

varying the amplitude parameter, a_f, as a piecewise time dependent forcing amplitude $a_f(t)$,

$$a_f(t) = \begin{cases} a_f & \text{if } t < T_f \\ 0 & \text{if } t > T_f \end{cases},$$

Where T_f is the time when the forcing is stopped and the wave reaches it target amplitude. A discussion of the forcing time can be found in section 3.3.1. A typical value of the wave forcing amplitude is

$$\frac{a_f}{U_0} = 0.01. \tag{3.8}$$

The value of the forcing amplitude is chosen to be small in order to reduce nonlinear affects during the forcing phase of the simulation. Despite the forcing amplitude being small, if T_f is large enough then large amplitude waves can be generated.

In the model both the velocity and density fields are globally forced (excluding the bottom boundary) in a manner that generates a mode-1 wave with specified frequency and wavenumber. This method offers several advantages such as allowing for the wave to developed a boundary layer in a way that is similar to a laboratory experiment [68]. Although the wave forcing terms are derived using linear theory, all waves generated were observed to have phase speeds that were consistent with linear theory. Additionally, no instability or significant wave dissipation was observed for waves that were allowed to propagate freely (i.e. without forcing), the wave form remained robust.

3.2 Wave Parameters

The results presented here address the relevant non-dimensional parameters that will ultimately determine the stability of the bottom boundary layer of a model mode-1 internal wave. In a linearly stratified finite depth horizontal waveguide, the model internal wave boundary layer is fully characterized by the set of parameters $\{k, m, N_0, A_\zeta, g, \rho_0, \nu\}$. Here k and m are the horizontal and vertical wavenumbers, refer to figure 3.1. The buoyancy frequency, N_0, of the base state is constant for a linear stratification, equation (3.10). The wave amplitude is denoted as A_ζ which is further defined in section 3.2.1. The remaining parameters are the acceleration due to gravity g, the reference density ρ_0, and the kinematic viscosity ν. The dispersion relation, given in equation (3.11), then sets the wave frequency, ω, and the wave induced velocities and density perturbation, for a free-slip bottom, are readily determined by the entire parameter set (excluding ν). From the set of dimensional parameters, we will construct the set of non-dimensional parameters that characterize the flow.

3.2.1 Dimensional Parameters

In this section we will discuss the dimensional parameters that have not yet been fully defined. These parameters include the wave amplitude, the characteristic velocity, the wave frequency, wave numbers, and base state buoyancy frequency. In order to define the relationship between the wave numbers and the wave frequency, we will write the dispersion relation for a model mode-1 internal wave explicitly. Once these parameters are defined,they will be used

to construct the non-dimensional wave parameters.

Dispersion Relation

The dispersion relation for a mode one internal wave coupled with the height of the water column and the base state buoyancy frequency, N_0, determines the relationship between the frequency, ω and the vertical wave number [37],

$$k = m\sqrt{\frac{\omega^2}{N_0^2 - \omega^2}}. \qquad (3.9)$$

Where $m = \pi/H$ and $k = 2\pi/L$ are the vertical and horizontal wave numbers. The domain height and length are given by H and L respectively and the base state buoyancy frequency is

$$N_0^2 = \frac{-g}{\rho_o}\frac{\partial \overline{\rho}}{\partial z}. \qquad (3.10)$$

The wave is set by fixing the domain depth and the buoyancy frequency while varying the domain length. Therefore, the free parameter is ω which leads to

$$\omega^2 = \frac{N_0^2 k^2}{k^2 + m^2}. \qquad (3.11)$$

Wave Amplitude

The displacement of a density surfaces from the reference density is given by

$$\zeta(x, z, t) = \frac{a}{\omega}\sin\left(m(z - \zeta)\right)\sin\left(kz - \omega t\right), \qquad (3.12)$$

a detailed derivation can be found in appendix A. It then follows that a simple definition for that amplitude of such a wave be described as the maximum isopycnal displacement induced by that wave, which is given by

$$\max \zeta = \frac{a}{\omega},$$
$$A_\zeta = \frac{a}{\omega}. \tag{3.13}$$

Where a is a free parameter with units of [m/s], which is ultimately determined by the forcing amplitude, a_f, and time, T_f.

Characteristic Velocity

The characteristic velocity of the internal wave field is the maximum horizontal wave induced velocity within the domain. From the method of vertical modes, the horizontal velocity field induced by an internal wave propagating in a horizontal wave guide is given by equation (3.6). The maximum horizontal wave induced velocity is then given by

$$U_0 = a\frac{m}{k}. \tag{3.14}$$

3.2.2   Non-Dimensional Parameters

Aspect Ratio

A useful non dimensional parameter to describe a given wave is the aspect ratio, defined as the ratio of the length to the height of the domain,

$$AR = \frac{L}{H}, \tag{3.15}$$

equivalently since a mode-1 wave has half a vertical wavelength, $m = \pi/H$, the aspect ratio written in terms of the wavenumbers is

$$AR = \frac{2m}{k}. \tag{3.16}$$

The range of aspect ratios tested in this study were $\{1,4,8,16\}$. However there was not significant instability observed for $AR = \{1,4\}$. Therefore the remainder of the study focuses on the higher range of aspect ratio, $AR = \{8, 16\}$.

Steepness

The steepness of a wave is a measure of how close the wave is to inducing a static instability. Static instability occurs when the local buoyancy frequency, N, given by

$$N^2 = N_0^2 - \frac{g}{\rho_0}\frac{\partial \rho'}{\partial z} \tag{3.17}$$

becomes negative. Given that the linear solution for the perturbation density field found using the method of vertical modes (appendix A) is

$$\rho' = -\frac{a}{\omega}N_0^2\frac{\rho_0}{g}\sin{(mz)}. \tag{3.18}$$

It can be show that static instability occurs when $A_\zeta m > 1$, by substituting equation (3.18) into equation (3.17).

$$N^2 = N_0^2(1 - A_\zeta m \cos{(mz)}\sin{(kx - \omega t)}) \tag{3.19}$$

This parameter is defined as the steepness, $st = A_\zeta m$[95].

An alternative way of writing the steepness is that it is the ratio between the maximum velocity induced by the wave, U_0, and the horizontal phase speed, C, of the model mode-1 internal wave. The steepness can then be rewritten as

$$st = \frac{am}{k}\frac{k}{\omega} = \frac{U_0}{C},\tag{3.20}$$

where $U_0 = am/k$ and $C = \omega/k$. This parameter is comparable to the Froude number defined by Fringer & Street, who observed that two-dimensional convective instabilities occurred when $Fr_{max} > 1$ [26], where $Fr_{max} = u_{max}/c \approx ka$ (section 1.3.1). As the steepness parameter approaches one, then the wave becomes more convectively unstable.

In the open ocean, where wave drag induced by the bed may be the dominate dissipation mechanism, it is unlikely that the low-mode internal wave become convectively unstable. In order for convective instability to occur (i.e. $st > 1$) the amplitude of the wave would need to be approximately 1/3 of the water depth ($A_\zeta = H/\pi \approx H/3$), which is unlikely in the open ocean. For the current study, the range of steepness parameters tested are between 0.1 and 0.5.

3.2.3   Isopycnal Slope

In addition to the steepness parameter, defined simply using bulk wave parameters, the directly related isopycnal slope can also be examined. The isopycnal slope, α, is computed by differentiating the isopycnal displacement, equation (3.12), with respect to the horizontal. The isopycnal slope depend

on the vertical and horizontal position since the isopycnal displacement due to the mode-1 wave is. A full discussion on the location and magnitude of the maximum isopycnal slope can be found in appendix B. In the discussion it is shown that the location and magnitude of the maximum isopycanl slope strongly depend on the steepness parameter. For $st << 1$ the amplitude of the maximum isopycanl slope is $\alpha \approx A_\zeta k$, and is approximately located at mid-water depth. For $st \to 1$,

$$\alpha = \frac{A_\zeta k}{1 - st},\tag{3.21}$$

and the location of the maximum slope is pushed towards the bed. Since the local isopycnal slope directly relates to the local buoyancy frequency, it can be seen that as the steepness is increased, the local buoyancy frequency near the bed is decreased, essentially reducing the local Richardson number in that region of the flow.

Reynolds number

The definition of the Reynolds number is chosen so that it is completely independent of the other two nondimensional parameters, and can therefore be varied independently. The Reynolds number is given by

$$Re = \frac{N_0}{\nu m^2}.\tag{3.22}$$

This definition of the Reynolds number is for limiting linear long waves and does not account for non-linearity of the wave. In the long wave limit (i.e.

$k << m$) the Reynolds number is given by

$$Re = \frac{CH}{\nu\pi} = \frac{AR}{\delta^2 m^2}.$$ (3.23)

Two Reynolds numbers are considered in this study and they are $Re = 5 \times 10^4, 2 \times 10^5$. These values of Re were chosen in order to capture a large range of Re_λ, which range from 7.76×10^4 to 6.21×10^5. Computational limitation set an upper bound on the Re, whereas the lower bound was determined by whether or not instabilities were observed in the simulations. Lower Re were tested however instabilities were not observed and therefore our focus is on the Re range where instabilities were present. In the ocean, typical Reynolds numbers are much higher than tested here, $O(10^6 - 10^8)$.

3.3   Simulation Description

In the following section a description of the simulations conducted is presented. Each simulation consists of a sequence of steps that create the wave and boundary layer. After the wave has been forced for sufficient time, so that the wave has reached a specified amplitude, the wave forcing is turned off. Perturbations are then inserted in the boundary layer to trigger any instabilities. This process is then repeated for each set of non-dimensional wave parameters. The set of wave parameters examined are given in table 3.1.

Table 3.1: Set of Wave Parameters Examined

Simulation	AR	st	Re
$AR8st2Re5$	8	0.2	5×10^4
$AR8st3Re5$	8	0.3	5×10^4
$AR8st4Re5$	8	0.4	5×10^4
$AR8st5Re5$	8	0.5	5×10^4
$AR8st1Re20$	8	0.1	2×10^5
$AR8st2Re20$	8	0.2	2×10^5
$AR8st3Re20$	8	0.3	2×10^5
$AR8st4Re20$	8	0.4	2×10^5
$AR16st1Re5$	16	0.1	5×10^4
$AR16st2Re5$	16	0.2	5×10^4
$AR16st3Re5$	16	0.3	5×10^4
$AR16st4Re5$	16	0.4	5×10^4
$AR16st5Re5$	16	0.5	5×10^4

3.3.1 Forcing Time

The steepness is measured at regular intervals by locating the maximum isopycnal displacement in the flow field as

$$A_\zeta = \frac{max[\rho']g}{N_0^2 \rho_0}. \tag{3.24}$$

After the desired steepness is reached the forcing is stopped and the perturbations are added to the BBL and the simulation is allowed to run without forcing.

3.3.2 Perturbation Field

In order for instabilities to arise, it is necessary to input perturbations into the BBL. A perturbation is required since the stability and accuracy of the high-order numerical method does not drive any numerical noise that could

cause the flow to go unstable. In numerical simulations conducted by Fringer & Street [26] it was assumed that the numerical noise in the method was of $O(10^{-8})$. In the current study the numerical method is spectrally accurate and any numerical noise is expected to be $O(\epsilon)$. Therefore the addition of perturbations are required for instability to be possible.

The perturbations that are inserted are divergence-free and have a red-noise spectra. The perturbation field is generate by first generating a pseudo-random white noise field on a uniformly spaced two dimensional grid. The two dimensional Fourier transform of that noise is computed and the Fourier coefficients are then scaled by $\mathbf{k^{-1}}$.

The perturbations are then windowed in the BBL using a Gaussian window, as to not disturb the entire flow field. This is done so that any instabilities that may arise outside of the boundary layer are not excited, and therefore cannot affect the BL dynamics. The Gaussian window is centered at the oscillatory boundary layer height given by

$$\delta_l = 5\delta, \tag{3.25}$$

and the standard deviation is set equal to the stokes boundary layer thickness

$$\delta = \sqrt{\frac{2\nu}{\omega}}. \tag{3.26}$$

The Gaussian window can then be written as follows

$$g(z) = A_0 \exp[-\frac{1}{2}(\frac{x - \delta_l}{\delta})^2] \tag{3.27}$$

where

$$A_0 = \frac{max[u_p]}{U_0} \tag{3.28}$$

is the initial amplitude parameter, defined as the maximum horizontal velocity perturbation, u_p, normalized by the maximum wave induced velocity. An example of the horizontal velocity spectra, at the center of the Gaussian window, of a typical initial noise field is shown in figure 3.2. Whether or not
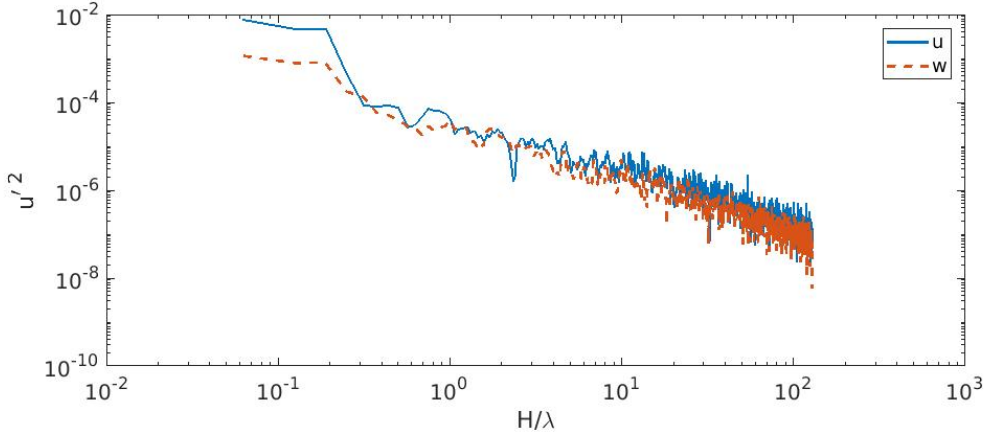

Figure 3.2: The spectrum of the initial noise field.

the simulation experiences overturning, is strongly dependent on the initial amplitude of the perturbation. Therefore, for each set of wave parameters, multiple values of A_0 are used in order to find the critical amplitude, A_c, that for $A_0 < A_c$ does not overturn and $A_0 > A_c$ does produce overturning. Due to limitations in time and resources, A_c is identified to within one order of magnitude. If the simulation with $A_i = 10^i$ overturned and simulation A_{i-1} did not overturn this was sufficient to report $A_i = A_c$, further discussion can be seen in results.

3.3.3   Isolating the Perturbation Field

To calculate the amount of energy in the perturbation field requires isolating the perturbations from the background flow, which consists of both the internal wave and boundary layer components. In the study of internal solitary wave boundary layer instability conducted by Diamessis & Redekopp [19], all wave fields were kept stationary in the wave-fixed reference frame employed. However in this study, the wave field is not stationary and undergoes non-negligible dissipation over a single wave period.Thus, it is required that the background flow is computed under the same conditions as the flow that consists of the perturbation field. To isolate the background flow, the simulations are run without the insertion of perturbations. These runs are referred to as the unperturbed run and are reference using the subscript (up) where as the perturbed runs have the subscript (p). Both the perturbed and unperturbed simulations are run with the same fixed time-step to allow for exact and direct comparison at any time of interest. The difference between the perturbed and unperturbed simulations is the perturbation field,

$$\overrightarrow{U}'(x, z, t) = \overrightarrow{U}_p(x, z, t) - \overrightarrow{U}_{up}(x, z, t). \tag{3.29}$$

The energy growth in the perturbation field is then calculated at each point in space. The maximum perturbation energy within the flow field at each time, $E_m(t) = max[E(t)]$, is found and used to calculate the perturbation energy growth rate. The growth rate is defined as

$$\sigma(t) = \frac{1}{E_m}\frac{dE_m}{dt}, \tag{3.30}$$

which comes from rearranging equation (2.15). Integrating this equation over the window of time, T_w, where $\sigma(t) > 0$ yields

$$\int_{T_w} \sigma(t)dt = \int_{T_w} \frac{1}{E_m}dE_m$$
$$\overline{\sigma}T_w = \log\left(\frac{E_{m,f}}{E_{m,0}}\right), \tag{3.31}$$

where $\overline{\sigma}$ is the time averaged maximum perturbation energy growth rate.

$$\rho'(x, z, t) \tag{3.32}$$

The total perturbation energy is calculated as the sum of both the kinetic and available potential energy

$$E = K + P, \tag{3.33}$$

where $K = K(x, z, t)$ is the total kinetic energy given by

$$K = \frac{1}{2}(\rho u'^2 + \rho w'^2), \tag{3.34}$$

and $P = P(x, z, t)$ is the available potential energy given by

$$P = \frac{\rho'^2 g^2}{2\rho_0 N^2}. \tag{3.35}$$

The perturbation energy growth rate is then calculated by using a least squares fit to the natural log of the energy as a function of time, where the

model is

$$E(t) = E_0 \exp \overline{\sigma} t. \tag{3.36}$$

The linear fit is then given by

$$ln(E_{m,f}) = \overline{\sigma} T \cdot t + ln(E_{m,0}). \tag{3.37}$$

The computed slope over the initial linear growth region, is then regarded as the time averaged energy growth rate $\overline{\sigma}$.

Chapter 4

Method

4.1 Numerical Method

The numerical method used is a spectral multidomain penalty method for the simulation of high Reynolds number incompressible flows in vertically finite and horizontally periodic domains. A full discussion of the numerical scheme and its validation (through comparison of simulations of stratified turbulent wakes with non-zero net momentum with corresponding laboratory data) may be found in Diamessis et. al. Diamessis et al. [20]. Only a brief overview of the method is provided here.

The temporal discretization of the governing equations combines third-order stiffly-stable and backward-differentiation schemes with a dynamic high-order boundary condition for the pressure [49]. Thus, maximum temporal accuracy is attained and splitting errors at the vertical boundaries are minimized, as $O(\Delta t^2)$ accuracy is achieved in both velocity and pressure. In the periodic horizontal direction, Fourier spectral discretization is used with

$\hat{N}_x$ Fourier modes. In the vertical direction, the computational domain is partitioned into M subdomains of variable height H_k and order of polynomial approximation $\hat{N}_k$ ($k = 1, \ldots M$) (figure 4.1). The total number of vertical grid points is $\hat{N}_z = M(\hat{N} + 1) + 1$. Within each subdomain, a Legendre spectral discretization [6] is used and, for the specific problem under consideration, $\hat{N}_k$ is fixed and equal to a fixed $\hat{N}$ in all subdomains. Subdomains communicate with their neighbors via a simple patching condition [6]. Among others, the primary advantage of the multidomain discretization [40] is flexibility in local resolution which allows positioning of sufficient number of grid points in the boundary layer combined with minimal resolution of the less active ambient fluid outside the boundary region.
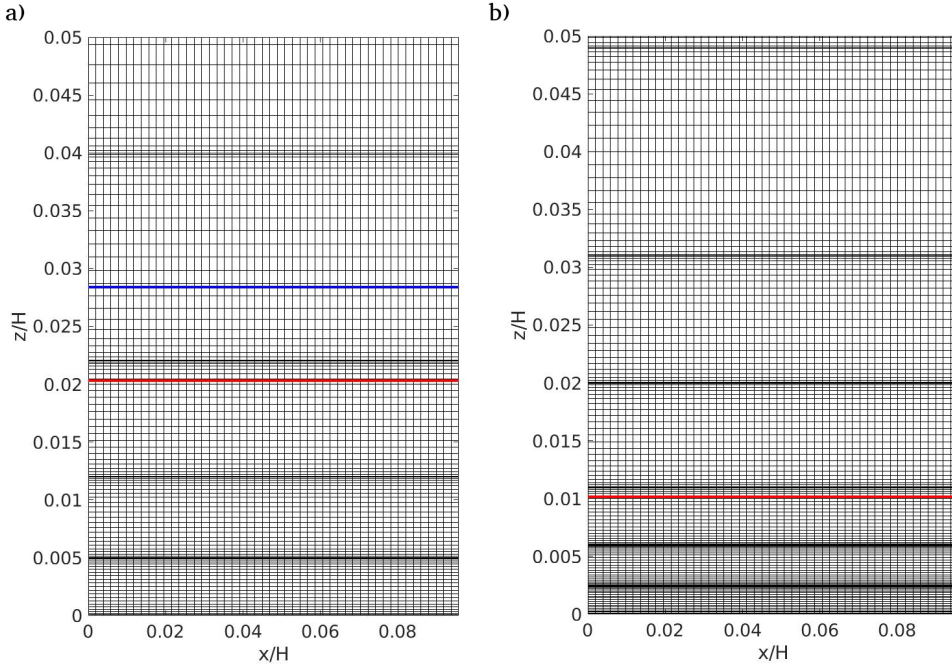
Figure 4.1: Section of the numerical grid employed in this study a) the low Reynolds number runs, where the vertical red and blue lines represent the height of the laminar boundary layer ($\delta_L = 5\sqrt{2\nu/\omega}$) for $AR = 8$ and $AR = 16$ respectively, b) is a section of the grid used for the high Re runs and the red line represent the height of the laminar boundary layer for $AR = 8$. The horizontal direction employs a spectral Fourier discretization and a uniform grid. In the vertical a Legendre spectral multidomain discretization is used with a) M = 14 and b) M = 18 subdomains with the polynomial order $\hat{N} = 25$ and a local Gauss–Lobatto–Legendre grid. Shown is the vertical grid point distribution for both level of Re. Subdomain origins are at z/H = 0 , 0.005, 0.012, 0.022, 0.04, 0.07, 0.12, 0.22, 0.37, 0.52, 0.67, 0.82, 0.92, 0.97 and z/H = 0, 0.0025, 0.006, 0.011, 0.02, 0.031, 0.49, 0.069, 0.089, 0.119, 0.16, 0.24, 0.37, 0.52, 0.67, 0.82, 0.92, 0.97

The resolution is chosen as to capture all relevant phenomena, especially focusing on the dynamics of the instabilities. Spectral filtering is applied to ensure that no numerical instabilities or subsequent aliasing effects develop due to lack of sufficient interpolating polynomial modes. Testing to

determine whether the grid configuration was sufficient to fully resolve the instabilities was accomplished by visual inspection of the horizontal spectra for all instabilities. If the wavenumber of the instability was not affected by the filter (see figure 4.2) then it was determined that the grid was sufficient to fully resolve the relevant physics. In the vertical direction, as long as there were at least 12 point across the amplitude of the isopycnal displacement induced by the instability it was determined that the resolution was sufficient. In addition, grid independence tests were done in which the resolution in both directions was increased; since there was no visible difference in the structural characteristics of the instability it was determined that the grid was sufficient to resolve the scales of the instabilities. Typical instability wavelength are $O(0.05)$ which is approximately 25 horizontal grid points.

The grid that was used in the low Reynolds number simulations were $\hat{N}_x \times \hat{N}_z = 4096 \times 350$, where n_x and n_z are the total number of points in both the horizontal and vertical directions respectively. For the high Reynolds number simulations a grid with increased vertical resolution, specifically increasing the resolution in the boundary layer, was used where $\hat{N}_x \times \hat{N}_z = 4096 \times 450$. The arrangement of the vertical subdomains can be seen in figure 4.1, where the subdomains concentrated in the boundary layer are visible.

To ensure stability of the numerical solution, while preserving its spectral accuracy, penalty techniques [40] are used in the vertical direction along with strong adaptive interfacial averaging [21]. As a final safeguard against numerical instability, explicit spectral filtering is used in all spatial directions [54]. The filtered solution can be expressed in terms of the modes of the

numerical solution as

$$f^F(z_i) = \sum_{j=0}^{N_k-1} \sigma(k_j)\tilde{f}_j P_j(z_i) \tag{4.1}$$

where k_j is the jth discrete Legendre mode. The exponential filter function used is

$$\sigma(k_j) = exp[-\alpha(\frac{k}{N})^p] \tag{4.2}$$

where p is the filter order and $\alpha = -ln\epsilon)_M$ with ϵ_M being the machine precision. Application of the filter function (4.2) is equivalent to introducing a pth-order hyperviscous operator in the governing equations [6][40] [19]. The advantage of the explicit application of a filter is that it avoids the additional stiffness and subsequent time step limitations of a hypervisous term[19]. An analogous filtering procedure is applied in Fourier space. The exact filter functions used in both directions is shown if figure 4.2.
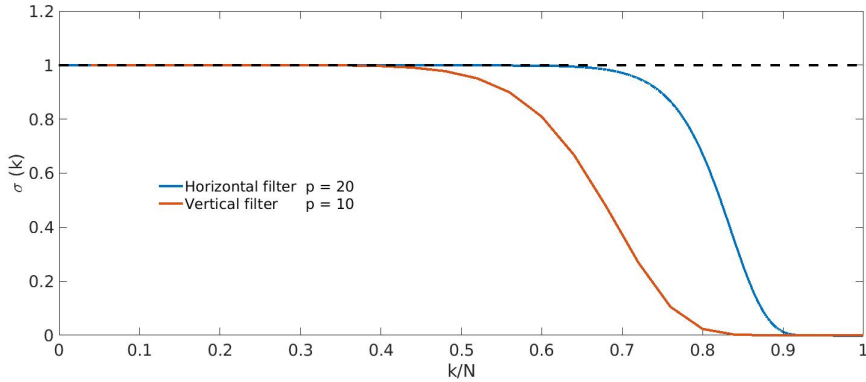

Figure 4.2: Exponential filter functions $\sigma(k/\hat{N})$ for different filter orders p. The mode number and total number of available modes (over the full domain in Fourier space and over a single subdomain in Legendre space) are denoted by k and $\hat{N}$, respectively.

In regards to the flow under consideration, the above numerical scheme provides two distinct advantages. First, the temporal discretization, when combined with a spectral spatial discretization, provides maximum temporal accuracy at the boundaries [38] and the solution is not contaminated by the formation of splitting-induced spurious numerical boundary layers [6]. Second, the penalty scheme allows the simulation of the "inviscid" physics of the wave-induced boundary layer (provided sufficient grid points are inserted therein) without requiring resolution of the thin viscous sublayer, which would require a prohibitively high number of grid points. Thus, the internal (internal with regards to the viscous sublayer) inviscid high Reynolds number physics of the flow are captured with spectral accuracy without having to worry about under-resolution-driven numerical instabilities. No enhanced numerical viscosities, which will bias the internal flow dynamics when using a spectral scheme [7], are required. In addition, the excessive artificial dissipation of a low-order finite difference scheme, which can damp features at the smallest resolved scales essential to the instability is not an issue.

Chapter 5

Results

5.1 Boundary Layer Structure

The structure of the boundary layer under a mode-1 internal wave has many key features that are similar over the range of wave parameters tested. A key feature of baroclinic oscillatory boundary layers that is present in the barotropic case is, the maximum wall shear is ahead of the maximum wave induced velocity (i.e. the crests and troughs)[11][46]. For the laminar barotropic oscillatory boundary layer it can be shown that the phase shift of the shear stress over the velocity is $\pi/4$ and that the boundary layer profile is anti symmetric in the sense that $U(x, z, t) = -U(x + \pi k^{-1}, z, t)$[4][97]. Upon inspection of the boundary layer under the model mode-1 internal wave it is shown that the anti symmetry is broken (figure 5.1). However, the phase lead of the maximum shear over the velocity is approximately the same as the barotropic wave.

In figure 5.1, the velocity vector field is plotted along the entire length

of the boundary layer for the bottom 4% of the water column. Notice that underneath the crests (rightward pointing velocity) and the trough (leftward pointing velocity) the vertical velocity profile looks similar to a flat plate boundary layer, whereas at the $\pi/2$ phase shifts (from the crest and trough) there is a region with a strong flow reversal similar to the observations of the barotropic oscillatory boundary layer by Mujal-Colilles et. al. [62] discussed in section 1.3.2. The flow reversals are inflection points in the vertical profile of the horizontal velocity and these inflection points are local maximums of vertical shear, these region therefore satisfy Rayleigh's inflection point theorem for parallel shear flow instabilities.

The breaking of the anti symmetry of the bottom boundary layer under the mode-1 internal wave indicates that a given region may be more susceptible to instabilities than its half wave period counter part (i.e. phase shifted $\pm\pi$). The breaking of the anti symmetry of the boundary layer is evident by the difference in length of the flow reversal regions ahead of both the crest and the trough of the wave. By visual inspection it appears that the length of the flow reversal ahead of the crest of the wave is about 1.5 times longer than the flow reversal region ahead of the trough, for the $AR16st5Re5$ simulation in figure 5.1. This is important because the length of the strong shear region is directly related to the amount of time that instabilities developing in that region will be subject to low Ri as the wave propagates past. Therefore the non anti-symmetry of the wave BBL indicates that the region characterized by a relatively long region of strong flow reversals and high shear ahead of the crest may be a preferential region for instability.
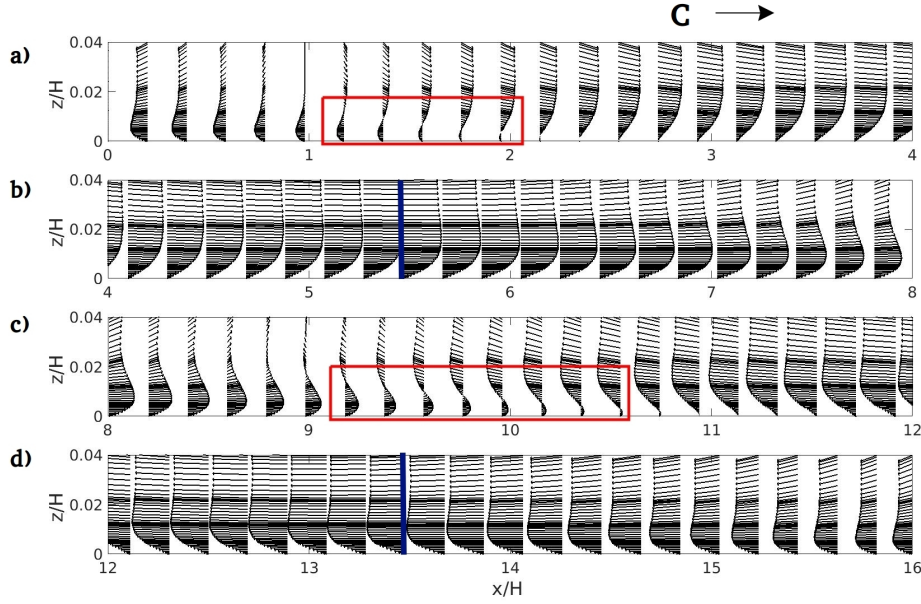
Figure 5.1: Velocity vectors in the BBL under a model mode 1 internal tide for the $AR16st5Re5$ simulation. Boxed regions correspond to the high shear regions, where inflection points in the flow are easily visible. In a) and c) the boxed inflection points corresponds to the regions ahead of the trough and crest of the wave respectively. The crest and trough are marked by vertical blue lines in b) and d) respectively. The wave is moving from left to right and the domain is periodic.

Figure 5.2 shows contour plots of both the horizontal and vertical velocity fields as well as the density field for simulation $AR16st5Re5$. In the contour of the horizontal velocity it can be seen that the effects of the boundary layer extend high into the water column, between 5% and 6% of the water depth. In the free-slip case the horizontal velocity field defined in equation (3.6) has anti symmetry. Recall, the horizontal velocity is given by $u(x, z, t) = -\frac{am}{k} \cos(mz) \sin(kx - \omega t)$. Here there are no flow reversals near the bed, in addition there is very little vertical shear near the bed since $\partial u/\partial z \propto \sin(mz)$. Therefore, it is the interaction with the bed that breaks the anti

symmetry and induces both the shear and the flow reversal regions.

In the region of the BBL ahead of the crest of the wave the isopycnals are lifted and the vertical separation between isopycnals is progressively increased (spread) from their equilibrium levels. This spreading of the isopycnals decreases the local stratification which in turn decreases the associated stabilizing effect. At the crest of the wave where the isopycnal spreading is at its maximum, the local buoyancy frequency is minimum. Since the maximum shear and flow reversal regions are ahead of the crest of the wave, as the wave propagates any instabilities that may be generated in that high shear region will eventually be overcome by the wave crest (see discussion on instability phase speed in section 5.2). Therefore instabilities generated in the region where the destabilizing effects of shear are at a maximum will eventually move into a region where the stabilizing effect of the stratification are at a minimum. These two effects determine the region where instabilities can grow and thus the life time of those instabilities.

From the equation of the isopycnal displacement, equation (3.12), it can be seen that steepness of the wave is directly related to how much the isopynals are lifted and spread. The spreading of the isopycnals decreases the local buoyancy frequency. As the steepness of the wave is increased the length of the region where the shear is capable of overcoming the stratification is then also increased. This competition between the effects of the stratification and the shear can be fully described by the local Richardson number.
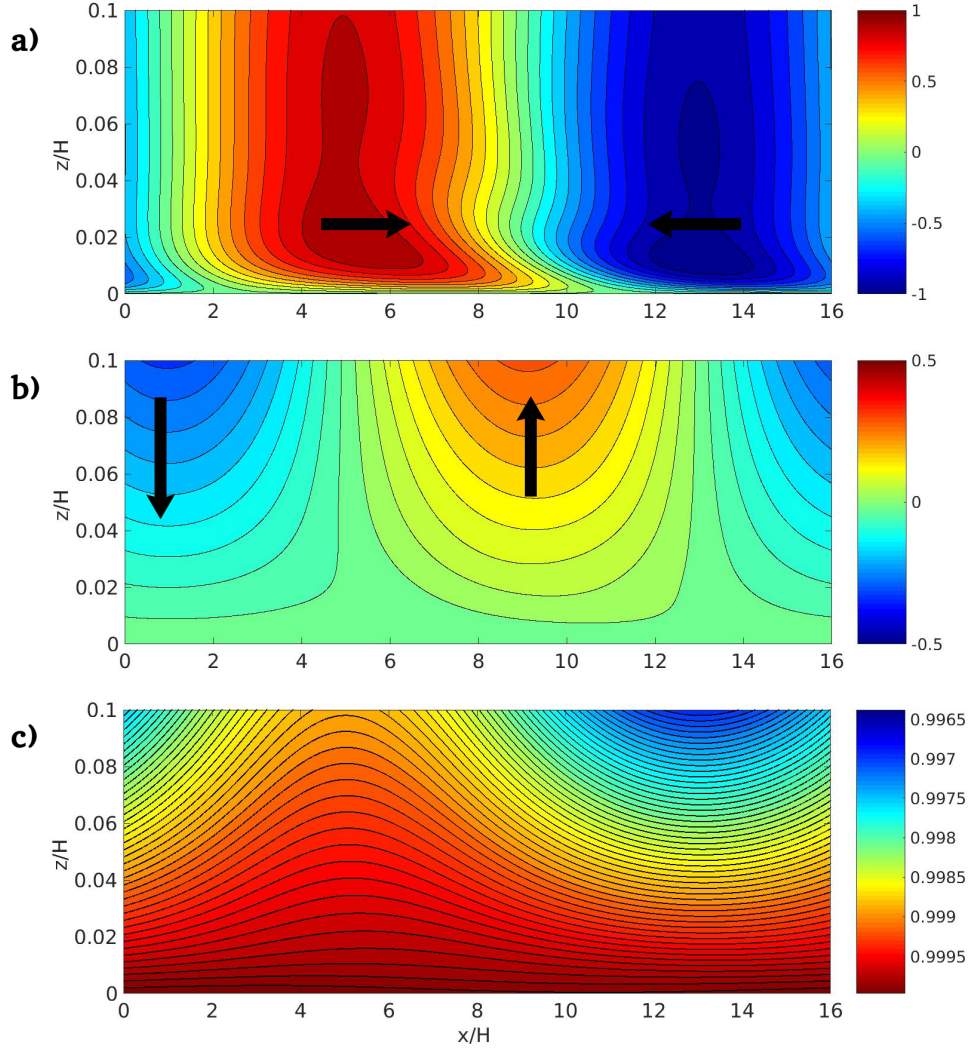
Figure 5.2: For a mode-1 internal wave with $AR = 16$, $st = 0.5$, and $Re = 5 \times 10^4$, (a) the horizontal velocity field U/U_0, (b) the vertical velocity field W/U_0, and (c) density field ρ/ρ_0 contour maps are plotted. The crest of the wave is located where the horizontal velocity is positive while the trough of the wave is located where the horizontal velocity is negative.

5.1.1   Length of High Shear Region

It is important to quantify the length of the high shear region since it is this length along with the horizontal phase speed of the background wave that determines the amount of time that an instability will have to grow. The length of the high shear region is defined as the length of the line that tracks the inflection point in the horizontal velocity profile, that is within a region where the Ri is below 1/4. A discussion of the Richardson number criterion is given in the following section. The contour lines that track the inflection point are defined as

$$\frac{\partial^2 U(x,z)}{\partial z^2} = 0. \qquad (5.1)$$

The line that tracks the inflection point is chosen since it is the maximum of the squared shear for the given vertical profile. Additionally, from parallel shear flow theory, in order for a flow to be unstable there must be an inflection point within the flow. Thus it is possible for instabilities to exist in the region where an inflection point exists.

Figure 5.3 shows both the contour line of the inflection point that exists within the region where $Ri < 1/4$ as well as the contour line for $Ri = 1/4$. It is seen that the length of this region is typically longer in the region in front of the crest than in the region infront of the trough. This indicates that the region infront of the crest is more likely to produce instabilities because any instabilities growing in this region will have more time to grow. However, it is not only the length of this region that determines if instability will be present it is also the magnitude of the Richardson number.
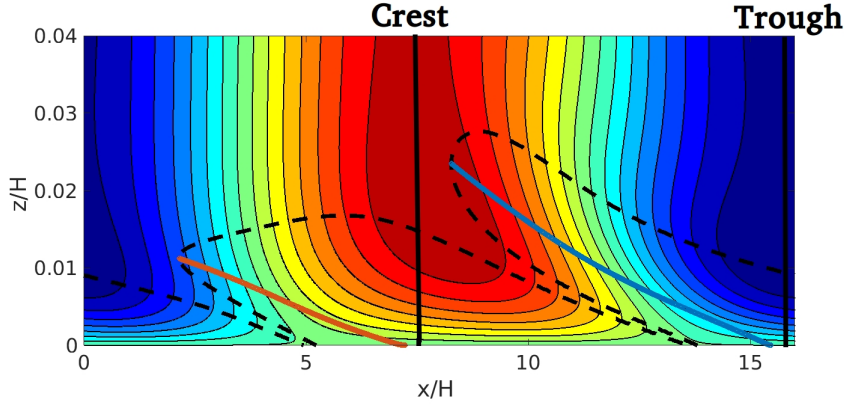
Figure 5.3: The blue lines mark inflection points in the horizontal velocity (i.e. $\partial^2 u/\partial z^2 = 0$). The black contour lines are where the Richardson number equals $1/4$. This figure is for the $AR8st5Re5$ run, however the picture looks qualitatively similar across the simulations.

The magnitude of the Richardson number will greatly impact the growth rate of the instability. Further discussion on the growth rates of the instabilities are found in section 5.3. The Richardson number along the inflection point line is plotted for the crest and trough separately in figure 5.4. It can be seen that the magnitude of the Richardson number along the line that tracks the inflection point that is in front of the crest has a much smaller magnitude then the line that tracks the inflection point that is in front of the trough. In order to account for the difference in the magnitude of the Richardson number along the line we can use a normalized (or weighted) length,

$$L_n = \overline{Ri}L_w, \tag{5.2}$$

where the non dimensional length of the low Richardson number region is given by

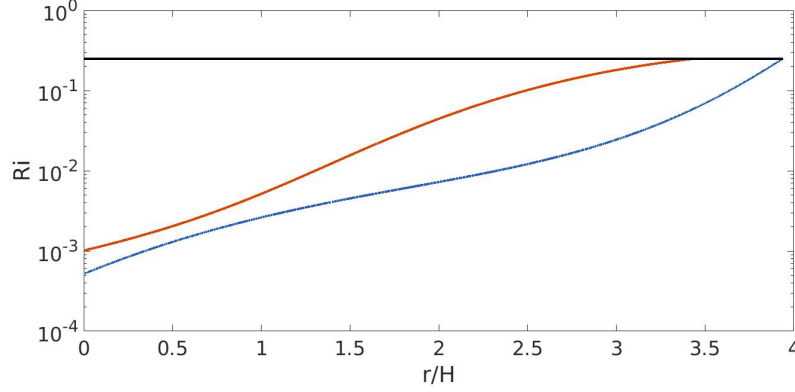$$L_w = \frac{1}{H} \int_{Ri < Ri_c} I(x, z)dxdz, \tag{5.3}$$

Figure 5.4: The Richardson number is plotted against the length of the line that tracks the inflection point curve, where r is the distance along that line starting from the point closest to the bed. The line tracking the inflection point in the region infront of the crest is in blue and for the region infront of the trough is in red.

and Ri_c is the critical Richardson number threshold and

$$I(x, z) \equiv U_{zz}(x, z) = 0 \tag{5.4}$$

is the line that tracks the inflection point. Finally, the normalization Richardson number (or the Richardson number weighting) is given by

$$\overline{Ri} = \frac{1}{Ri_c L_w} \int_{L_w} (Ri_c - Ri(x, z)) dL_w. \tag{5.5}$$

The normalization Richardson number is defined in such a way that if $Ri(x, z) = 0$ over the extent of the line then $\overline{Ri} = 1$ and if $Ri(x, z) = 0.25$ over the extent of the line then $\overline{Ri} = 0$. This weighting can be used to further show that the region in front of the crest is more prone to instability then the region infront of the trough. Table 5.1 has the values of the lengths, L_w, as well as the nor-

malization Richardson number, $\overline{Ri}$, listed for all of the simulations run. In general, as the steepness is increased for a set of wave parameters the length of the high shear regions, infront of both the crest and the trough, increases. Additionally, it is most instructive to compare the normalization Richardson number between the high shear regions in a particular simulation. The value $\overline{Ri}$ is almost always greater in the region infront of the crest. Finally, the weighted length of the high shear regions are plotted in figure 5.5 .

Table 5.1: Length of the high shear regions.

Simulation	Crest L_w	Crest $\overline{Ri}$	Trough L_w	Trough $\overline{Ri}$
$AR8st2Re5$	2.658	0.763	2.191	0.761
$AR8st3Re5$	3.290	0.822	2.614	0.785
$AR8st4Re5$	3.681	0.866	2.968	0.7805
$AR8st5Re5$	3.958	0.897	3.456	0.742
$AR8st1Re20$	2.328	0.765	2.125	0.767
$AR8st2Re20$	3.375	0.841	3.040	0.802
$AR8st3Re20$	3.853	0.8828	3.8476	0.774
$AR8st4Re20$	4.140	0.9049	6.494	0.649
$AR16st1Re5$	3.012	0.6915	3.121	0.703
$AR16st2Re5$	4.483	0.7361	3.941	0.759
$AR16st3Re5$	5.760	0.784	4.545	0.786
$AR16st4Re5$	6.566	0.828	4.760	0.786
$AR16st5Re5$	7.218	0.867	5.100	0.782

It is interesting to note that the value of the weighted length is larger in the region infront of the trough for the $AR8st4Re20$ simulation. However, the region in front of the crest is still the region that has instabilities (section sec:ISE). To give insight into why this occurs the Richardson number plot along the inflection point curves are plotted in figure 5.6. It can be seen that the magnitude of the Ri for the region infront of the crest is much lower up
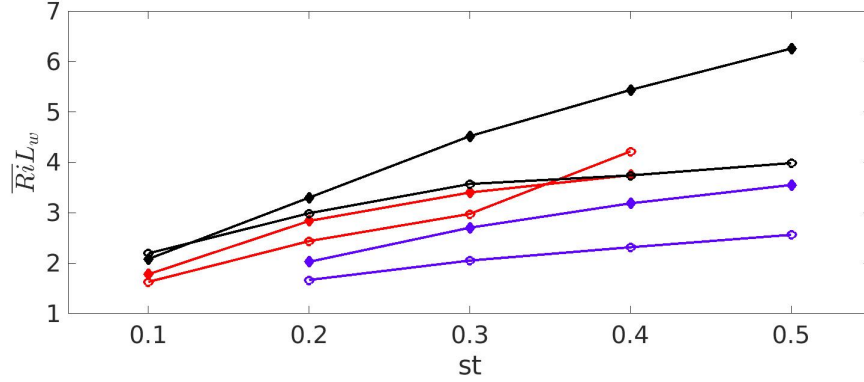
Figure 5.5: The weighted length of the high shear region infront of both the crest and the troughs are plotted against steepness for each set of wave parameters. The crest are marked with closed diamond and the troughs are marked with open circles while each set of AR and Re are as follows $AR8Re5$ blue, $AR8Re20$ red, and $AR16Re5$ black.

to about $r/H = 4$ where the Richardson number at the trough begins to plateau at $Ri \approx 0.1$. The reason that crest is still more prone to instability may be because the initial growth may be more important then the long time growth, or that the $0.1 < Ri < 0.25$ is not small enough to cause significant growth.

5.1.2   Richardson number

The gradient Richardson number is a measure of how strong the local stabilizing effect of the stratification is compared to the destabilizing shear, recall from equation (2.18) $Ri = N^2/(\partial U/\partial z)^2$, where $N = N(x, z, t)$ and $U = U(x, z, t)$ are the local quantities and

$$N^2 = N_0^2 - \frac{g}{\rho_0} \frac{\partial \rho'(x, z, t)}{\partial z}, \qquad (5.6)$$
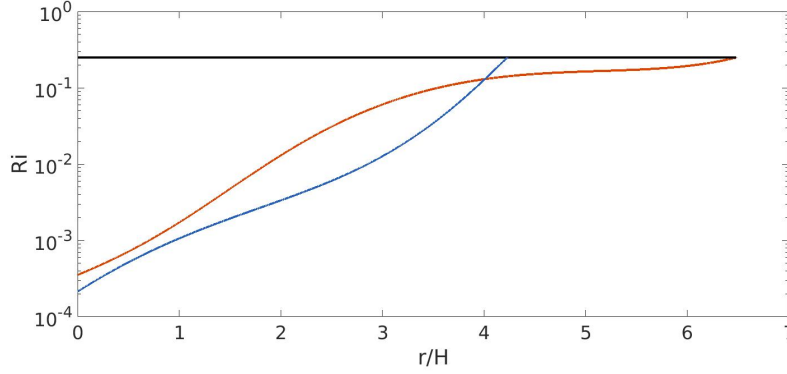
Figure 5.6: The Richardson number is plotted against the length of the line that tracks the inflection point curve, where r is the distance along that line starting from the point closest to the bed. The line tracking the inflection point in the region infront of the crest is in blue and for the region infront of the trough is in red.

where N_0 is defined in equation (3.10).

In figure 5.7, contours of subcritical gradient Richardson number ($Ri \leq 0.25$) are plotted over the horizontal velocity which is used as a reference to identify the relative location. The maximum contour line plotted, corresponds to $Ri_{cr} = 0.25$, is used to delineate regions where instabilities are possible. It is seen that the low Ri region extends higher into the water column in the region ahead of the wave crest than in the region ahead of the trough. The difference in the height of the low Ri regions is mostly attributed to the separation and compression of the isopycnals at the crest and trough respectively. Additionally, the low Ri region is elongated in the horizontal direction in the region ahead of the crest compared to the region leading the trough which is much narrower. The difference in the length of the regions is attributed to the difference in length of the high shear regions as well as the reduced buoyancy frequency at the crest of the wave (see section 5.1.1).
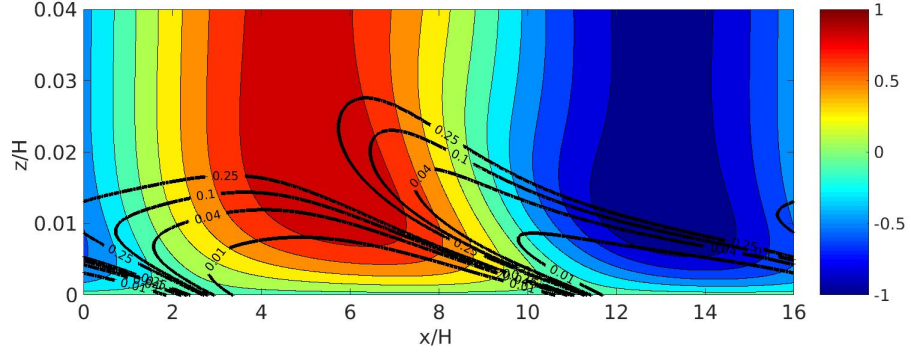
Figure 5.7: The $Ri = \{0.01, 0.04, 0.1, 0.25\}$ contours are plotted for the unperturbed state of $AR16st5Re5$, over the horizontal velocity U/U_0.

Wave Parameter Effect on Gradient Richardson Number Structure

It is also important to consider how the non-dimensional parameters of the wave affect the structure of the low Ri region. In figure 5.8, the $Ri = 0.25$ contour is plotted for various steepness values for each of the aspect ratios and Reynolds numbers considered. When comparing the two aspect ratios at a fixed Reynolds number, (figure 5.8 a and b) it is seen that the region where $Ri < 0.25$ for $AR = 16$ is about twice the length of the region where $Ri < 0.25$ for $AR = 8$. For the two Reynolds numbers considered for $AR = 8$ (figure 5.8 b and c) the low Ri number region is slightly longer for high Re, this is due to the increased shear associated with higher Reynolds numbers.
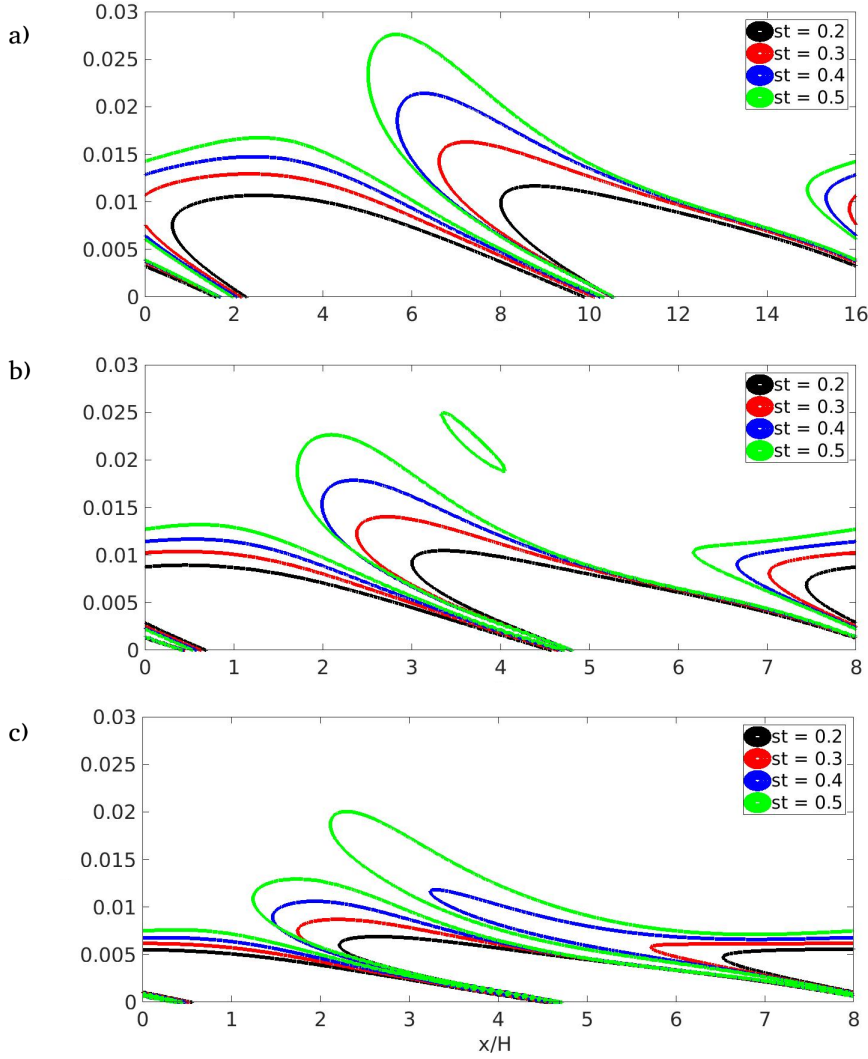
Figure 5.8: The $Ri_{cr} = 0.25$ contour line is plotted for various steepness levels for the fixed parameter values of; a) $AR = 16$, $Re = 5 \times 10^4$ b) $AR = 8$, $Re = 5 \times 10^4$ c) $AR = 8$, $Re = 2 \times 10^5$. The aspect ratio of subplot a) is twice that of b) and c).

Local Density Gradient   Neglecting boundary layer effects in the density field, the local Brunt–Vaisala frequency can be calculated simply by substituting the equation for the density perturbation field into equation (5.6).

Recall the density perturbation due to the background wave is

$$\rho'(x, z, t) = -\frac{a}{\omega} N_0^2 \frac{\rho_0}{g} \sin(mz) \sin(kx - \omega t). \tag{5.7}$$

It then follow that

$$N^2(x, z, t) = N_0^2 (1 + \frac{am}{\omega} \cos(mz) \sin(kx - \omega t)). \tag{5.8}$$

Near the bed $\cos(mz) = 1$, and we can say the minimum value of $N^2 \approx N_0^2(1 - \frac{am}{\omega})$, where $am/\omega = st$ defined in equation (3.20). The local buoyancy frequency near the bed decreases with increasing steepness. The minimum buoyancy frequency written in terms of steepness is given by

$$min\{N^2\} = N_0^2(1 - st). \tag{5.9}$$

Near Bed Vertical Shear   Recall that the horizontal velocity associated with the wave has very little shear near the bed, i.e. $\partial u/\partial z \propto \sin(mz)$ (section sec:LwRi). The vertical shear near the bed is then determined by the velocity deficit created by the interaction of the oscillatory flow with the no slip condition at the bed. The velocity deficit approximation derived from the linearized horizontal momentum equation and neglecting the vertical derivative of pressure is given by

$$U_d = U_0 \sin(kx - \omega t + \delta^{-1}z) exp(-\delta^{-1}z). \tag{5.10}$$

The derivation can be found in appendix C. It then follows that the vertical shear of the horizontal velocity deficit induced by the interaction of the base flow with the no-slip boundary at the bed is given by

$$\frac{\partial U_d}{\partial z} = -\frac{U_0}{\delta} \exp(-\delta^{-1}z)(\sin(kx - \omega t + \delta^{-1}z) - \cos(kx - \omega t + \delta^{-1}z)), \quad (5.11)$$

and

$$\max\left\{\frac{\partial U}{\partial z}\right\} \propto \frac{U_0}{\delta}. \quad (5.12)$$

From equation (5.11), it can be seen that the maximum shear is phase shifted by $\phi_x(z) = -\delta^{-1}z$ from the maximum velocity. Note that the horizontal phase shift is a function of height. In figure 5.9, velocity profiles are plotted for various horizontal location. It can be seen that the vertical shear at the bed is larger at the $\pi/4$ phase shift then at the crest of the wave. At the $\pi/2$ phase shift there is a strong flow reversal that is a maximum of squared shear (i.e. there is an inflection point). Additionally it can be shown that, to leading order, the magnitude of the shear scales with $U_0/\delta = am/(k\delta)$. To see how the non dimensional parameters effect the shear magnitude, U_0/δ is rewritten in terms of the non dimensional parameters. Recall, from equation (3.23), $1/\delta = m\sqrt{Re/AR}$.

$$\frac{am}{k}\frac{1}{\delta} = \frac{A_\zeta m\omega}{k}\frac{1}{\delta} \quad (5.13)$$

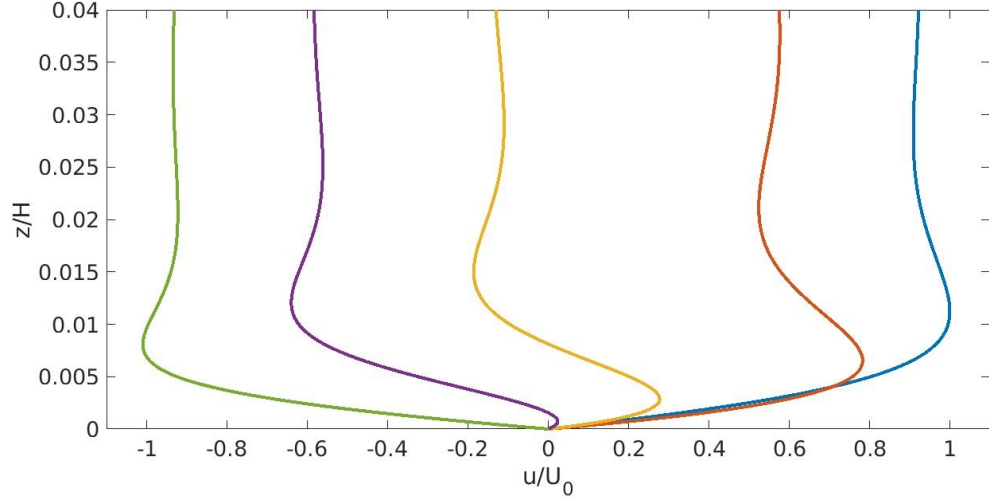$$= st \cdot C \cdot m\sqrt{\frac{Re}{AR}} \quad (5.14)$$

Figure 5.9: For the $AR8st4Re5$ case the profile of the horizontal velocity plotted for various locations phase shifted from the location of maximum velocity, $U_0 = U(x_0, z_0)$. From left to right the vertical velocity profiles are plotted at $\phi_x = \pi, 2\pi/3, \pi/2, \pi/4, 0$

Bulk Richardson number

The bulk Richardson number follows a similar and predictable trend to the minimum Richardson number computed in the flow field, therefore the bulk Richardson number defined here can be used to characterize the flow. The bulk Richardson number has the advantage that it can be computed using only bulk wave parameters, whereas the gradient Richardson number requires knowledge of the full flow field.

From the equation for the density perturbations from the method of vertical modes (3.6) and from the equation for the horizontal velocity deficit (5.10) (derivation can be found in appendix C) we can examine how changing the non dimensional parameters changes the structure of the isodensity surfaces and the magnitude of the vertical shear respectively. Note that the

equation for the density perturbations does not in anyway incorporate affects due to a no slip boundary and the equation for the horizontal velocity deficit is a boundary layer approximation that neglects the nonlinear terms. These equations are used simply to examine at the lowest order how changing the non dimensional parameters will affect the structure of the low Ri region. A Richardson number defined using the minimum value of the buoyancy frequency from equation (5.9) and U_0/δ, given in equation (5.13), to represent the characteristic shear can then be written as

$$
\begin{aligned}
Ri_a &= \frac{N_0^2(1 - st)}{(U_0/\delta)^2} \\
&= \frac{N_0^2(1 - st)}{(st \cdot C \cdot m\sqrt{Re/AR})^2} \\
&= \left(\frac{N_0}{C \cdot m}\right)^2 \frac{(1 - st)}{st^2} \frac{AR}{Re}
\end{aligned}
\tag{5.15}
$$

,

where Ri_a is an approximation for the minimum Richardson number within the flow. In the long wave limit,i.e. $k << m$, $C = N_0/m$ and becomes

$$
Ri_a \approx \frac{(1 - st)}{st^2} \frac{AR}{Re}.
\tag{5.16}
$$

The long wave limit is justified for waves with large AR. For an $AR = 8$, the approximation for the horizontal phase speed has an error of less than 3%. For this approximation an error of 3% is acceptable.

The bulk Richardson number, equation (5.16), is defined using only bulk wave parameters is plotted against the minimum Richardson number, Ri_m, computed in the wave field for each set of wave parameters in figure 5.10.

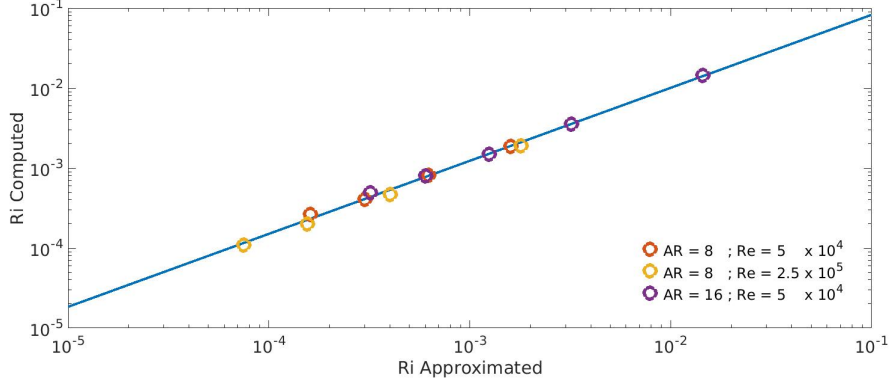The value of Ri_m and Ri_a are listed in table 5.2.

Figure 5.10: The BBL minimum Richardson number computed from the unperturbed wave field for each set of wave parameters plotted versus the corresponding approximated bulk Richardson number Ri_a defined using a BBL approximation. $Ri_m = Ri_a^{0.9126} \times 10^{-0.3957}$, and $R^2 = 0.999$.

Table 5.2: Richardson number approximation

Simulation	Re_λ	Ri_a	Ri_m
$AR8st2Re5$	7.76×10^4	1.60×10^{-3}	1.88×10^{-3}
$AR8st3Re5$	1.16×10^5	6.22×10^{-4}	8.16×10^{-4}
$AR8st4Re5$	1.55×10^5	3.00×10^{-4}	4.13×10^{-4}
$AR8st5Re5$	1.94×10^5	1.60×10^{-4}	2.67×10^{-4}
$AR8st2Re20$	1.55×10^5	1.80×10^{-3}	1.93×10^{-3}
$AR8st3Re20$	3.10×10^5	4.00×10^{-4}	4.71×10^{-4}
$AR8st4Re20$	4.66×10^5	1.56×10^{-4}	2.03×10^{-4}
$AR8st5Re20$	6.21×10^5	7.50×10^{-5}	1.09×10^{-5}
$AR16st1Re5$	7.94×10^4	1.44×10^{-2}	1.44×10^{-2}
$AR16st2Re5$	1.59×10^5	3.20×10^{-3}	3.54×10^{-3}
$AR16st3Re5$	2.38×10^5	1.20×10^{-3}	1.51×10^{-3}
$AR16st4Re5$	3.18×10^5	6.00×10^{-4}	8.11×10^{-4}
$AR16st5Re5$	3.97×10^5	3.20×10^{-4}	6.67×10^{-4}

5.2   Instability Structure and Evolution

After the insertion of the perturbation in the BBL, instabilities begin to grow in the region of low Ri ahead of the crest of the wave. This is consistent across all simulations that produce instabilities with some visible growth.The instabilities An example of an instability packet evolution is shown in figure 5.11, where successive snapshots of the Kelvin-Helmholtz-like instability for $AR16st5Re5$ is shown using the contour plot of the density field with the $Ri = 0.25$ contour plotted for reference. The location of the maximum perturbation energy, E_m, is marked in each snapshot and the initial perturbation amplitude was $A_0 = 10^{-4}$. The value of the initial perturbation amplitude was strong enough to lead to overturning as is evident at $t/T = 0.182$. To put the spatial scale of these instabilities in perspective, the vertical scale of figure 5.11 is the same as for figure 5.8, however the ratio of the horizontal scale is 1:8.

Instability Packets

The observed instability packets do appear to interact with one another as they overlap in space (figure 5.12). However, it is seen that the location of the maximum perturbation energy does not simply track a particular instability packet, instead it "jumps" (i.e. the location of the maximum perturbation energy does not track smoothly through space) from one packet to another predominantly in the direction of the large-scale mode-1 wave propagation. The packets appear to be overlapping because there are distinct peaks of the packets and certain packets begin to grow before others. The newly growing
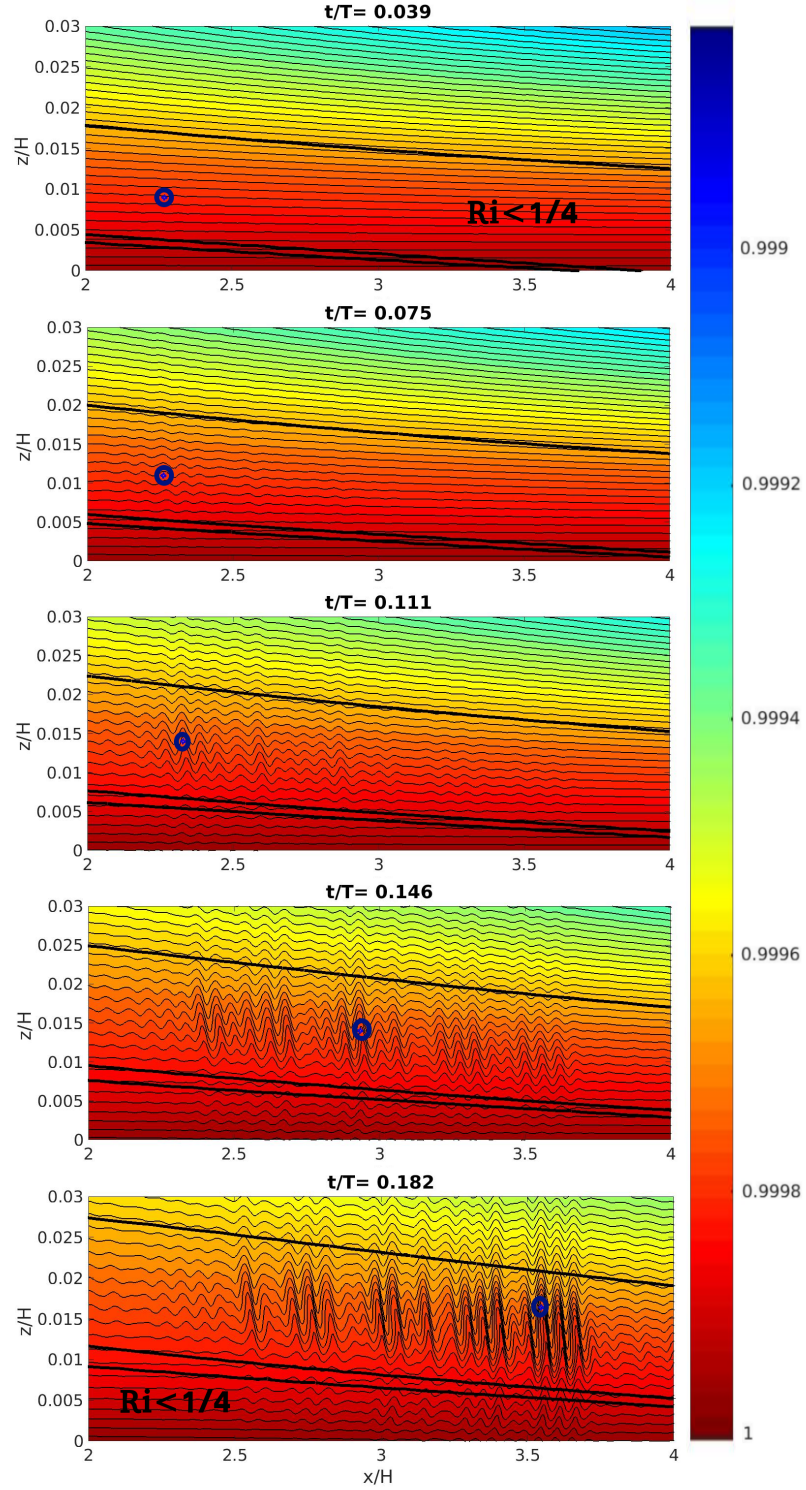
Figure 5.11: Successive snapshots of the Kelvin-Helmoholtz like instability that evolves in the BBL under a model mode 1 internal tide for $AR16st5Re5$ with $A_0 = 10^{-4}$. The blue dot in the figure marks the location where the perturbation energy is at a maximum in the domain, and the black line marks the contour $Ri = 0.25$ contour line.
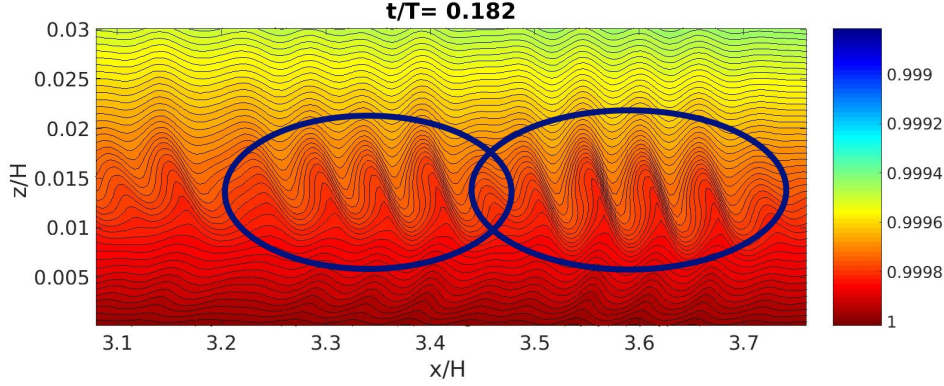
Figure 5.12: Snapshots of the Kelvin-Helmoholtz-like instability that develop in distinct wave packets for $AR16st5Re5$ with $A_0 = 10^{-4}$, a zoomed in frame from figure fig:insta. The blue circles indicate two overlapping wave packets.

wave packets begin to overlap with previously existing wave packets. The jumping indicates that the growth rate of the initially largest amplitude wave packet must have become less than the growth rate of the currently largest amplitude packet at some time $t < t_f$, where t_f is the time that the "jump" occurred.

In figure 5.13, the Hovmöller diagram of the contours of the perturbation energy is plotted. The vertical location of the Hovmöller diagram is chosen so that it cross through the center of the first overturning billow in the $AR16st5Re5$ simulation. The location of the maximum perturbation energy as a function of time for the given height, $z/H = 0.112$, is marked. It can be seen that the slope on the Hovmöller diagram of the "jumping" pattern follows the phase speed of the background wave. This slope is the general pattern that the jumping of the maximum perturbation energy within the flow follow on the time verse horizontal position diagram. The speed of the maximum perturbation energy within a wave packet (i.e. tracks the

wave packet) is much slower. Both the lines equal to the phase speed and to the maximum velocity, U_0, are plotted for reference in addition to the $Ri = \{0.1, 0.25\}$ contours.
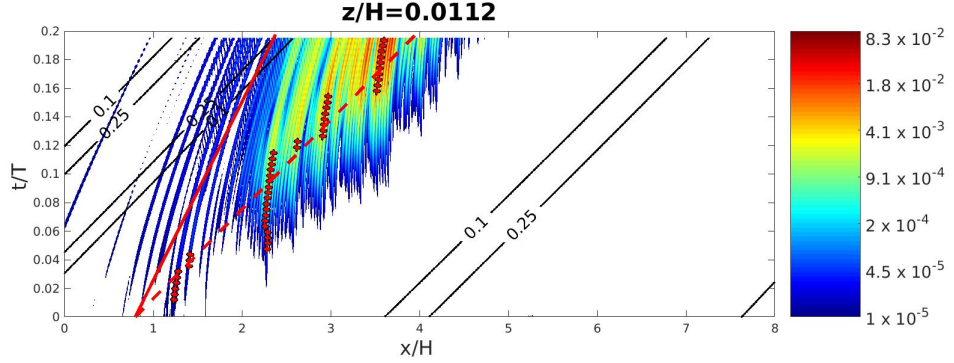

Figure 5.13: The Hovmöller diagram of the perturbation energy contour is plotted at $z/H = 0.0112$ for $AR16st5Re5$ with $A_0 = 10^{-4}$, the same simulation as in figure 5.11. The dashed red line is the line with slope $c = \omega/k$ and the solid line red line has slope $U_0 = st\omega/k$. The red circles indicate the maximum perturbation energy as a function of time at the given height. Note only half of the horizontal domain is shown.

From Miles-Howard semi-circle theorem for unstable normal mode instabilities of a homogeneous, inviscid, parallel shear flow, the instability phase speed, c, is required to be within the range of the background flow [89]. These are local instability arguments that can be used to give insight atleast locally, as to how the instability will evolve. That is, if the background velocity $U(z)$ is bounded by U_{min} and U_{max}, then any unstable normal mode must have a phase speed located within the semicircle centered at $c = (U_{max} + U_{min})/2$, $c_i = 0$ with a radius, $r = (U_{max} - U_{min})/2$[44] (refer to section 2.0.2). Therefore, a bound on the phase speed of the instability can be given as $|c| < U_0$. Wave that satisfy $U_0/C < 1$, where C is the phase speed of the background

wave, will then always have phase speed of the background wave that is larger then the phase speed of the instability. Therefore, the instabilities will always eventually be overcome by the background wave and will longer be in a region where the $Ri < 0.25$. Recall that

$$\frac{U_0}{c_0} = \frac{st\omega}{k}\frac{k}{\omega} = st, \tag{5.17}$$

it can then be seen that if the steepness parameter is less than one then the phase speed of the wave will always be greater then that of the shear instabilities. Therefore, when the steepness of a wave increases the amount of time that an instability can exist inside the region of low Ri also increases, in addition to the increased shear and isopycnal spreading.

Instability time scale, T_w

To obtain an approximate time that the instability is in the low Richardson number, we can start by using the approximation to the length of the low Richardson number region given in section 5.1.1 coupled with the phase speed of the background wave. The time that the instability is subject to low Richardson numbers is then given by

$$T_w = \frac{H \cdot L_w}{C} \tag{5.18}$$

This is the amount of time that an instability that is not moving (i.e. $c = 0$) and originated at the right most point of the low Richardson number region will be subject to Richardson numbers below $1/4$. Since the phase speed of

the instabilities is not zero, the time that the instability has to grow may be large than T_w. However, since the phase speed of the instabilities is typically small compared to the phase speed of the background wave it is assumed that T_w is a good approximation for the amount of time that the instability will have to grow.

5.2.1   Spatial Structure of Instability Packet

Figure 5.14 shows an exploded view of the isodensity contours at time $t/T = 0.182$ in the region where the Kelvin-Helmholtz-like instabilities have overturned. It is observed that the isodensity contours have overturned to the left in the direction of the shear at that height, which is consistent with the picture of the horizontal velocity profile in figure 5.15. Closer to the bed the isopycnal are tilting to the right, consistent with the picture that the sign of the vertical shear at the bed is pointing in the opposite direction.
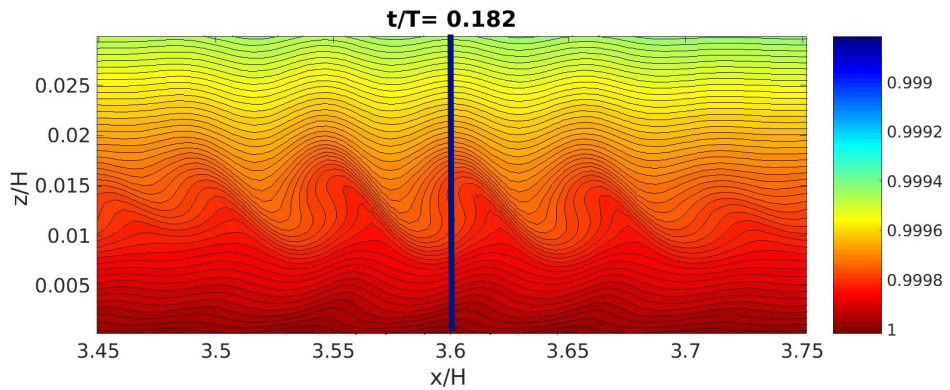

Figure 5.14: The isodensity contours are plotted for $AR16st5Re5$, $A_0 = 10^{-4}$. This snapshot corresponds to figure 5.11. The vertical line corresponds to the horizontal velocity profile in figure 5.15.
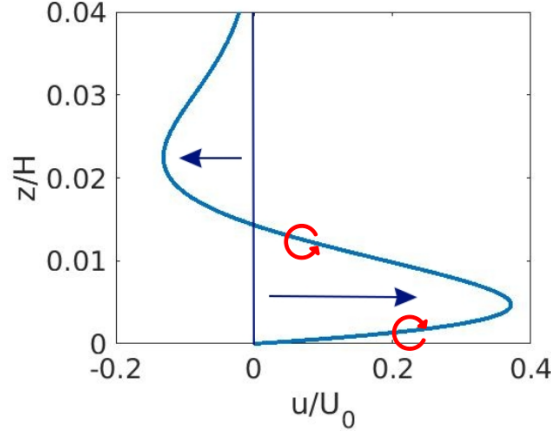
Figure 5.15: The unperturbed horizontal velocity profile is plotted at $x/H = 3.6$ for $AR16st5Re5$, at the time $t/T = 0.182$, corresponding to the vertical line in figure 5.14.

Spectra   The horizontal velocity spectra is plotted in figure 5.16 at various times to see how the changing background state affects the highest amplitude wavelength. It is noted that there is not strictly one mode that grows, instead there is a band of wave numbers with high growth rates. As time goes on not only does the amplitude of the spectral peak increase, so does the spectral width of the band, as it extends to higher and higher wave numbers. At the same time the peak of the band also shifts to higher wave numbers. Additionally it appears that resonant modes of the peak are also excited at later times. The peak of the horizontal velocity spectra $15 < H/\lambda < 20$, matches well to the wavelength of the Kelvin-Helmhotz-like instability in figure 5.14.
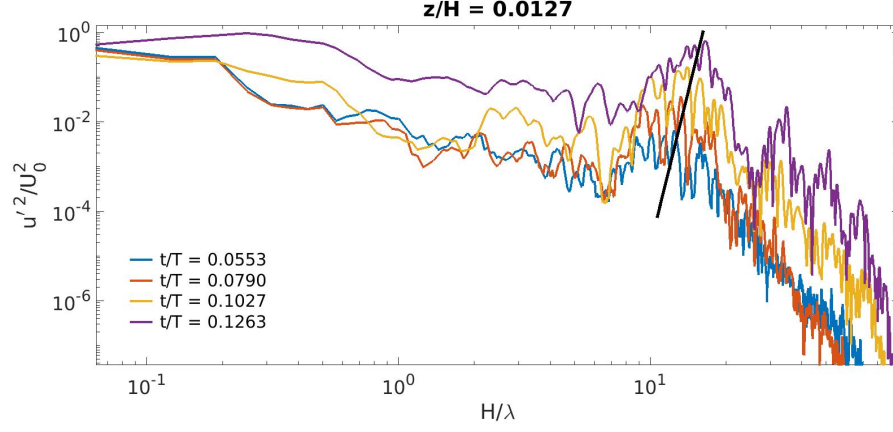
Figure 5.16: Spectra of the horizontal perturbations are plotted at various times for the $AR16st5Re5$ simulation. The black line is drawn in to indicate how the peak of the spectral amplitude shifts to higher wave numbers as time passes. At time $t/T = 0.1263$ resonant modes of the peak are excited.
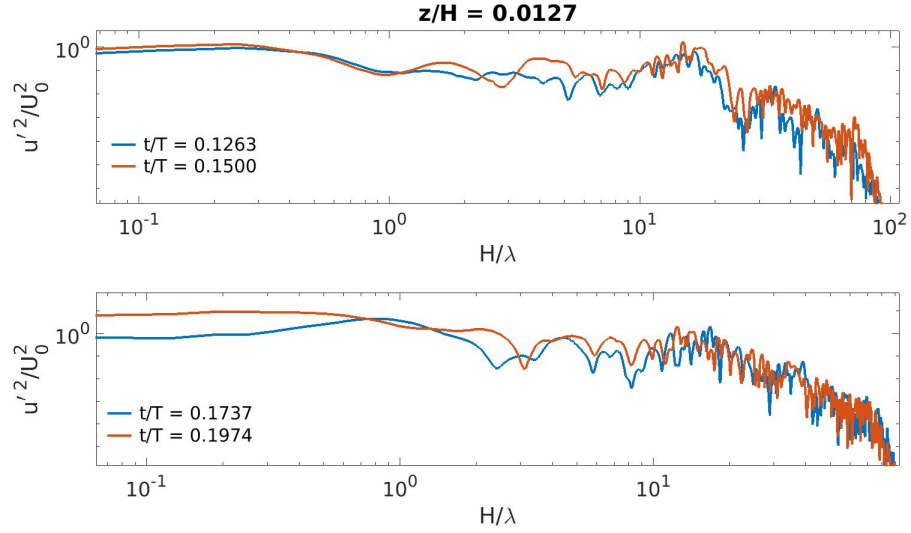

Figure 5.17: Spectra of the horizontal perturbations are plotted at later times then in figure 5.16 for the $AR16st5Re5$ simulation. At time $t/T = 0.1500$ most of the resonant modes become coalesced, by time $t/T = 0.1974$ all of the peaks have coalesced including the largest initial peak.

5.3 Linear Growth Rates

The perturbation energy growth rate is an important quantity to know, as it determines how fast the perturbation will grow during the time that the instability is in the region with low Ri. The growth rates will also allow for comparison with future theoretical analysis. Consequently, the growth rate will determine the absolute magnitude of the instability at the time, t_f, given an initial perturbation amplitude, E_0. The perturbation energy growth rate, σ, is defined as

$$E_p(t) = E_0 \exp\left(\sigma t\right) \tag{5.19}$$

where the growth rate and perturbation energy are both functions of time and space (i.e. $\sigma = \sigma(x, z, t)$). Since we are interested in the most unstable part of the wave field we can instead seek the growth rate of the largest amplitude perturbation energy. This is done by tracking the instability packet that has the largest perturbation energy within the time of the simulation. To calculate the growth rate of the instability wave packet, the linear growth phase just after the initial transient perturbation energy decay is computed. The exponential least squares fit to $E(t)$ is taken over a range that is most linear and which is just after the initial energy decay and before the non-linear phase. This choice is made to be most consistent across simulations.

The growth rates for a single set of parameters is calculated for varying levels of the initial perturbation amplitude, A_0. It is observed that the initial amplitude of the perturbation does not significantly affect the growth rate, at least in the initial linear growth phase. Therefore, the mean of the growth rates computed for varying amplitudes can be used to represent the growth

rate for a given set of wave parameters.

In figures 5.18, 5.19 ,5.20, 5.21 the maximum perturbation energy is plot-
ted as function of time for cases $AR8st4Re5$, $AR8st5Re5$, $AR16st4Re5$, and
$AR8st4Re20$ respectively. Note that the growth rate curves are normalized
by the period of the wave, T, and not the time, T_w, for which an instability
is subject to a $Ri < 1/4$. This was chosen since the relationship between
T_w and the period T is a simple linear relation, $T_w = T \cdot L_w/AR$ and this
scaling allows for a more direct comparison of the growth rate across steep-
ness parameters. The effect of T_w is taken into consideration in the next
section. In each of the perturbation energy time-series, there is only one
$E(t)$ curves. However, more values of, A_0, were tested. The values of A_0
shown here represent the lowest initial amplitude perturbation that resulted
in overturning.

]

Figure 5.18: The energy growth as a function of nondimensional time at low
Re for $AR = 8$, $st = 0.4$. The non-dimensional growth rate is found by fitting
a line to the linear region of the perturbation energy curve. The growth rate
$\sigma T = 48.74$.

Varying the steepness for the given set of parameters (i.e. $AR = 8$ and
$Re = 5 \times 10^4$), figure 5.18 and 5.19, it is observed that increasing the steepness
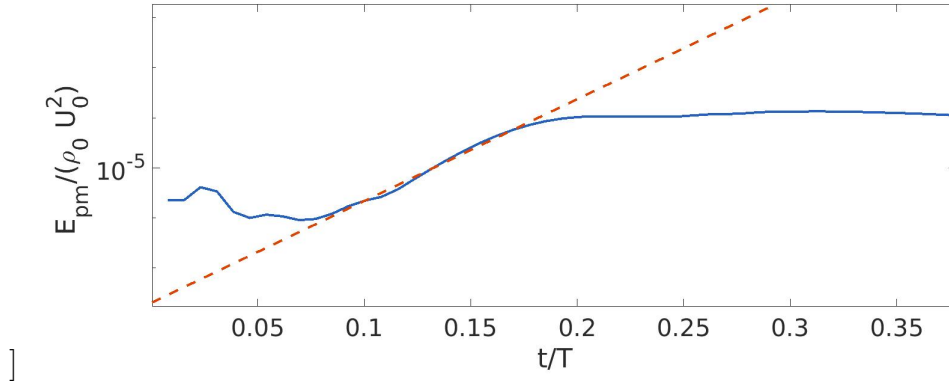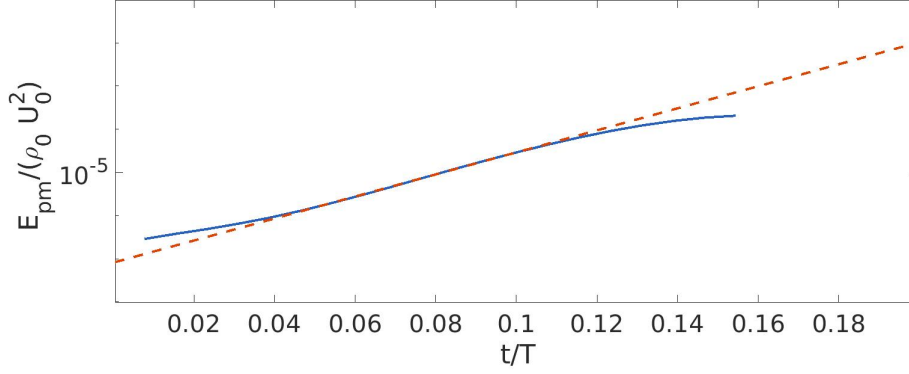
Figure 5.19: The energy growth as a function of nondimensional time at low Re for $AR = 8$, $st = 0.5$. The non-dimensional growth rate is found by fitting a line to the linear region of the perturbation energy curve. The growth rate $\sigma T = 61.04$.

results in an increase in the non-dimensional growth rate. Comparing figures 5.18 and 5.20, it is observed that for the same value of steepness and Reynolds number that the non-dimensional growth rate increases when you double the AR. Note that the period of the wave T increases when the AR increases. Therefore, the non dimensional growth rates normalized by T for $AR = 8$ and $AR = 16$ effects the non-dimensional growth rate. However this difference in the normalization is taken care of in the follow section where the period of the wave T is replaced by the time, T_w, that the instabilities are subject to low Richardson numbers.Lastly, when varying the Reynolds number while keeping the AR and st fixed by comparing figures 5.18 and 5.21. It can be seen that when increasing the Re the non-dimensional growth rate also increases.A summary of all of the parameter sets that were tested along with the corresponding growth rates are shown in table 5.3.
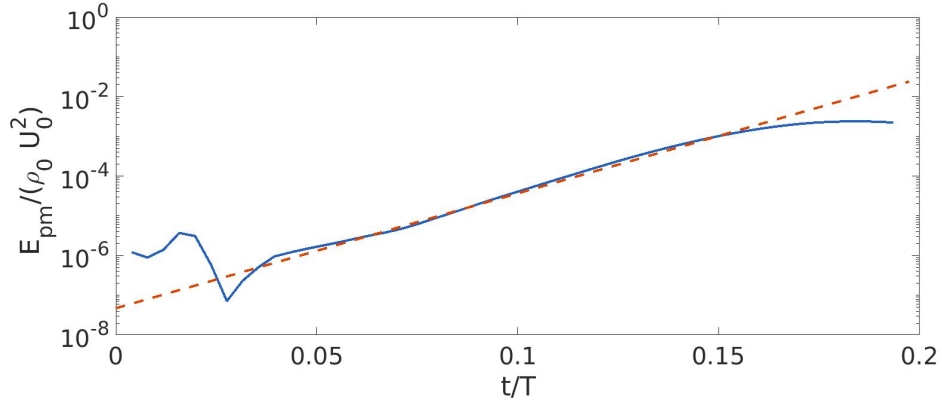
Figure 5.20: The energy growth as a function of nondimensional time at low Re for $AR = 16$, $st = 0.4$. The non-dimensional growth rate is found by fitting a line to the linear region of the perturbation energy curve. The growth rate $\sigma T = 61.04$.

Table 5.3: Growth Rates

Simulation	σT	σT_w	A_c
$AR8st2Re5$	8.93	2.97	No overturn
$AR8st3Re5$	19.45	8.00	No overturn
$AR8st4Re5$	48.74	22.43	4.4×10^{-6}
$AR8st5Re5$	61.04	30.20	1.1×10^{-7}
$AR8st1Re20$	1.50	0.44	No Overturn
$AR8st2Re20$	34.27	14.46	No Overturn
$AR8st3Re20$	52.12	25.10	6.5×10^{-8}
$AR8st4Re20$	123.56	63.94	5.85×10^{-10}
$AR16st1Re5$	6.54	1.23	No Overturn
$AR16st2Re5$	13.18	3.69	No Overturn
$AR16st3Re5$	45.72	16.46	2.6×10^{-3}
$AR16st4Re5$	66.12	27.13	1.1×10^{-5}
$AR16st5Re5$	95.16	42.93	5.5×10^{-8}

5.4   Stability Boundary

Similar to the discussion of instabilities in internal solitary waves dicussed by Barad & Fringer and progressive interfacial waves discussed by Troy & Koseff
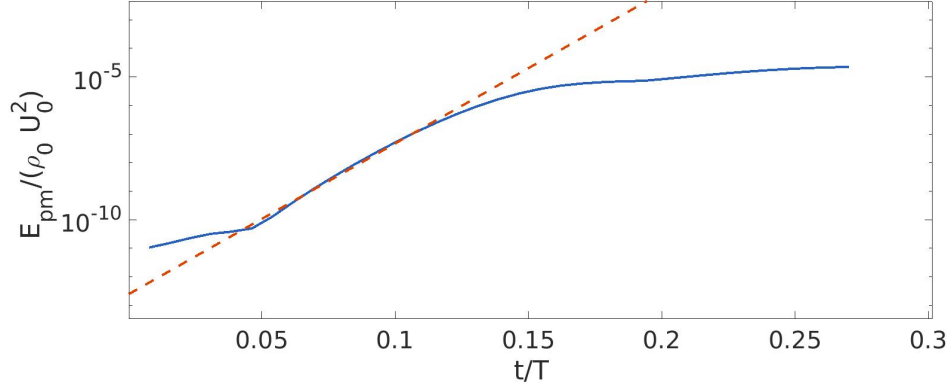
Figure 5.21: The energy growth as a function of nondimensional time at high Re for $AR = 8$, $st = 0.4$. The non-dimensional growth rate is found by fitting a line to the linear region of the perturbation energy curve. The growth rate $\sigma T = 123.56$.

in sections 1.3.1 and 1.3.1respectively, it is assumed that the non-dimensional growth rate is a function of the non-dimensional parameters that describe the problem,

$$\sigma T_w = F(AR, st, Re). \tag{5.20}$$

Since, the bulk Richardson number, given in equation (5.16), can be expressed in terms of the other three parameters and is linearly proportional to both the AR and Re, we can replace the st in the functional dependence with the Richardson number as

$$\sigma T_w = F(AR, Ri, Re). \tag{5.21}$$

A model to describe the growth rate as a function of the bulk wave parameters can be determine. In order to determine how the non-dimensional growth
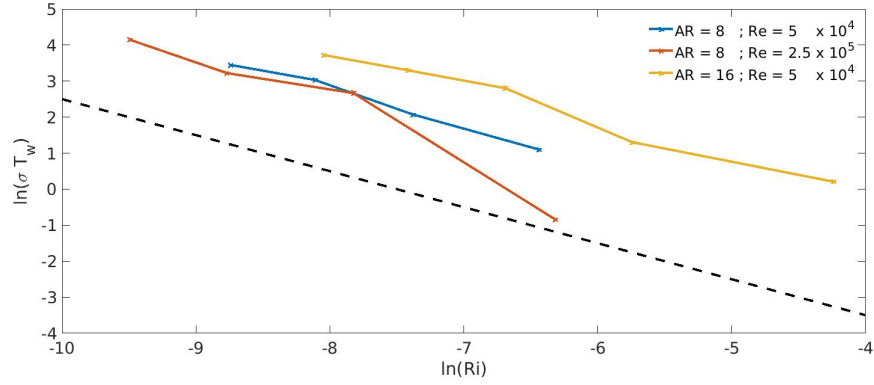
Figure 5.22: Non-dimensional perturbation growth rate as a function of the bulk Richardson number is plotted while keeping the Reynolds number and aspect ratios constant. The average of these slopes is used to find the exponent of the model. It is found that $\sigma T_w \propto Ri_a^{-1}$.

rate scales with respect to each non-dimensional parameter we model

$$
\sigma T_w \propto Ri^{n_0},
$$
$$
\sigma T_w \propto AR^{n_1}, \quad\quad (5.22)
$$
$$
\sigma T_w \propto Re^{n_2},
$$

where n_0, n_1 and n_2 are each constant scaling exponents over the range of parameters. This model is chosen since when the data is plotted on a log-log plot, the data lines up approximately linearly. The scaling exponents are then found by varying the parameter for which the exponent is to be found, while fixing the other parameters and observing how the growth rate is effected. It was found that

$$
\sigma T_w \propto Ri_a^{-1}, \quad\quad (5.23)
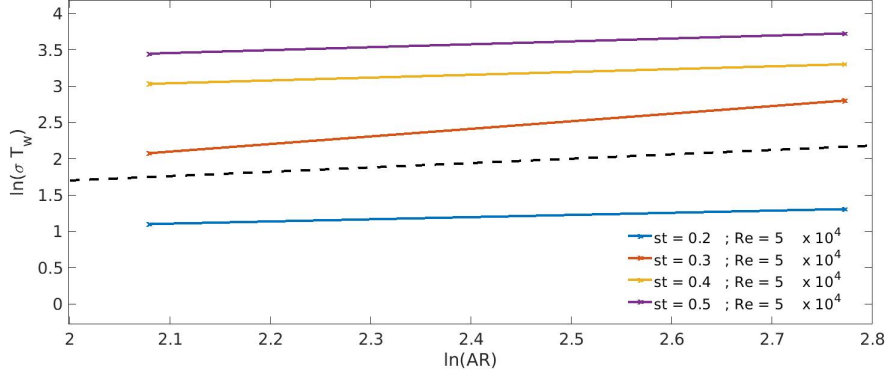$$

which can be seen in figure 5.22.

Figure 5.23: Non-dimensional perturbation growth rate as a function of the bulk aspect ratio is plotted while keeping the Reynolds number and the steepness constant. The average of these slopes is used to find the exponent of the model. It is found that $\sigma T_w \propto AR^{0.6}$.

When varying the AR (figure 5.23) while keeping the other parameters the same, it was found that

$$\sigma T_w \propto AR^{0.6}. \tag{5.24}$$

Similarly it was found that

$$\sigma T_w \propto Re^{0.92}, \tag{5.25}$$

as can be seen in figure 5.24. It then follows that to leading order

$$\sigma T_w \propto Ri_a^{-1} AR^{1.6} Re^{-0.08} = (1 - st)st^{-2} AR^{0.6} Re^{0.92}. \tag{5.26}$$

In figure 5.25 the non-dimensional growth rate is plotted as a function of the non-dimensional wave parameters as described in equation (5.26). The best fit line, with $R^2 = 0.9763$, is then plotted. The model for the data is given as
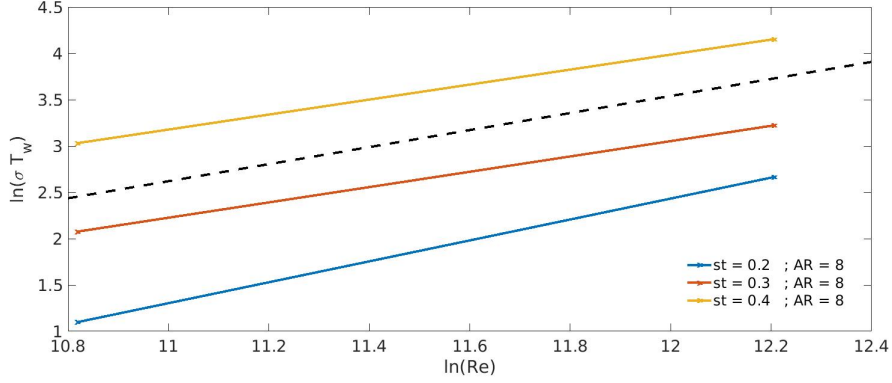
Figure 5.24: Non-dimensional perturbation growth rate as a function of the bulk Reynolds number is plotted while keeping the steepness and the aspect ratios constant. The average of these slopes is used to find the exponent of the model. It is found that $\sigma T_w \propto Re^{0.92}$. The horizontal black line marks the location where $\sigma T_w = 15$, all simulations that had growth rates above this value produced overturning for some value of A_0 while all simulations with growth rates below this value did not produce any overturing.

$\sigma T_w = 4.76 \cdot 10^{-4} \cdot Ri_a^{-1} AR^{1.6} Re^{-0.08} + 0.29$. The model written in terms of the steepness parameter is given as $\sigma T_w = 4.76 \cdot 10^{-4} \cdot (1 - st)st^{-2} AR^{0.6} Re^{0.92} + 0.29$.

Wave with non-dimensional growth rates less than $\sigma T_w = 15$ are shown to not exhibit isopycnal overturning for any value of A_0 tested. This indicates that these waves are stable. Above $\sigma T_w = 15$, instabilities are able to grow to a point where instability is possible for atleast some initial perturbation amplitude. Therefore, there exist a stability boundary at $\sigma T_w = 15$, this value is marked by a horizontal black line in figure 5.25. This result does not match the exact results of Troy & Koeseff[98] who studied long internal interfacial waves, and Fringer & Street[26] who studies moderate length internal interfacial waves,and Sadek[76] who studies the boundary layer instabilities under a long solitary wave.In each of these studies, it was shown that in order
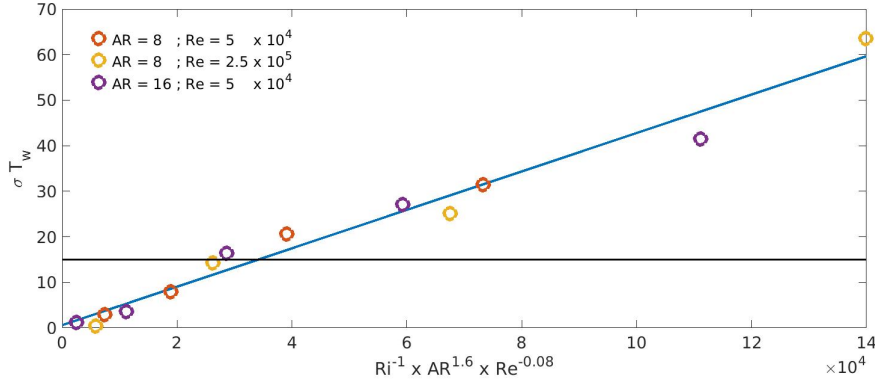
Figure 5.25: Non-dimensional perturbation growth rate as a function of the non-dimensional parameters of the wave, $\sigma T_w \propto Ri^{-1}AR^{1.6}Re^{-0.08}$, using the bulk Richardson number computed in the wave field. The model for the data is given as $\sigma T_w = 4.76 \cdot 10^{-4} \cdot Ri_a^{-1}AR^{1.6}Re^{-0.08} + 0.29$. The horizontal black line marks the location where $\sigma T_w = 15$, above this valye the simulations produced overturning while simulations with growth rates below this value did not.

for the unsteady shear flow under investigation to become unstable $\sigma T_w > 5$.

Chapter 6

Discussion

The results presented in this thesis are for an idealized model mode-1 internal wave propagating in a horizontal wave guide. In the ocean, however, this is never the case; there are always many additional complications such as sloping bottoms and roughness at the bed, in addition to abyssal hills and larger scale topography. There are also non-negligible background turbulence levels, higher mode waves, and background currents that may distort this picture. However, these results may be able to guide further research by indicating the wave phase where near-bottom instabilities are most likely to occur under a mode-1 wave. The bulk wave parameters can also be used to determine if there is potential for instability due to the interaction of the mode-1 internal wave with the bed. The Reynolds numbers in the ocean are typically larger than those computationally accessible. Therefore, low mode internal waves with lower steepness may be more prone to instability. Additionally, the aspect ratio of low mode internal waves in the ocean is also much larger than was tested here. For example, low mode internal wave with

aspect ratios larger than 30 are typically generated at the Aleutian ridge[16]. The larger aspect ratios are also more unstable since the amount of time that instabilities can develop near the bed in the along wave direction is extended. Therefore, in the open ocean, lower steepness internal wave may be more unstable due to higher Reynolds numbers and increased aspect ratios. When the low mode waves propagate into shallow seas the steepness level can be much higher, at the north east shelf edge of New Zealand, Sharples et. al [82] measured internal tides having mid-water column peak-to-trough amplitude typically 40 m, reaching as much as 70 m, almost 50% of the local water depth. Since, it has been shown that low mode internal waves have higher isopycnal displacements closer to the bed as the steepness is increased, these wave may have even higher steepness then were tested in this study.

In the past work on stability of internal solitary wave induced BBL, there are several key differences from the boundary layer of the mode-1 internal waves. That is the the internal solitary wave boundary layers, as discussed by Diamessis & Redekopp [19] creates a separation bubble that proceeds to destabilize. The instability is characterized by elevated levels of bottom shear stress and a periodic shedding of coherent vortex structures. This shedding process leaves a vortex wake behind the wave, in a wave following reference frame, where there is no interaction with the BBL of a trailing wave. Conversely, in the problem of the mode-1 wave BBL, any instability is constantly effected by the wave induced BBL. Additionally, there is no stratification at the bed to suppress instabilities that may be generated there so this type of wave BBL may be more susceptible to instability. The instabilities that develop in the boundary layer of a mode-1 internal wave have much different

characteristics. There is no creation of a separation bubble in the BBL of the mode-1 internal wave, the boundary layer may separate but does not re-attach. The instability triggered by finite amplitude perturbations generates instability packets that evolve into a train of billows that progressively moves away from the bed as they develop. The instability packets are continuously influenced by the background wave, changing both the phase speed of the instability as well as the growth rate. At some point the instability is suppressed by the existence of increased stratification due to compressed isodensity surfaces induced by the wave at the trough. The internal solitary wave has a two layer stratification, therefore the bottom boundary in unstratified and there is no stratification to suppress instabilities.

Since the mode-1 wave is periodic, residual perturbation energy left after a full wave period, may be larger than the initial perturbation which may then be able to lead to additional instability. Additionally, the picture may be changed if the simulations were continuously perturbed. Continuous perturbation of the boundary layer may actually be more realistic in the ocean where roughness elements are continuously affecting the flow. This continuous perturbation may additionally lower the threshold of the critical perturbation amplitude and potentially even modify the stability criterion.

Three dimensional simulations of this instability mechanism may additionally be able to further elucidate the correct parameterization of the low mode internal waves bottom drag. Here it has been shown that boundary shear instability is a probable mechanism for low mode internal wave dissipation in the ocean. Further studies to quantify the amount of dissipation caused by these instabilities and turbulence are required. Additionally, it has

been shown that there is a spatial intermittency of the instability and that the instabilities, at least in the two dimensional case, propagate away from the bed. Since it has been shown that the spatial distribution in vertical direction, as well as the horizontal, of the dissipation is important in the parameterization of the low mode energy dissipation in GCMs[61], further research is required to correctly parameterize distribution of the dissipation caused by the non-trivial evolution of this instability.

Internal wave packets are generated by the instabilities outside of the low Richardson number region where the instability packets can no longer grow. The low Richardson number region essentially acts as an instability wave-guide, a region in space where instabilities can grow and propagate. The instabilities are able to freely propagate in the low Ri region, however as the move into a region where Ri is above the critical value, $Ri > 0.25$, then instabilities cannot exist there and wave packets are generated and propagate away from the BBL.

Further investigation is required to examine that amount of energy that is radiated away from the boundary as high mode internal wave packets. These wave packets can then dissipate energy further away from the boundary. This energy radiation may also be important to parameterize in GCMs. Additionally, internal wave packets are generated even before overturning occurs so energy can be radiated away from the bottom and dissipated without overturning billows.

Shear stress at the bottom may be able to resuspend and lift sediment [91]. It was observed by Cheriton et. al. [15] that near-bed vertical velocities capable of lifting particulates high into the water column and that

once suspended, particulate matter was transported shoreward. Therefore it is also necessary to compute the shear stress that is generated at the bed. If the shear stress generated by the instabilities is strong enough to lead to resuspension, the internal tidal currents can then transport the suspended particulate. The instabilities observed in the study occur at the leading edge of the crest of the wave. The currents that suspended particulate would be exposed to would then be in the direction of the wave propagation. Therefore internal waves propagating towards the coast will carry particulate toward the coast. This can have significant impact on shelf development and ecological systems that may rely on nutrients supplied from the deep ocean.

Chapter 7

Conclusions

The structure of the bottom boundary layer under a model mode-1 internal wave in a horizontal wave guide is described. The non-dimensional parameters that fully characterize the wave are the steepness, aspect ratio, and the Reynolds number. It is shown that the region of maximum shear (i.e. inflection point of the vertical derivative of the horizontal velocity) is off set from the crest and troughs of the wave and that the horizontal phase shift of the maximum shear is a function of vertical position. Additionally, it is shown that the region of low Richardson number ahead of both the crest and trough have significantly different lengths. The length of these regions are defined as the length of the line that tracks the inflection point, of the in the vertical profiles of the horizontal velocity field, that is within a region where the Richardson number is below the critical vale of $Ri_{cr} = 0.25$. The difference in the length of the high shear region is attributed to the breaking of the asymmetry of the boundary layer by the difference in the vertical pressure gradient at the two location. The region of high shear ahead of the

crest of the wave is shown to be significantly longer than the region ahead of the trough. The difference in length is significant because the length of this high shear region is directly related to the amount of time that an instability will be in a region where the $Ri < 1/4$.

In addition to the longer region of high shear ahead of the crest, the crest of the wave also creates lifted and separated isopycnals. The spreading of the isopycnals essentially decreases the local stratification, reducing the stabilizing effect of that stratification locally. The reduced stratification and the high shear conspire to create a long region of low Ri that extends high into the water column. The region of low Ri acts as an instability wave-guide where the instabilities are able to grow and propagate.

It was found that the magnitude of the Richardson number in these regions was also significantly different. The magnitude of the Richardson number in the region ahead of the crest was much lower that the Richardson number in the region ahead of the trough. This was quantified using the normalization Richardson number defined in section 5.1.1. The magnitude of the growth rate is directly related to the magnitude of the Richardson number, therefore the region infront of the crest was much more prone to instability due to the lower value of Ri.

The instabilities exist as individual instability wave packets. As time passes the instability packet with the largest perturbation energy is not the same. The manner in which one instability packet begins to have higher perturbation energy then the previously highest perturbation energy packet is attributed to the fact that the background wave phase speed is larger than the phase speed of the packet. The difference in the phase speed of

the highest growth rate region compared to the phase speed of the wave causes the region a maximum perturbation energy to "jump" from one wave packet to another in the direction of the phase speed. The growth rate at the center of each wave packets is different due to to the spatially and temporally varying nature of the background flow.In order to calculate the growth rate of the instability packet that has the largest perturbation amplitude within the time of the simulation, that packet is tracked through time to calculate the time series of the perturbation energy at the center of that packet.

A bulk Richardson number for a model mode-1 internal wave propagating in a horizontal wave guide has been defined. It is shown that the bulk Richardson number can be written in terms of the three non-dimensional parameters that describe the flow; steepness, aspect ratio, and Reynolds number. The bulk Richardson number is then used to collapse the non-dimensional growth rates of all of the simulations. It is thus shown that the non-dimensional growth rate can be written as a function of the non-dimensional wave parameters. The stability boundary is shown to exist at $\sigma T_w = 15$, below this value no overturning is observed regardless of the initial perturbation amplitude. Where σ is the growth rate of the instability and T_w is the time that the instability is subject to Richardson numbers below the 1/4. Above the stability boundary it is shown that there exists some critical perturbation amplitude that causes overturning in the boundary layer, while below this level there is no initial perturbation that causes overturning.

7.1   Future Work

The mode-1 internal wave BBL has been studied over a range of the non-dimensional parameters. However, it would be instructive to test additionally values of the parameters in order to see if the model for the non-dimensional growth rate hold. Additionally, it would be beneficial to see if the value of the critical non-dimensional growth rate also holds over a larger range of wave parameters.

The windowing function used in order to focus the initial perturbation near the bed is Gaussian in the vertical. Different windowing functions for the initial noise field should be tested in order to see if the windowing function affects the results. Initial tests have shown that the structure of the windowing function does not qualitatively affect the structure of the instabilities that develop. However, the shape of the windowing function may change the amplitude of the initial perturbation that is subject to the largest growth rates in the flow.

Wave packets are observed to radiate away from the bed. The energy that is radiate away as high mode wave packets may be capable of transporting a non negligible amount of perturbation energy high into the water column where it will eventually be dissipated. Since the vertical distribution of dissipation is important for GCMs, it may be important to quantify the amount of energy transported away as wave packets.

Lastly, we will allow the instabilities to evolve in three dimensions. In a two dimension simulation, the instabilities are confined, however when allowed to develop in three dimensions, additional instability modes may

cause the billows that develop to break down to turbulence. This may change how the billows evolve as they propagate upwards away from the bed.

Appendix A

Theory: Method of Vertical Modes

Waves in the ocean are naturally confined in the vertical by its' boundaries, the sea floor acts as an impermeable no slip boundary and the oceans surface is a deform able free slip boundary. These boundaries can be thought of as a wave-guide, restricting the wave motions in the vertical, causing the internal waves to have the characteristic of a standing wave in the vertical and propagating in the horizontal. If we approximate the sea surface as a free- slip rigid lid and the sea floor as a free-slip flat plate then we can us the method of vertical modes. The method of vertical modes requires the vertical boundaries to be horizontal, to find internal wave solutions to the Navier-Stokes equations. From the Navier-Stokes equations we can derive a single equation with one unknown, which is shown in Gerekema's notes [37].

$$\frac{\partial^2}{\partial t^2}\nabla^2 w + (\overrightarrow{f}\cdot\nabla)^2 w + N^2\nabla_h w = 0 \qquad\qquad \text{(A.1)}$$

Where $\overrightarrow{f} = (0, \overline{f}, f)$ is the Coriolis parameter which we assume to be zero in this study. This assumption renders the horizontal plane isotropic, in the sense that the direction of wave propagation becomes immaterial and their is no Coriolis force on the wave. We then seek solutions of the form

$$w = W(z)exp\{i(kx - \omega t)\} \tag{A.2}$$

We take ω to be positive and substitute our solution into equation (A.1), resulting in an ordinary differential equation for W.

$$W'' + k^2 \frac{N^2(z) - \omega^2}{\omega^2} W = 0 \tag{A.3}$$

Since k in the equation appears only as a squared quantity, solutions can exist with either a positive or negative k indicating a leftward or rightward propagating wave respectively. Without losing generality, we can than assume k to be a positive quantity. The boundary conditions we consider as described previously are a rigid lid and a horizontal bottom boundary which can be expressed mathematically as follows:

$$W = 0 \qquad\qquad \text{at } z = 0, H \tag{A.4}$$

Where $z = 0$ and $z = H$ are the bottom and top boundaries respectively. Equation (A.3) together with the boundary conditions form a Sturm-Liouville problem, which for a fixed frequency ω, has an infinite number of solutions W_n, which are the eigenfunctions or vertical modes, with corresponding eigenvalues k_n. From the solutions W_n it is then possible to find

the solutions for the horizontal velocity and density perturbation field given an initial arbitrary stratification. For a two dimensional field we can simply solve for the horizontal velocity field using the continuity equation and the density field through the density equation.

The general solution of w consists of the superposition

$$w = \sum_n W_n(z)[a_n^{\pm} exp[i(k_n^{\pm}x - \omega t)]], \tag{A.5}$$

where a_n is an arbitrary complex constant. The dispersion relation for these waves can be expressed as

$$m^2(z) = k^2 \frac{N^2(z) - \omega^2}{\omega^2 - f^2}. \tag{A.6}$$

Solutions can exhibit two types of behavior depending on the sign of m^2. Oscillatory in those parts of the water column where m is real, i.e. $m^2(z) \geq 0$ and exponential-like decay when, $m^2(z) < 0$, where the wave amplitude decreases rapidly outside of the wave-guide. It then follows that for internal waves of a give frequency to exist, one of the inequalities in equation (A.7) must be satisfied inside the wave-guide and will decay exponentially outside of this region.

$$N(z) \leq \omega \leq |f| \qquad \text{or} \qquad |f| \leq \omega \leq N(z) \tag{A.7}$$

Since internal tides are generated at frequencies identical to those of the barotropic tides ($M_2, S_2, O_1, K_1, etc.$), internal tides of diurnal frequency can only propagate freely equatorward of about ± 30 deg latitude, but semidiurnal

tides can propagate freely throughout most of the ocean, as $\omega_{M_2} = \|f\|$ at $\pm 74.5\,\mathrm{deg}$ latitude [90] and ω is typically much less than N^2.

For low mode internal tides which inherently have low-frequencies, the hydrostatic approximation is often appropriate, meaning that the vertical acceleration of $\partial w/\partial t$ can be neglected. This amounts to assuming that $N >> \omega$, meaning that we can rewrite the Sturm-Liouville problem equation (A.3) as

$$W'' + \bar{k}^2 N^2(z)W = 0 \qquad (A.8)$$

with $\bar{k} = k/(\omega^2 - f^2)^{1/2}$. The hydrostatic approximation thus brings about a considerable simplification, that the vertical structure of the modes W_n no longer depends on the wave frequency ω. Making an additional simplification, that the stratification is uniform i.e. $N = constant$. Now in order to solve for our wave field we must resolve the eigenvalues k_n and the vertical structure of the modes W_n. we can now write equation (A.3) as

$$W'' + m^2 W = 0, \qquad (A.9)$$

where m, defined in the dispersion relation is now independent of z and real since we are looking for wave-like solutions. The general solutions can then we written as

$$W = C_1 \sin mz + C_2 \cos mz \qquad (A.10)$$

applying the boundary conditions it can be shown that $C_1 = a_n$ is an arbi-

trary constant, $C_2 = 0$, and $\sin mz = 0$. The solution is then given by

$$m_n = \pm\frac{n\pi}{H} \qquad\qquad \text{for } n = 1, 2, 3, ...$$

From the dispersion relation, we can then write the eigenvalues as

$$k_n = m_n(\frac{\omega^2 - f^2}{N^2 - \omega^2})^{1/2} \qquad\qquad \text{for } n = 1, 2, 3, ...$$

For a given frequency ω, there are then an infinite number of eigenvalues k_n, which are the horizontal wave numbers. Thus, if we set the wave number k and mode number n as the independent variables we can rewrite the dispersion relation to express the frequency as a function of known and independent variables.

$$\omega^2 = \frac{N^2 k^2 + f^2 m^2}{k^2 + m^2} \tag{A.11}$$

The horizontal group velocity can then be found by differentiating, $c_g = d\omega/dk$,

$$c_g = \pm\frac{1}{m}\frac{(\omega^2 - f^2)^{1/2}(N^2 - \omega^2)^{3/2}}{\omega(N^2 - f^2)}. \tag{A.12}$$

If k is positive we have a rightward propagating wave and when k is negative there is a leftward propagating wave. The group velocity c_g indicates how fast the wave energy travels and the phase horizontal phase speed c, how fast the wave's crests and troughs travel, where $c = \omega/k$. If $f = 0$ as in this experiment, long waves become dispersionless, having a group and phase speed $c_0 = N/m$. Finally writing down the wave field for an arbitrary

number of modes

$$U_n = -\sum_n a_n \frac{m_n}{k_n} \cos{(m_n z)} \sin{(k_n x - \omega_n t)},$$

$$W_n = \sum_n a_n \sin{(m_n z)} \cos{(k_n x - \omega_n t)},$$

$$\rho'_n = -\sum_n \frac{a_n}{\omega_n} N_0^2 \frac{\rho_0}{g} \sin{(m_n z)} \sin{(k_n x - \omega_n t)},$$

$$P_n = -\sum_n \rho_0 a_n \omega_n \frac{m_n}{k_n^2} \cos{(m_n z)} \sin{(k_n x - \omega_n t)}.$$

Finally, it is important to consider how the isopycnals are displaced by the wave. By letting the isopycnals that lie at depth z_0 at a state of rest be described by

$$z = z_0 + \zeta(x, z_0, t). \tag{A.13}$$

Then

$$w(x, z, t) = \frac{\partial \zeta}{\partial t}(x, z_0, t) + u(x, z, t)\frac{\partial \zeta}{\partial t}. \tag{A.14}$$

Making a Taylor expansion about $z = z_0$ and neglecting the nonlinear terms gives

$$w(x, z_0, t) = \frac{\partial \zeta}{\partial t}(x, z_0, t). \tag{A.15}$$

Therefore the solution for ζ is

$$\zeta(x, z, t) = -\sum_n \frac{a_n}{\omega_n} sin(m(z - \zeta)) sin(k_n x - \omega t). \tag{A.16}$$

Appendix B

Isopycnal Slope

In addition to the steepness parameter, defined simply using the bulk wave parameters, the directly related quantity of isopycnal slope can also be examined. The isopycnal slope is computed by differentiating equation (3.12), with respect to the horizontal,

$$\frac{\partial \zeta}{\partial x} = -A_\zeta k \sin\left(m(z-\zeta)\right) \cos\left(kx - \omega t\right) - A_\zeta m \frac{\partial \zeta}{\partial x} \cos\left(m(z-\zeta)\right) \sin\left(kx - \omega t\right),$$

(B.1)

substituting for compactness

$$u = m(z-\zeta),$$
$$v = kx - \omega t,$$

(B.2)

and solving for the slope, the partial differential equation (B.1) becomes

$$\frac{\partial \zeta}{\partial x} = -\frac{A_\zeta k \cos v \sin u}{1 + A_\zeta m \sin v \cos u}.$$

(B.3)

The maximum wave slope, $\alpha = max[\partial\zeta/\partial x]$, can then be found by computing the gradient of the wave slope in equation (B.3) and setting it to zero. Although, it is a non-trivial task to compute the gradient of this function there are a few things that can be learned about the location and magnitude of the maximum slope.

The maximum slope will occur if $A_\zeta m = 1$; this will cause the denominator to be zero at a point meaning that there is an infinite slope (i.e. a region of static instability). It can also be seen that if $A_\zeta m$ is small the numerator will dictate the magnitude of the maximum slope, $\alpha \approx A_\zeta k$, and will be located at approximately mid depth, $x = H/2$.

For the range of steepness that are of interest, $0.1 \leq st \leq 0.5$, the maximum slope is a balance between minimizing the denominator and maximizing the numerator. If we rewrite the slope of the wave as

$$\frac{\partial\zeta}{\partial x} = -\frac{st2/AR\cos v\sin u}{1 + st\sin v\cos u}, \qquad (B.4)$$

it can be seen that for small aspect ratios the numerator is dominant, whereas for large steepness level the denominator becomes more important. Looking at the vertical location of the maximum slope it can be seen that increasing the value of the steepness parameter causes the location of the maximum slope to approach the boundaries. Since the local isopycnal slope directly relates to the local buoyancy frequency it can be seen that as the steepness is increased the local buoyancy frequency near the bed is decreased, essentially reducing the local Richardson number near the bed. The decreased stratification near the bed coupled with high shear created by the boundary layer

structure is a likely indicator for the potential of instability.

In order to examine more quantitatively how the magnitude and structure of this function change with wave parameters we will choose a horizontal location to examine. For simplicity, let us choose a horizontal location, $xk = 3\pi/4$. This location is chosen because it is the region of maximum wall shear stress found from the linear boundary layer approximation for oscillatory laminar boundary layers[11].The equation for the isopycnal slope at the given horizontal location is then given by,

$$g = -\frac{\sqrt{2}stAR\sin u}{1 + \frac{\sqrt{2}}{2}st\cos u}. \tag{B.5}$$

Differentiating g with respect to z and setting it equal zero to find the maximum slope at the given horizontal location:

$$\frac{\partial g}{\partial z} = -stk\cos(mz) + 1/2st^2k\cos^2(mz) + 1/2st^2k\sin^2(mz), \tag{B.6}$$

simplifying the equation, it becomes

$$0 = -\cos(mz) + 1/2st. \tag{B.7}$$

From this it it can be seen that as the steepness is increased the location of the maximum slope is pushed towards the bed. The vertical location of the maximum slope is at $z = 1/m\cos^{-1}(1/2st)$.

Appendix C

Boundary Layer Approximation

The bottom boundary layer under a mode 1 wave propagating in a horizontal wave guide has the interesting characteristic that regions of maximum shear do not correspond to the crests and troughs of the wave (i.e. regions of maximum velocity). This is similar to the oscillatory boundary layers, which do not have horizontal dependence [48][65] [11], with a free stream velocity that is sinusoidal in time. It is observed that the maximum velocity lags 45° behind the max wall shear stress and to the oscillatory boundary layer that is sinusoidal in space and time [96]. To show why this occurs, the laminar boundary layer approximation can be found for the mode-1 wave.

The boundary layer approximation for a mode-1 wave propagating in a horizontal wave guide is derived using the linearized momentum equations and the continuity equation.Recall the mode-1 internal wave solution for a wave propagating in a horizontal wave guide is given in equation (C.1). In this derivation the full velocity field will be denoted using $\mathbf{U} = (U, W)$, which is assumed to be composed of the background velocity field $\mathbf{u} = (u, w)$ and

a velocity deficit, $\mathbf{U_d} = (U_d, W_d)$, which is induced by the nonslip boundary condition at the bed. The boundary layer approximation applied here assumes that the density perturbation near the bed, i.e. $z < 5\delta$, is negligible. Therefore when solving for $\mathbf{U_d}$, the density equation is not considered and the force of gravity is neglected.

$$u(x, z, t) = -\frac{am}{k} \cos{(mz)} \sin{(kx - \omega t)}$$

$$w(x, z, t) = a \sin{(mz)} \cos{(kx - \omega t)} \tag{C.1}$$

$$\rho'(x, z, t) = -\frac{a}{\omega} N_0^2 \frac{\rho_0}{g} \sin{(mz)} \sin{(kx - \omega t)}$$

The equations of motion are

$$\frac{\partial \mathbf{U}}{\partial t} = -\frac{1}{\rho_0} \nabla p + \nu \nabla^2 \mathbf{U}, \tag{C.2}$$

$$\nabla \cdot \mathbf{U} = 0, \tag{C.3}$$

where p is the pressure, ν is the viscosity, and ρ_0 is the reference density. The horizontal momentum equation is then given as

$$\frac{\partial U}{\partial t} = -\frac{1}{\rho_0} \frac{\partial p}{\partial x} + \nu \frac{\partial^2 U}{\partial z^2} + \nu \frac{\partial^2 U}{\partial x^2}. \tag{C.4}$$

The term $\nu \frac{\partial^2 U}{\partial x^2}$ is $O(\nu k^2 U)$ which is small compared to the other terms and can therefor be neglected. Additionally, far away from the boundary the velocity deficit goes to zero and the viscous terms become negligible and the

equation becomes

$$\frac{\partial u}{\partial t} = -\frac{1}{\rho_0}\frac{\partial p}{\partial x}.$$
(C.5)

The pressure term can then be eliminated in equation (C.4)

$$\frac{\partial U}{\partial t} = \frac{\partial u}{\partial t} + \nu\frac{\partial^2 U}{\partial z^2},$$
(C.6)

equivalently

$$\frac{\partial}{\partial t}(U - u) = \nu\frac{\partial^2}{\partial z^2}(u - U_d).$$
(C.7)

Since the viscous term is negligible for the wave component u, the equation can then be simplified to an equation in only the velocity deficit,

$$\frac{\partial U_d}{\partial t} = \nu\frac{\partial^2 U_d}{\partial z^2}.$$
(C.8)

The boundary conditions are

$$U_d = \begin{cases} -u = -U_0\cos(mz)\sin(kx - \omega t) & \text{for } z = 0 \\ 0 & \text{for } z \to \infty \end{cases},$$

where $U_0 = -am/k$. Conversely the boundary conditions can be written in terms of U as

$$U = \begin{cases} 0 & \text{for } z = 0 \\ u = U_0\cos(mz)\sin(kx - \omega t) & \text{for } z \to \infty \end{cases}.$$

The solution to the partial differential equation is then

$$U_d = -U_0 \exp\left(-\delta^{-1}z\right) \sin\left(kx - \omega t - \delta^{-1}z\right). \tag{C.9}$$

Where δ is the stokes boundary layer thickness

$$\delta = \sqrt{\frac{2\nu}{\omega}}. \tag{C.10}$$

The horizontal velocity field, U, is then written as

$$U = U_0[\cos\left(mz\right)\sin\left(kx - \omega t\right) - \exp\left(-\delta^{-1}z\right)\sin\left(kx - \omega t - \delta^{-1}z\right)]. \tag{C.11}$$

From the continuity equation, the vertical velocity deficit can then be obtained,

$$\frac{\partial U_d}{\partial x} - \frac{\partial W_d}{\partial z} = 0. \tag{C.12}$$

The vertical velocity deficit is then given by

$$W_d = U_0 k \frac{\delta}{2} \exp\left(-\delta^{-1}z\right)\left(\sin\left(kx - \omega t - \delta^{-1}z\right) - \cos\left(kx - \omega t - \delta^{-1}z\right)\right), \tag{C.13}$$

and the total vertical velocity is

$$W = a[\sin\left(mz\right)\cos\left(kx - \omega t\right) +$$
$$\frac{m\delta}{2}\exp\left(-\delta^{-1}z\right)\left(\sin\left(kx - \omega t - \delta^{-1}z\right) - \cos\left(kx - \omega t - \delta^{-1}z\right)\right)]. \tag{C.14}$$
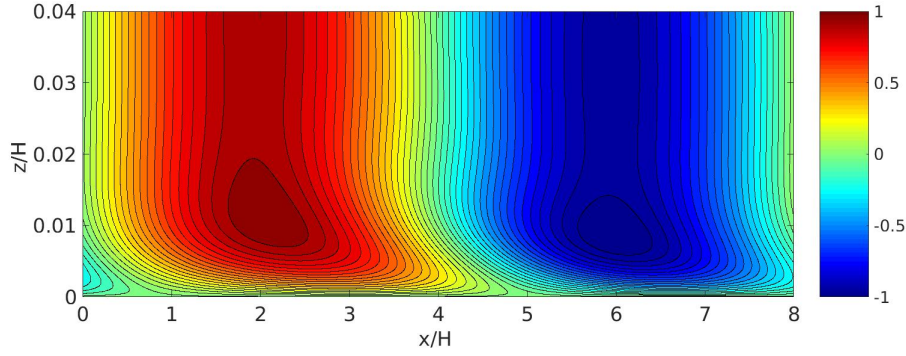
Figure C.1: An example of the BBL structure using the horizontal velocity field from the simulation for $AR = 8$, $st = 0.3$, $Re = 5 \times 10^4$
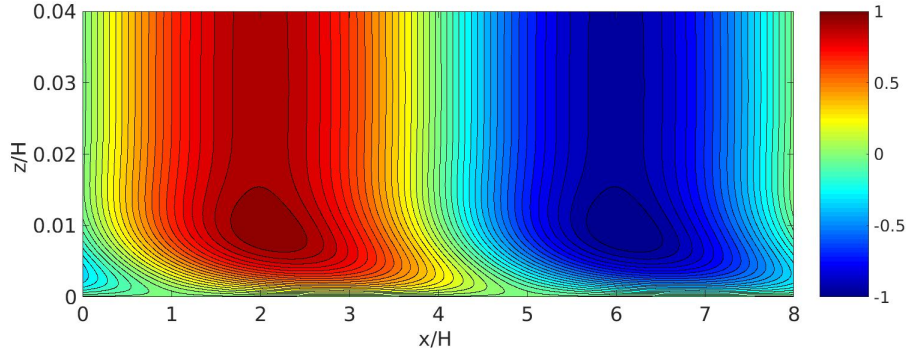

Figure C.2: An example of the flow field using the approximate velocity deficit to find the structure of the BBL for an $AR = 8$, $st = 0.3$, $Re = 5 \times 10^4$

This is a simple approximation that neglects the non-linear terms as well as the effect of the density perturbations, and therefore does not fully capture all of the aspects of the true boundary layer that develops in the two dimensional fully non-linear non-hydrostatic problem.However, it does give a pretty accurate approximation that gives insight as to how the boundary layer develops this particular structure. Particularly that the maximum shear is phase shifted from the maximum velocity. In order to compare qual-

itatively how well the boundary layer approximation approximates the BBL under the mode-1 internal wave, both the velocity and shear are plotted for both the approximation and the true simulated boundary layer in figures .
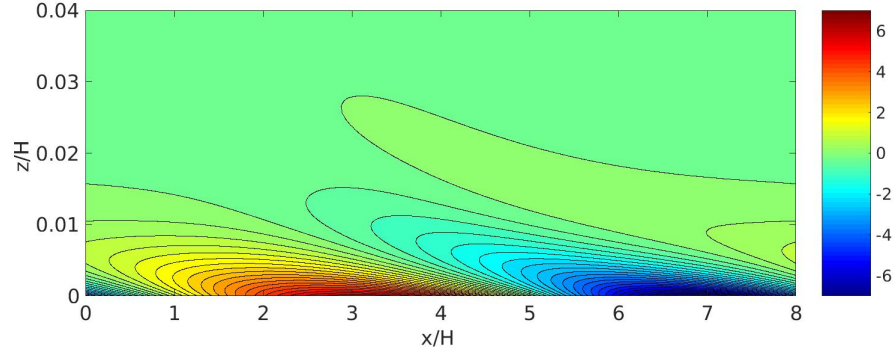

Figure C.3: An example of the BBL structure using the vertical derivative of the horizontal velocity field from the simulation for $AR = 8$, $st = 0.3$, $Re = 5 \times 10^4$
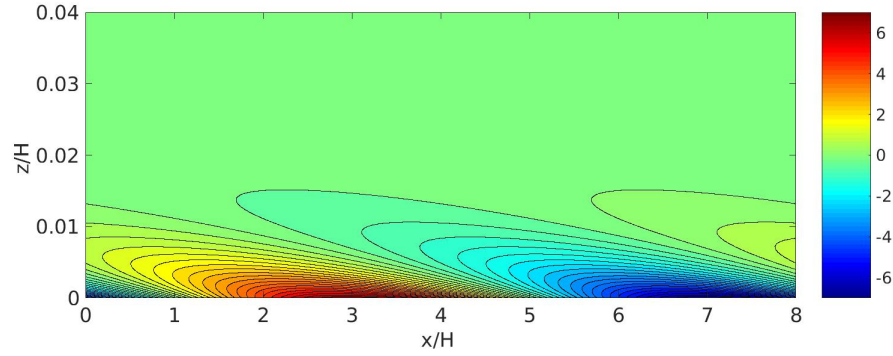

Figure C.4: An example of the flow field using the vertical derivative of the horizontal velocity from the approximate velocity field for an $AR = 8$, $st = 0.3$, $Re = 5 \times 10^4$

Appendix D

Noise Generation

The noise is generated by building a random noise field over a uniform grid in both direction. Then the two-dimensional Fourier transform of the field is scaled by k^{-1}. Then inverse Fourier transform of the field is then taken and a Gaussian window is used in the vertical so that the noise is focused near the bed. The Gaussian window is given by

$$g(z) = A \times exp[-\frac{(z - 2\delta)^2}{\frac{1}{2}\delta^2}], \qquad (D.1)$$

where δ is the boundary layer thickness of oscillatory flow defined as

$$\delta = 2\pi\sqrt{\frac{2\nu}{\omega}}. \qquad (D.2)$$

This window is chosen so that the maximum perturbation is at the height of the boundary layer and that it goes to zero at the boundaries. This allows for the perturbation to be compatible with the boundary conditions as well as be focused in the high shear regions where instabilities are likely while minimally

affecting the rest of the background flow. Once the noise is windowed near the bed, the noise is projected onto a divergence free basis. This makes the noise divergence free so that the noise is compatible with the method.

Bibliography

[1] J.K. Ansong, B.K. Arbic, M.C. Buijsman, J.G. Richman, J.F. Shriver, and A.J. Wallcraft. Indirect evidence for substantial damping of low-mode internal tides in the open ocean. *J. Geophys. Res. Oceans*, 120: 6057–6071, 2015. doi: 10.1002/2015JC010998.

[2] N.J. Balmforth and T. Peacock. Tidal conversion by supercritical topography. *J. Phys. Oceanogr.*, 39:1965–1974, 2009. doi: 10.1175/2009JPO4057.1.

[3] M.F. Barad and O.B. Fringer. Simulations of shear instabilities in interfacial gravity waves. *J. Fluid Mech.*, 644:61–95, 2010. doi: 10.1017/S0022112009992035.

[4] G.K. Batchelor. An introduction to fluid dynamics. *Cambridge University Press.*, 1967.

[5] D. Bogucki and C. Garrett. A simple-model for the shear-induced decay of an internal solitary wave. *J. Phys. Oceanogr.*, 23:1767–1776, 1993. doi: 10.1175/1520-0485(1993)023¡1767:ASMFTS¿2.0.CO;2.

[6] J.P. Boyd. Rational chebyshev spectral methods for unbounded so-

lutions on an infinite interval using polynomial-growth special basis functions. *COMPUT. Math. Appl.*, 41:1293–1315, 2001. doi: 10.1016/S0898-1221(01)00098-0.

[7] D.L. Boyer, D.B. Haidvogel, and N. Perenne. Laboratory-numerical model comparisons of canyon flows: A parameter study. *J. Phys. Oceanogr.*, 34:1588–1609, 2004. doi: 10.1175/1520-0485(2004)034¡1588:LMCOCF¿2.0.CO;2.

[8] K.W. Bruland, E.L. Rue, and G.J. Smith. Iron and macronutrients in california coastal upwelling regimes: Implications for diatom blooms. *Limnol. Oceanogr.*, 46:1661–1674, 2001.

[9] M.C. Buijsman and et al. Impact of parameterized internal wave drag on the semidiurnal energy balance in a global ocean circulation model. *J. Phys. Oceanogr.*, 46:1399–1419, 2016. doi: 10.1175/JPO-D-15-0074.1.

[10] M. Carr, M. Stastna, and P.A. Davies. Internal solitary wave-induced flow over a corrugated bed. *Ocean Dynamics*, 60:1007–1025, 2010. doi: 10.1007/s10236-010-0286-2.

[11] S. Carstensen, B.M. Sumer, and J. Fredsoe. Coherent structures in wave boundary layers. part 1. oscillatory motion. *J. Fluid Mech.*, 646: 169–206, 2010. doi: 10.1017/S0022112009992825.

[12] G.S. Carter and et al. Energetics of m2 barotropic-to-baroclinic tidal conversion at the hawaiian islands. *J. Phys. Oceanogr.*, 38:2205–2223, 2008. doi: 10.1175/2008JPO3860.1.

[13] V.K. Chalamalla and S. Sarkar. Mixing, dissipation rate, and their overturn-based estimate in a near-bottom turbulent flow driven by internal tides. *J. Phys. Oceanogr.*, 45:1969–1987, 2015. doi: 10.1175/JPO-D-14-0057.1.

[14] V.K. Chalamalla, B. Gayen, A. Scotti, and S. Sarkar. Turbulence during the reflection of internal gravity waves at critical and near-critical slopes. *J. Fluid Mech.*, 729:47–68, 2013. doi: 10.1017/jfm.2013.240.

[15] O.M. Cheriton, E.E. McPhee-Shaw, W.J. Shaw, T.P. Stanton, J.G. Bellingham, and C.D. Storlazzi. Suspended particulate layers and internal waves over the southern monterey bay continental shelf: An important control on shelf mud belts? *J. Geophys. Res. Oceans*, 119: 428–444, 2014. doi: 10.1002/2013JC009360.

[16] P.F. Cummins, J.Y. Cherniawsky, and M.G.G. Foreman. North pacific internal tides from the aleutian ridge: Altimeter observations and modeling. *J. Marine Res.*, 59:167–191, 2001. doi: 10.1357/002224001762882628.

[17] P.A. Davis and W.R. Peltier. Some characteristics of the kelvin-helmholtz and resonant overreflection modes of shearflow instability and of their interaction through vortex pairing. *J. Atmos. Sci.*, 36:2394–2412, 1979. doi: 10.1175/1520-0469(1979)036¡2394:SCOTKH¿2.0.CO;2.

[18] I.P.D. De Silva, H.J.S. Fernando, F. Eaton, and D. Hebert. Evolution

of kelvin-helmholtz billows in nature and laboratory. *Earth Planet. Sci. Lett.*, 143:217–231, 1996. doi: 10.1016/0012-821X(96)00129-X.

[19] P.J. Diamessis and L.G. Redekopp. Numerical investigation of solitary internal wave-induced global instability in shallow water benthic boundary layers. *J. Phys. Oceanogr.*, 36:784–798, 2006.

[20] P.J. Diamessis, J.A. Domaradzki, and J.S. Hesthaven. A spectral multidomain penalty method model for the simulation of high reynolds number localized incompressible stratified turbulence. *J. Comput. Phys.*, 202:298–322, 2005. doi: 10.1016/j.jcp.2004.07.007.

[21] W.S. Don, D. Gottlieb, and J.H. Jung. A multidomain spectral method for supersonic reactive flows. *J. Comput. Phys.*, 192:325–354, 2003. doi: 10.1016/j.jcp.2003.07.022.

[22] P. Echeverri, M.R. Flynn, K.B. Winters, and T. Peacock. Low-mode internal tide generation by topography: An experimental and numerical investigation. *J. Fluid Mech.*, 636:91–108, 2009. doi: 10.1017/S0022112009007654.

[23] G.D. Egbert and R.D. Ray. Significant dissipation of tidal energy in the deep ocean inferred from satellite altimeter data. *Nature*, 405:775–778, 2000.

[24] G.D. Egbert and R.D. Ray. Estimates of m-2 tidal energy dissipation from topex/poseidon altimeter data. *J. Geophys. Res. Oceans*, 106: 22475–22502, 2001. doi: 10.1029/2000JC000699.

[25] L.K. Forbes and S.R. Belward. Atmospheric interfacial waves. *Phys. Fluids*, 4:2222, 1992. doi: 10.1063/1.858463.

[26] O.B. Fringer and R. Street. The dynamics of breaking progressive interfacial waves. *J. Fluid Mech.*, 494:319–353, 2003. doi: 10.1017/S0022112003006189.

[27] B. Galperin, S. Sukoriansky, and P.S. Anderson. On the critical richardson number in stably stratified turbulence. *Atmos. Sci. Lett.*, 8:65–69, 2007.

[28] P. Garaud. Waves and instabilities in fluids. *University of California Santa Cruz*, 2013.

[29] A.E. Gargett. Vertical eddy diffusivity in the ocean interior. *J. Mar. Res.*, 42:359–393, 1984. doi: 10.1357/002224084788502756.

[30] G. Gargett, A.E.and Holloway. Dissipation and diffusion by internal wave breaking. *J. Mar Res.*, 42:15–27, 1984. doi: 10.1357/002224084788506158.

[31] C. Garrett. Internal tide and ocean mixing. *Science*, 301:1858–1859, 2003.

[32] C. Garrett and E. Kunze. Internal tide generation in the deep ocean. *Annu. Rev. Fluid Mech.*, 39:57–87, 2007. doi: 10.1146/annurev.fluid.39.050905.110227.

[33] C. Garrett and W. Munk. Internal waves in the ocean. *Annu. Rev. Fluid Mech.*, 11:339–369, 1979. doi: 10.1146/annurev.fl.11.010179.002011.

[34] C. Garrett and L. St Laurent. Aspects of deep ocean mixing. *J. Oceanogr.*, 58:11–24, 2002. doi: 10.1023/A:1015816515476.

[35] B. Gayen and S. Sarkar. Negative turbulent production during flow reversal in a stratified oscillating boundary layer on a sloping bottom. *Phys. Fluids*, 23:101703, 2011. doi: 10.1063/1.3651359.

[36] T. Gerkema and H. van Haren. Internal tides and energy fluxes over great meteor seamount. *Ocean Sci.*, 3:441–449, 2007. doi: 10.1029/JC089iC05p07999.

[37] T. Gerkema and J.T.F. Zimmerman. An introduction to internal waves. *Lecture Notes*, R. Neth. Inst. for Sea Res.:Den Burg., 2008.

[38] J.L. Guermond and J. Shen. Laboratory-numerical model comparisons of canyon flows: A parameter study. *Siam J. Numer. Anal.*, 41:112–134, 2003. doi: 10.1137/S0036142901395400.

[39] K.R. Helfrich and W.K. Melville. Long nonlinear internal waves. *Annu. Rev. Fluid Mech.*, 38:395–425, 2006. doi: 10.1146/annurev.fluid.38.050304.092129.

[40] J.S. Hesthaven. A stable penalty method for the compressible navier-stokes equations 2. one-dimensional domain decomposition schemes. *Siam J. Sci Comput.*, 18:658–685, 1997. doi: 10.1137/S1064827594276540.

[41] P.A. et. al. Holme. Shear induced platelet activation and platelet microparticle formation at blood flow conditionsas in arteries with sever

stenosis. *Arteriosclerosis thrombosis and vascular biology*, 17:646–653, 1997. doi: 10.1161/01.ATV.17.4.646.

[42] L.E. Holmedal and D. Myrhaug. Combined tidal and wind driven flows and bedload transport over a flat bottom. *Ocean Model.*, 68:37–56, 2013.

[43] D.A. Horn, J. Imbergerand, and G.N. Ivey. The degeneration of large-scale interfacial gravity waves in lakes. *J. Fluid Mech.*, 434:181–207, 2001.

[44] L.N. Howard. Note on a paper of john w. miles. *J. Fluid Mech.*, pages 509–512, 1961. doi: 10.1017/S0022112061000317.

[45] E.L. Hult, C.D. Troy, and J.R. Koseff. The breaking of interfacial waves at a submerged bathymetric ridge. *J. Fluid Mech.*, 637:45–71, 2009. doi: 10.1017/S0022112009008040.

[46] I.G. Johnsson. A new approach to oscillatory rough turbulent boundary layers. *Ocean Eng.*, 7:109–152, 1980.

[47] T.M.S. Johnston, M.A. Merrifield, and P.E. Holloway. Internal tide scattering at the line islands ridge. *J. Geophys. Res. Oceans*, 108:3365, 2003. doi: 10.1029/2003JC001844.

[48] I.G. Jonsson. A new approach to oscillatory rough tubulent boundary layers. *Ocean Eng.*, 7:109–152, 1984. doi: 10.1016/0029-8018(80)90034-7.

[49] G.E. Karniadakis, M. Isaeli, and S.A. Orszag. High-order splitting methods for the incompressible navier stokes equations. *J. Comput. Phys.*, 97:414–443, 1991. doi: 10.1016/0021-9991(91)90007-8.

[50] P.K. Kundu, I.M. Cohen, and D.R. Dowling. Fluid mechanics (sixth edition). *Academic Press*, 2016. doi: 10.1016/B978-0-12-405935-1.01001-7.

[51] E. Kunze and S. G. Llewellyn Smith. The role of smallscale topography in turbulent mixing of the global ocean. *Oceanography*, 17:55–64, 2004.

[52] A. Lefauve, C. Muller, and A. Melet. A three-dimensional map of tidal dissipation over abyssal hills. *J. Geophys. Res. Oceans*, 120:4760–4777, 2015. doi: 10.1002/2014JC010598.

[53] S. Legg. Scattering of low-mode internal waves at finite isolated topography. *J. Phys. Oceanogr.*, 44:359–383, 2014. doi: 10.1175/JPO-D-12-0241.1.

[54] J.G. Levin, M. Iskandarani, and D.B. Haidvogel. A spectral filtering procedure for eddy-resolving simulations with a spectral element ocean model. *J. Comput. Phys.*, 137:130–154, 1997. doi: 10.1006/jcph.1997.5797.

[55] J.A. MacKinnon and K.B. Winters. Subtropical catastrophe: Significant loss of low-mode tidal energy at 28.9 degrees. *Geophys. Res. Lett.*, 32:L15605, 2005. doi: 10.1029/2005GL023376.

[56] J.A. et. al. MacKinnon. Climate process team on internal wave-driven ocean mixing. *Am. Meteorol. Soc.*, pages 2429–2454, 2017. doi: 10.1175/BAMS-D-16-0030.1.

[57] E. McPhee-Shaw. Boundary-interior exchange: Reviewing the idea that internal-wave mixing enhances lateral dispersal near continental margins. *Deep Sea Res. Part 2.*, 53:42–59, 2006. doi: 10.1016/j.dsr2.2005.10.018.

[58] E.E. McPhee-Shaw and E. Kunze. Boundary layer intrusions from a sloping bottom: A mechanism for generating intermediate nepheloid layers. *J. Geophys. Res. Oceans*, 107:3050, 2002. doi: 10.1029/2001JC000801.

[59] A. Melet, R. Hallberg, S. Legg, and K. Polzin. Sensitivity of the ocean state to the vertical distribution of internal-tide-driven mixing. *J. Phys. Oceanogr.*, 43:602–615, 2013. doi: 10.1175/JPO-D-12-055.1.

[60] A. Melet, R. Hallberg, S. Legg, and M. Nikurashin. Sensitivity of the ocean state to lee wave- driven mixing. *J. Phys. Oceanogr.*, 44:900–921, 2014. doi: 10.1175/JPO-D-13-072.1.

[61] A. Melet, S. Legg, and R. Hallberg. Climatic impacts of parameterized local and remote tidal mixing. *J. Clim.*, 29:3473–3500, 2016. doi: 10.1175/JCLI-D-15-0153.1.

[62] A. Mujal-Colilles, K.T. Christensen, A. Bateman, and M.H. Garcia. Coherent structures in oscillatory flows within the laminar-to-turbulent

transition regime for smooth and rough walls. *J. Hydraul. Res.*, 54: 502–515, 2016. doi: 10.1080/00221686.2016.1174960.

[63] W.H. Munk. Once again: Once again - tidal friction. *J Phys. Oceanogr.*, 40:7–35, 1997. doi: 10.1016/S0079-6611(97)00021-9.

[64] J. D. Nash, E. Alford, M. H.and Kunze, K. Martini, and S. Kelly. Hotspots of deep ocean mixing on the oregon continental slope. *Geophys. Res. Lett.*, 34:L01605, 2007. doi: 10.1029/2006GL028170.

[65] P. Nielsen. On the structure of oscillatory boundary layers. *Coast. Eng.*, 9:261–276, 1985.

[66] C.E. Ozdemir, T.J. Hsu, and S. Balachandar. Direct numerical simulations of instability and boundary layer turbulence under a solitary wave. *J. Fluid Mech.*, 731:545–578, 2013. doi: 10.1017/jfm.2013.361.

[67] P. Passaggia, K.R. Helfrich, and B.L. White. Optimal transient growth in thin-interface internal solitary waves. *J. Fluid Mech.*, 840:342–378, 2018. doi: 10.1017/jfm.2018.19.

[68] T. Peacock, M.J. Mercier, H. Didelle, and S. Viboud. A laboratory study of low-mode internal tide scattering by finite-amplitude topography. *Phys. Fluids*, 21:121702, 2009. doi: 10.1063/1.3267096.

[69] F. Pétrélis, S.L. Smith, and W.R. Young. Tidal conversion at a submarine ridge. *J. Phys. Oceanogr.*, 36:1053–1071, 2006.

[70] L. Rainville and R. Pinkel. Propagation of low-mode internal waves through the ocean. *J. Phys. Oceanogr.*, 36:1220–1236, 2006.

[71] R. D. Ray and G. T. Mitchum. Surface manifestation of internal tides in the deep ocean: Observations from altimetry and island gauges. *Prog. Oceanogr.*, 40:135–162, 1997.

[72] W.C.. Reynolds and M.C. Potter. Finite-amplitude instability of parallel shear flows. *J. Fluid Mech.*, 27:465–492, 1967.

[73] O. Richet, C.M. Muller, and J.M. Chomaz. Impact of a mean current on the internal tide energy dissipation at the critical latitude. *J. Phys. Oceanogr.*, 47:1457–1472, 2017. doi: 10.1175/JPO-D-16-0197.1.

[74] G.A. Rivera-Rosario, P.J. Diamessis, and J.T. Jenkins. Bed failure induced by internal solitary waves. *J. Geophys. Res. Oceans*, 122:5468–5485, 2017. doi: 10.1002/2017JC012935.

[75] D.L. Rudnick, T.J. Boyd, R.E. Brainard, G.S. Carter, G.D. Egbert, and M.C. Gregg. From tides to mixing along the hawaiian ridge. *Science*, 301:355–357, 2003.

[76] M.M Sadek, L. Parras, P.J. Diamessis, and P.L.-F. Liu. Two-dimensional instability of the bottom boundary layer under a solitary wave. *Phys. Fluids*, 27, 2015.

[77] R.M. Samelson. Large-scale circulation with locally enhanced vertical mixing. *J. Phys. Oceanogr.*, 28:712–726, 1998. doi: 10.1175/1520-0485(1998)028¡0712:LSCWLE¿2.0.CO;2.

[78] H. Sandstrom and Elliott J.A. Internal tide and solitons on the sco-

tian shelf: A nutrient pump at work. *J. Geophys. Res. Oceans*, 89: 6415–6426, 1984.

[79] P.J. Schmid and D.S. Henningson. Stability and transition in shear flows. *Springer*, 2001. doi: 10.1007/978-1-4613-0185-1.

[80] T. Schneider and et. al. Climate goals and computing the future of clouds. *Nat. Clim. Chang.*, 7:3–5, 2017.

[81] J.C. Sevadjian, E.E. McPhee-Shaw, B.Y. Raanan, O.M. Cheriton, and C.D. Storlazzi. Vertical convergence of resuspended sediment and subducted phytoplankton to a persistent detached layer over the southern shelf of monterey bay, californi. *J. Geophys. Res. Oceans*, 120:3462–3483, 2015. doi: 10.1002/2015JC010785.

[82] J. Sharples, C.M. Moore, and E.R. Abraham. Internal tide dissipation, mixing, and vertical nitrate flux at the shelf edge of ne new zealand. *J. Geophys. Res.*, 106:14069–14081, 2001. doi: 10.1175/JPO-D-16-0197.1.

[83] R.K. Shearman and S.J. Lentz. Observations of tidal variability on the new england shelf. *J. Geophys. Res.*, 109:C06010, 2004. doi: 10.1029/2003JC001972.

[84] J.F. Shriver and et. al. An evaluation of the barotropic and internal tides in a high-resolution global ocean circulation model. *J. Geophys. Res.*, 117:C10024, 2012. doi: 10.1029/2012JC008170.

[85] S. A. Siedlecki, D. E. Archer, and A. Mahadevan. Nutrient exchange

and ventilation of benthic gases across the continental shelf break. *J. Geophys. Res.*, 116:C06023, 2011. doi: 10.1029/2010JC006365.

[86] H.L. Simmons, R.W. Hallberg, and B.K. Arbic. Internal wave generation in a global baroclinic tide model. *Deep Sea Res. Part 2*, 51: 3043–3068, 2004. doi: 10.1016/j.dsr2.2004.09.015.

[87] H.L. Simmons, S.R. Jayne, L.C. St. Laurent, and A.J. Weaver. Tidally driven mixing in a numerical model of the ocean general circulation. *Ocean Model.*, 6:245–263, 2004. doi: 10.1016/S1463-5003(03)00011-8.

[88] D.N. Slinn and J.J. Riley. A model for the simulation of turbulent boundary layers in an incompressible stratified flow. *J. Comput. Phys.*, 144:550–602, 1998. doi: 10.1006/jcph.1997.5983.

[89] W.D. Smyth. Instability in geophysical flows: Lecture notes for oc680. *College of Earth, Ocean and Atmospheric Sciences*, Oregon State University, 2016.

[90] L. St. Laurent and C. Garrett. The role of internal tides in mixing the deep ocean. *J. Phys. Oceanogr.*, 32:2882–2899, 2002.

[91] M. Stastna and K.G. Lamb. Vortex shedding and sediment resuspension associated with the interaction of an internal solitary wave and the bottom boundary layer. *Geophys. Res. Lett.*, 29:1512, 2002. doi: 10.1029/2001GL014070.

[92] T. Stefanakis. Bottom boundary layer instabilities iduced by nonlinear internal waves. 2010.

[93] B.M. Sumer, P.M. Jensen, L.B. Sorensen, J. Fredsoe, P.L.-F. Lui, and S. Carstensen. Coherent structures in wave boundary layers. part 2. solitary motion. *J. Fluid Mech.*, 646:207–231, 2010. doi: 10.1017/S0022112009992837.

[94] B. Sutherland. Internal gravity waves. *Cambridge University Press*, 2010. doi: 10.1017/CBO9780511780318.

[95] S.A. Thorpe. On the reflection of a train of finite-amplitude internal waves from a uniform slope. *J. Fluid Mech.*, 178:279–302, 1987. doi: 10.1017/S0022112087001228.

[96] J. Trowbridge and O.S. Madsen. Turbulent wave boundary layers 1. model formulation and first-order solution. *J. Geophys. Res. Oceans*, 89:7999–8007, 1984. doi: 10.1029/JC089iC05p07999.

[97] J. Trowbridge and O.S. Madsen. Turbulent wave boundary layers 2. 2nd order theory and mass transport. *J. Geophys. Res. Oceans*, 89: 7989–7997, 1984. doi: 10.1029/JC089iC05p07989.

[98] C.D. Troy and J.R. Koseff. The instability and breaking of long internal waves. *J. Fluid Mech.*, 543:107–136, 2005. doi: 10.1017/S0022112005006798.

[99] H. van Haren and L. Gostiaux. Large internal waves advection in very weakly stratified deep mediterranean waters. *Geophys. Res. Lett.*, 38: L22603, 2011. doi: 10.1029/2011GL049707.

[100] D.J. Wain, M.C. Gregg, M.H. Alford, R.C. Lien, R.A. Hall, and

G.S. Carter. Propagation and dissipation of the internal tide in upper monterey canyon. *J. Geophys. Res.*, 118:4855–4877, 2013. doi: 10.1002/jgrc.20368.

[101] T. Wang and Y. Lin. Wave ducting in a stratified shear flow over a two-dimensional mountain. part i: General linear. *J. Atmos. Sci.*, 56:412–436, 1999. doi: 10.1175/1520-0469(1999)056¡0412:WDIASS¿2.0.CO;2.

[102] A.F. Waterhouse and al. et. Global patterns of diapycnal mixing from measurements of the turbulent dissipation rate. *J. Phys. Oceanogr.*, 44:1854–1872, 2014. doi: 10.1175/JPO-D-13-0104.1.

[103] C. Wunsch. Internal tides in the ocean. *Rev. Geophys. Space Phys.*, 13:167–182, 1975.

[104] S. Wunsch. Nonlinear harmonic generation by diurnal tides. *Dyn. Atmos. Oceans*, 71:91–97, 2015. doi: 10.1016/j.dynatmoce.2015.06.002.

[105] S. Wunsch and T. Drivas. Internal tide energy transfer by nonlinear refraction. *International Symposium on Stratified Flows*, 7, 2016.

[106] X.H. Xie, G.Y. Chen, X.D. Shang, and W.D. Fang. Evolution of the semidiurnal (m-2) internal tide on the continental slope of the northern south china sea. *Geophys. Res. Lett.*, 35:L13604, 2008. doi: 10.1029/2008GL034179.

[107] J.Z. Zhang, M.O. Baringer, C.J. 1 Fischer, and J.A Hooper. An estimate of diapycnal nutrient fluxes to the euphotic zone in the florida straits. *Sci. Rep.*, 7:16098, 2017. doi: 10.1038/s41598-017-15853-0.

[108] Z. Zhao, M.H. Alford, J.B. GIRTON, L. RAINVILLE, and H.L. Simmons. Global observations of open-ocean mode-1 m2 internal tides. *J. Phys. Oceanogr.*, 46:1657–1684, 2016. doi: 10.1175/JPO-D-15-0105.1.